UNIVERSIDAD DE CHILE
FACULTAD DE CIENCIAS FÍSICAS Y MATEMÁTICAS
DEPARTAMENTO DE GEOLOGÍA

SIGNATURAS GEOQUÍMICAS SEDIMENTARIAS DE LOS SULFUROS DE CU-(FE) DEL DEPÓSITO EL SOLDADO, REGIÓN DE VALPARAÍSO, CHILE

TESIS PARA OPTAR AL GRADO DE MAGÍSTER EN CIENCIAS, MENCIÓN GEOLOGÍA

MEMORIA PARA OPTAR AL TÍTULO DE GEÓLOGA

CAMILA ALCOHOLADO MAILLARD

PROFESOR GUÍA:
MARTIN REICH MORALES

PROFESOR CO-GUÍA:
FERNANDO BARRA PANTOJA

MIEMBROS DE LA COMISIÓN:
ALIDA PÉREZ FODICH
IRENE DEL REAL CONTRERAS

Este trabajo fue financiado por el proyecto FONDECYT Regular#1230161.

SANTIAGO DE CHILE
2024

RESUMEN DE LA TESIS PARA OPTAR AL GRADO DE MAGÍSTER EN CIENCIAS, MENCIÓN GEOLOGÍA Y MEMORIA PARA OPTAR AL TÍTULO DE GEÓLOGA

POR: Camila Alcoholado Maillard

FECHA: 2024

PROFESOR GUÍA: Martin Reich Morales

SIGNATURAS GEOQUÍMICAS SEDIMENTARIAS DE LOS SULFUROS DE CU-(FE) DEL DEPÓSITO EL SOLDADO, REGIÓN DE VALPARAÍSO, CHILE

Los depósitos estratoligados de Cu-(Ag) de la Cordillera de la Costa, tercera fuente de cobre en Chile, se dividen en dos grupos en base a su edad de formación: Jurásico Superior y Cretácico Inferior. Un ejemplo paradigmático de este último grupo corresponde a El Soldado, de relevancia debido a su tamaño y la asociación entre mineralización de cobre y materia orgánica en forma de (piro)bitumen. A pesar de su importancia, uno de los aspectos que no ha sido suficientemente estudiado en El Soldado corresponde a la geoquímica de elementos mayores, menores y traza de los sulfuros de Cu-(Fe), la cual puede aportar información sobre la naturaleza de los fluidos que dieron origen al depósito. Es por esto que el objetivo planteado en esta tesis es constreñir la distribución y concentración de dichos elementos en los sulfuros de ganga (pirita) y mena (calcopirita, bornita y calcosina) de El Soldado, de manera de identificar su signatura geoquímica y evaluar su potencial relación genética con la materia orgánica. Para ello se utiliza una combinación de técnicas micro-analíticas, incluyendo microscopía óptica de polarización y microscopía electrónica de barrido (SEM), análisis de microsonda electrónica (EPMA), espectrometría de masas por plasma inductivamente acoplado con ablación láser (LA-ICP-MS) y micro-fluorescencia de rayos X (µ-XRF).

Los resultados petrográficos sugieren que el depósito fue formado en dos etapas consecutivas, una de pre-mena y otra de mena, en donde los sulfuros de Cu-(Fe) presentan una cantidad importante de elementos traza, ya sea en solución sólida, o bien como inclusiones de micro y nanopartículas. La pirita es el mayor huésped de elementos traza incorporando entre decenas y miles de ppm de Mn, Co, Ni, As, Mo, Ag, Tl y Pb. La bornita es capaz de hospedar cantidades apreciables de Mn, Se, Ag, Tl, Pb y Bi, mientras que la calcopirita es solo un huésped menor, incorporando Mn, Se, Ag, In y Pb. Finalmente, la calcosina presenta concentraciones significativas de Ag y Fe. Algunos de estos elementos, por ejemplo, Mn, Ni, Mo y Tl, se relacionan a ambientes asociados a fluidos de origen sedimentario con importante influencia de materia orgánica. Además, de manera complementaria, análisis geoquímicos en granos de bitumen indican la presencia de cantidades significativas (de hasta miles de ppm) de ligantes y metales (S, Cl, Cu y Ag).

Por último, las razones elementales de Co/Ni y Mn/Fe vs Mo en pirita, e In/Se y Ag/Bi en calcopirita y bornita respectivamente, fueron analizadas y comparadas con depósitos estratoligados de Cu tanto en Chile como en otras regiones a nivel mundial (Irán y Polonia), y también con otros tipos de depósitos que ocurren en la franja metalogénica de la Cordillera de la Costa del centro-norte Chile (depósitos de óxido de hierro-cobre-oro (IOCG), óxido de hierro-apatito (IOA) y pórfido de cobre). Los resultados sugieren que efectivamente El Soldado presenta similitudes con depósitos considerados de origen sedimentario, siendo la razón de Co/Ni en pirita de gran potencial como herramienta de exploración en la Cordillera de la Costa chilena.

A Carolina y Alejandro

AGRADECIMIENTOS

En primer lugar, me gustaría agradecer a mi profesor guía, Martin Reich, por su confianza y apoyo en la realización de esta tesis, por sus enseñanzas, y su gran disposición a resolver cada una de las inquietudes que surgieron en este camino. Agradecer también a mi profesor co-guía, Fernando Barra, por toda la contribución al trabajo y por todas sus enseñanzas invaluables en el reconocimiento de minerales. Agradecer también a la profesora Irene del Real por aceptar ser miembro de la comisión y por los comentarios y ayuda otorgada. No pueden quedar atrás todos quienes hicieron posible el desarrollo de la investigación a través de su apoyo técnico en los múltiples análisis realizados: Rurik Romero, Gelu Costin, Christian Nievas y Ricardo Cabeza.

Agradecer a las y los funcionarios del Departamento de Geología. A Maritza, Blanca, Tonya, William, Rosita, Mariela, Luis, don Julio y a todos quienes me ayudaron en cada cosa que se necesitara y en los interminables trámites.

Quiero agradecer también a mi familia, sobre todo a mi mamá y papá, por su amor incondicional, por su apoyo fundamental durante cada uno de estos procesos, por sus consejos y esfuerzo durante todos estos años. Agradecer a mis abuelos, la Juani y el Tata por todo el amor que me dieron, y a mi abuelita Gloria por todo su apoyo y regaloneo.

A mis amigas de Plan Común, la Ale, Vale, Tami y Oppi por cada una de esas juntas y por su compañía desde los primeros años de la universidad. Agradecer a cada uno de mis amigos de geología, los geopanes, por todos esos momentos de risas, terrenos, estudios, y conversaciones a lo largo de estos años. En especial, agradecer a la Karin Javi, amigas desde los primeros días de Geo, al Joaco y al Aaron por todos esos cafés y conversaciones en este periodo de magíster, al geobestie Curi, a la Tania, Cata, Alexis, Lucas, Deb y Roberto, y muchos otros por su compañía durante estos últimos años, Agradezco también a cada uno de los que conocí en las oficinas del -1, por todos esos momentos de distensión, risas, y aprendizajes, agradecer sobre todo a la Mary y la Anto que aguantaron todas mis mañas estos últimos años.

Agradecer al Camilo por todo su apoyo durante estos ya casi 4 años, y sobre todo durante este último periodo, gracias por toda tu ayuda, paciencia, tus consejos y tu contención. Gracias por hacerme reír cuando estoy estresada, por darme un espacio en tu vida, y por haber sido un pilar fundamental en todos estos años.

Finalmente, agradecer al apoyo otorgado por el proyecto FONDECYT Regular #1230161, a la beca de Magíster Nacional de ANID que proveyó el financiamiento para mis estudios de postgrado (#22230553), y a la beca “Graduate Student Fellowship” otorgada por la Society of Economic Geologists (SEG), que aportó con financiamiento adicional para el desarrollo de esta tesis.

TABLA DE CONTENIDOS

ÍNDICE DE FIGURAS

CAPÍTULO 1:
INTRODUCCIÓN

1.1. Motivación

La presente tesis tiene por objetivo principal aportar al conocimiento del depósito estratoligado de Cu-(Ag) de El Soldado, ubicado en la comuna de Nogales, región de Valparaíso, y en particular, evaluar, a través del análisis geoquímico de sulfuros de Cu-(Fe), el origen y naturaleza de los fluidos involucrados en su formación. Para esto se realiza un estudio de detalle de secciones transparentes-pulidas obtenidas de la colección personal del Dr. Marcos Zentilli, la cual representa el material de investigación existente a la fecha más completo, representativo y geológicamente constreñido del depósito. Las muestras fueron caracterizadas petrográfica, textural y geoquímicamente para identificar la signatura geoquímica de los sulfuros de mena y ganga del depósito, los procesos que propiciaron su formación, y las implicancias que esto puede tener tanto en el modelo genético del depósito, como en la generación de herramientas de apoyo a la exploración.

1.1.1. Depósitos estratoligados de Cu-(Ag)

Chile es reconocido por ser uno de los principales productores de cobre (Cu) a nivel global, destacando además importantes producciones de otros metales como el molibdeno (Mo) y la plata (Ag), los cuales son recuperados como subproductos dentro del proceso minero (Servicio Nacional de Geología y Minería, 2023). Dentro de este contexto, los depósitos de tipo estratoligados de Cu-(Ag) representan actualmente la tercera fuente de cobre más importante de Chile, antecedidos por los depósitos de tipo pórfido cuprífero y óxido de hierro-cobre-oro (del inglés, IOCG). Este tipo de depósitos, también conocidos como yacimientos de tipo manto chilenos, se encuentran hospedados en rocas volcánicas y volcano-sedimentarias del Jurásico Superior a Cretácico Inferior, en una franja de más de 1000 km de extensión entre los 22-34°S de la Cordillera de La Costa (Maksaev & Zentilli, 2002).

Los depósitos estratoligados de Cu-(Ag) se formaron durante la primera etapa del Ciclo Tectónico Andino, posterior a un prolongado periodo de inactividad tectónica entre 240 y 190 Ma (Mpodozis & Kay, 1990; Charrier et al., 2007). A partir de este momento, la placa oceánica de Phoenix, de mayor antigüedad y de menor temperatura, comienza a subducir bajo el margen suroeste de Gondwana con un alto ángulo, provocando así un "roll-back" de la placa oceánica. Esto genera un ambiente extensional en el tras-arco, adelgazamiento de la corteza continental, un arco magmático activo a lo largo del margen sudamericano, la formación de cuencas de intra-arco entre los 28 y 35°S, cuencas de tras-arco entre los 21 y 27°S, y eventos de transgresión-regresión marina hacia el este del arco continental (Figura 1; Coira et al., 1982; Mpodozis & Ramos, 1989; Mpodozis & Allmendinger, 1993; Maksaev & Zentilli, 2002; Charrier et al., 2007; Maksaev et al., 2007; Oliveros et al., 2020; Jara et al., 2021a, b; Ojeda et al., 2024). Hacia fines del Cretácico Inferior ocurre un cambio en las condiciones tectónicas del margen sudamericano, produciéndose una

continua disminución del ángulo de subducción, la migración del arco magmático hacia el este, la inversión de las cuencas previamente formadas y el cese de la actividad magmática en el arco occidental de Sudamérica, marcando así un cambio en la impronta metalogénica de la Cordillera de la Costa (Mpodozis & Ramos, 1989; Ramos & Aleman, 2000; Maksaev & Zentilli, 2002; Jara et al., 2021a, b).

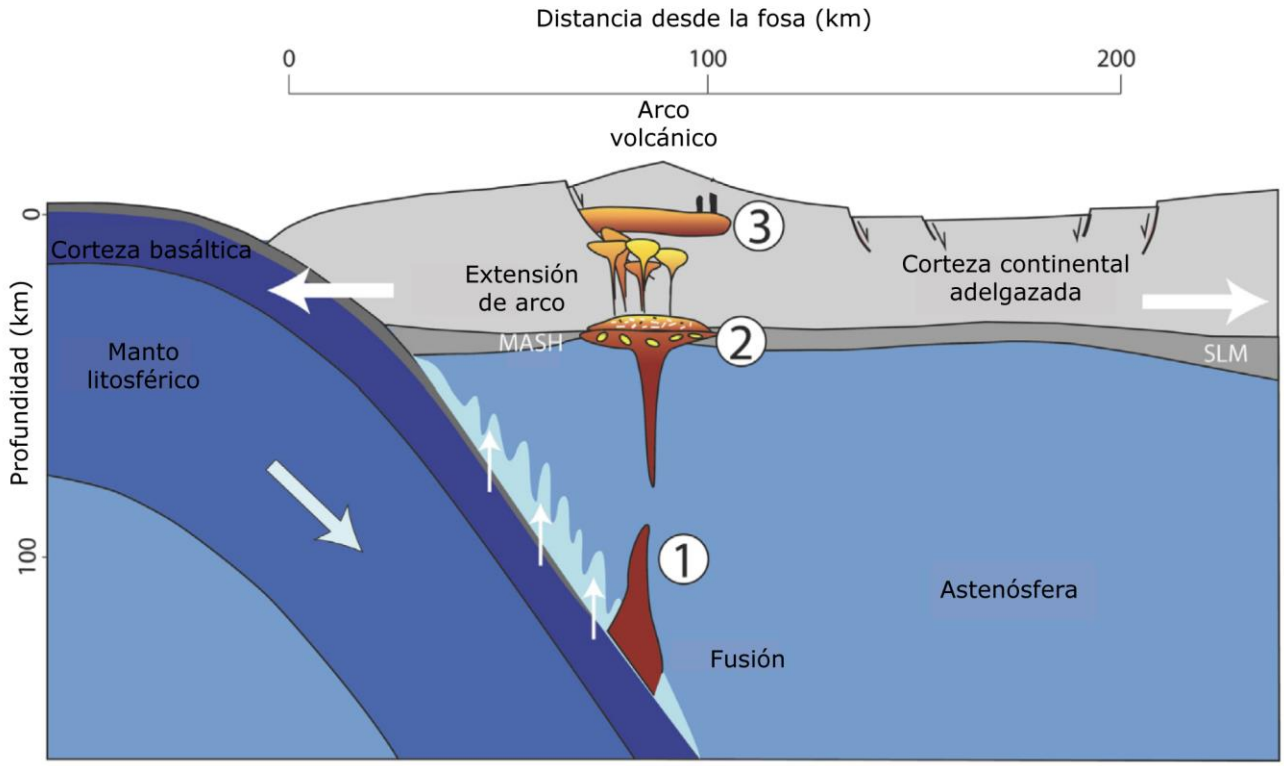

Figura 1. *Contexto tectono-magmático de la Cordillera de la Costa durante el Cretácico. Modificado de Ojeda et al. (2024).*

El origen de los depósitos estratoligados de Cu-(Ag) ha sido ampliamente discutido en la literatura, habiendo tanto hipótesis singenéticas como epigenéticas para su formación (Ruiz et al., 1965; Sato, 1984; Oliveros et al., 2008; Kojima et al., 2009), siendo esta última la más aceptada debido a las características geológicas, estructurales, isotópicas y geocronológicas de este tipo de depósitos. Además, a partir de estas características y de su ubicación espacial, se pueden definir también dos grandes grupos para este tipo de depósitos, aquellos del Jurásico Superior y del Cretácico Inferior (Figura 2).

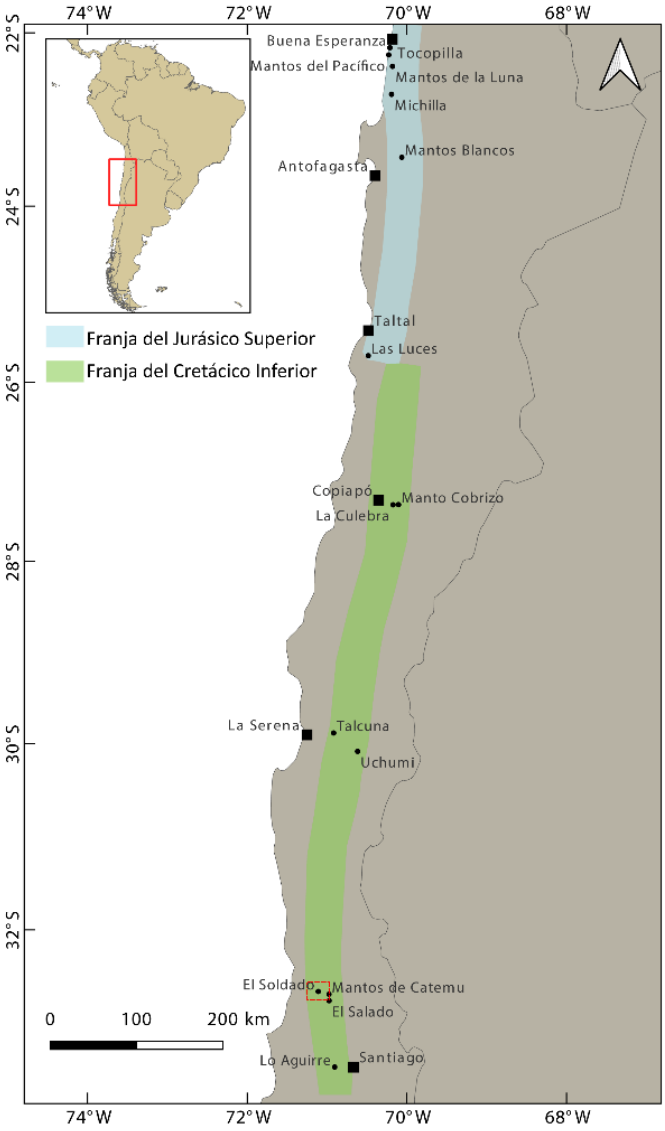

Figura 2. *Ubicación de los depósitos Estratoligados de Cu-(Ag) en la Cordillera de la Costa de la zona central y norte de Chile. Modificado de Herazo et al. 2020.*

Los depósitos del Jurásico Superior se encuentran distribuidos a lo largo de la Cordillera de la Costa de la zona norte de Chile, entre los 22° a 26°S, aproximadamente entre las localidades de Taltal y Tocopilla. En este tipo de depósitos, la mineralización es hospedada en lavas porfíricas basálticas a andesíticas, o bien en cuerpos brechosos del Jurásico (Maksaev & Zentilli, 2002). Algunos ejemplos característicos corresponden a los yacimientos de Buena Esperanza, Michilla, Mantos Blancos y Las Luces (Figura 2). Por otra parte, los cuerpos estratoligados de la franja del Cretácico Inferior se distribuyen en la zona centro y norte de Chile, entre los 26° y 34°S, entre las ciudades de Taltal y Santiago, en donde la mineralización es hospedada principalmente en secuencias volcánicas con intercalaciones de rocas sedimentarias marinas. Algunos ejemplos característicos de este segundo grupo corresponden, de norte a sur, a los depósitos de la zona de Copiapó (ej. Manto Cobrizo, La Culebra), aquellos cercanos a La Serena (ej. Talcuna), y los depósitos de El

Soldado y Lo Aguirre, cercanos a Santiago. En ambos grupos es posible la identificación de dos etapas de formación, configuradas por una etapa temprana o de pre-mena, seguida de una etapa principal o de mena. Durante la etapa de pre-mena se habría formado principalmente pirita, asociada a minerales de alteración y/o de metamorfismo de bajo grado, mientras que en la etapa de mena se habrían generado sulfuros de Cu, principalmente calcopirita, bornita y calcosina. En el caso particular de los depósitos del Cretácico Inferior, tanto las asociaciones minerales de la etapa de pre-mena, como aquellas de la etapa de mena, están asociadas a la presencia pirita framboidal, de origen bacteriano, y a la presencia de materia orgánica solidificada en forma de (piro)bitumen (Wilson & Zentilli, 1999; Boric et al., 2002; Maksaev & Zentilli, 2002).

El bitumen corresponde a uno de los principales precursores del gas metano, y se define como materia orgánica sólida/viscosa migrada, o bien como el componente soluble de la materia orgánica (Parnell et al., 1993). El bitumen es generado a partir del kerógeno, el que corresponde a materia orgánica insoluble en solventes orgánicos y es formado a partir de plantas y biomasas (Figura 3). Una vez que el bitumen madura termalmente, debido al sometimiento a mayores temperaturas y presiones, se descompondrá en gas metano y en (piro)bitumen, siendo este último un residuo orgánico rico en carbono (Figura 3; Gaupp et al., 2008).

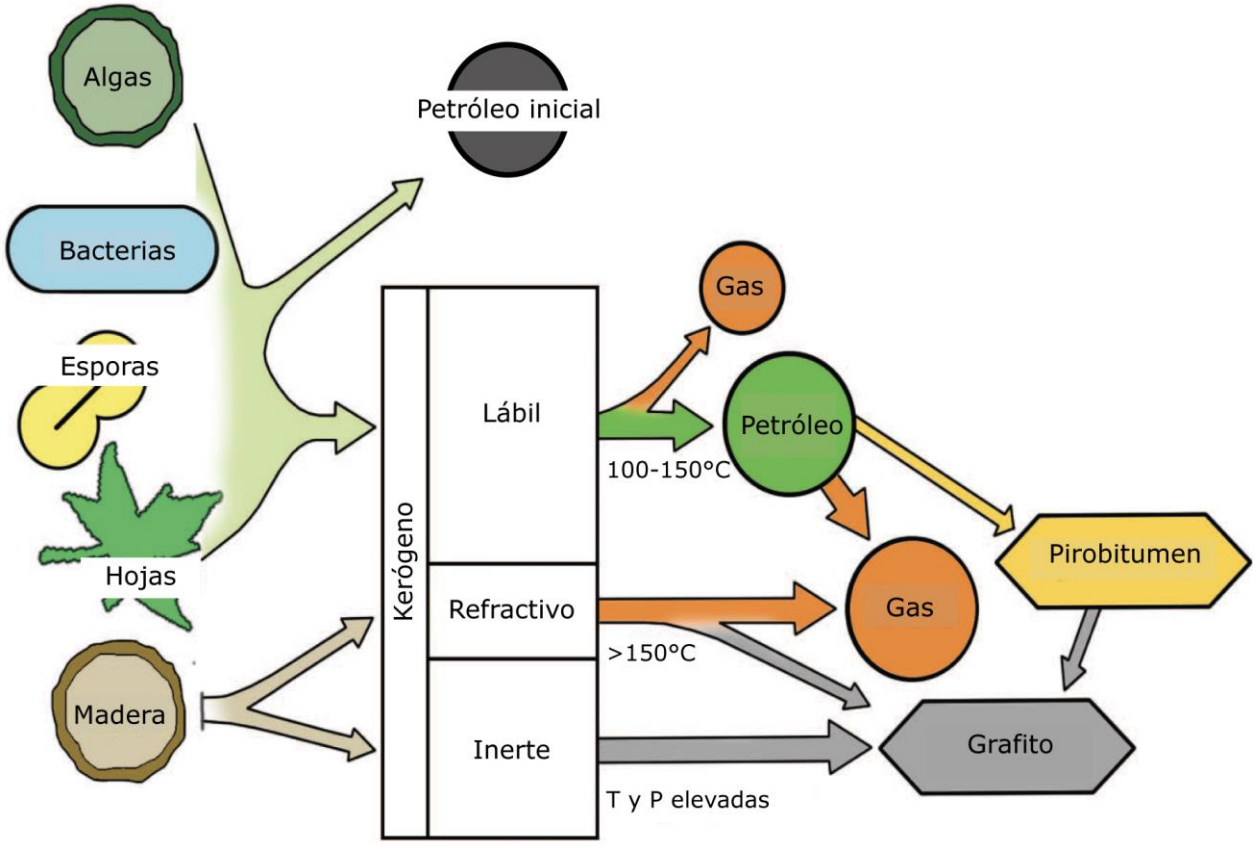

Figura 3. *Esquema de las relaciones entre biomasa, kerógeno, petróleo, (piro)-bitumen y gas natural. Modificado de Gaupp et al. (2008).*

La asociación entre materia orgánica y depósitos de cobre ha sido identificada y estudiada en una variedad de depósitos estratiformes de cobre tanto en Chile como en otras localidades, tales como Irán y Polonia, y también en otros tipos de ambientes, entre los que se incluyen depósitos de

plomo-zinc de tipo Mississippi Valley, y depósitos de oro y de uranio alojados en rocas sedimentarias (Parnell et al., 1993; Spirakis and Heyll, 1993; Wilson & Zentilli, 2006; Large et al., 2011; Affouri et al., 2013; Fuchs et al., 2015; Perona et al., 2018; Saintilan et al., 2019; Movahednia et al., 2022). En estos diversos trabajos, se ha postulado que la materia orgánica, generalmente en forma de bitumen o (piro)bitumen, puede actuar como un agente reductor de los fluidos hidrotermales que transportan los metales, propiciando así la precipitación de sulfuros. Sin embargo, no se descarta que la materia orgánica también juegue un rol activo en el transporte y precipitación de metales; por ello, su estudio además es relevante tanto para comprender la evolución temporal y espacial de depósitos con presencia de materia orgánica, como para la generación de herramientas que apoyen la exploración de nuevos recursos.

1.1.2. El Soldado

El Soldado (140.7 Mt @ 0.56% Cu, incluyendo recursos medidos e indicados; Anglo American, 2022), ubicado en la comuna de Nogales, corresponde al yacimiento de mayor envergadura de los depósitos estratoligados de Cu-(Ag) de la franja del Cretácico Inferior. La actividad minera en El Soldado se remonta al siglo XVIII con la explotación de zonas expuestas de alta ley. En el año 1919 comienza la explotación moderna en el distrito, con leyes que oscilan entre 7 y 15%, y que son extraídas a partir de minas subterráneas. En el año 1978 Exxon Minerals se convierte en el propietario de El Soldado, quien genera campañas de perforación y exploración, concluyendo en el descubrimiento de cuerpos mineralizados no expuestos, y permitiendo así aumentar las reservas minerales (Boric et al., 2002). Desde el año 2002, Anglo American es la compañía propietaria de El Soldado, no siendo actualmente explotado.

El depósito se encuentra hospedado en el miembro superior de la Formación Lo Prado (Figura 4, 5), la cual corresponde a una secuencia de lavas félsicas a basálticas intercaladas con rocas sedimentarias (calcilutitas, calcarenitas, brechas y conglomerados) de edad Cretácica Superior (Nasi & Thiele. R, 1982; Rivano, 1993; Aguirre et al., 1999; Fuentes et al., 2005). Esta secuencia volcano-sedimentaria se encuentra sobre el miembro inferior de la Fm. Lo Prado, caracterizado por la presencia de secuencias marinas, siendo esta la posible fuente de materia orgánica en El Soldado. Suprayacente a la Fm. Lo Prado, se encuentra la Formación Veta Negra (Figura 4, 5), característica de un ambiente transicional-terrestre. A rasgos generales, la secuencia en la cual se encuentra emplazado el depósito, se puede interpretar como un ambiente transicional marino-terrestre, concordante con un arco volcánico-plutónico desarrollado en el margen occidental del continente, dentro de un contexto de subsidencia y extensión cortical (Aberg et al., 1984; Vergara et al., 1995; Boric et al., 2002; Charrier et al., 2007; Boyce et al., 2020).

En El Soldado la mineralización se encuentra estrechamente relacionada tanto a un control litológico ejercido por la secuencia volcano-sedimentaria, como también a un control estructural predominante. En este sentido, los distintos cuerpos mineralizados se distribuyen dentro de un sistema estructural regional de rumbo NS-NNW, caracterizado por fallas de rumbo sinestrales y fallas normales reactivadas con manteos de 60° hacia el oeste (Figura 4, 5; Boric et al., 2002).

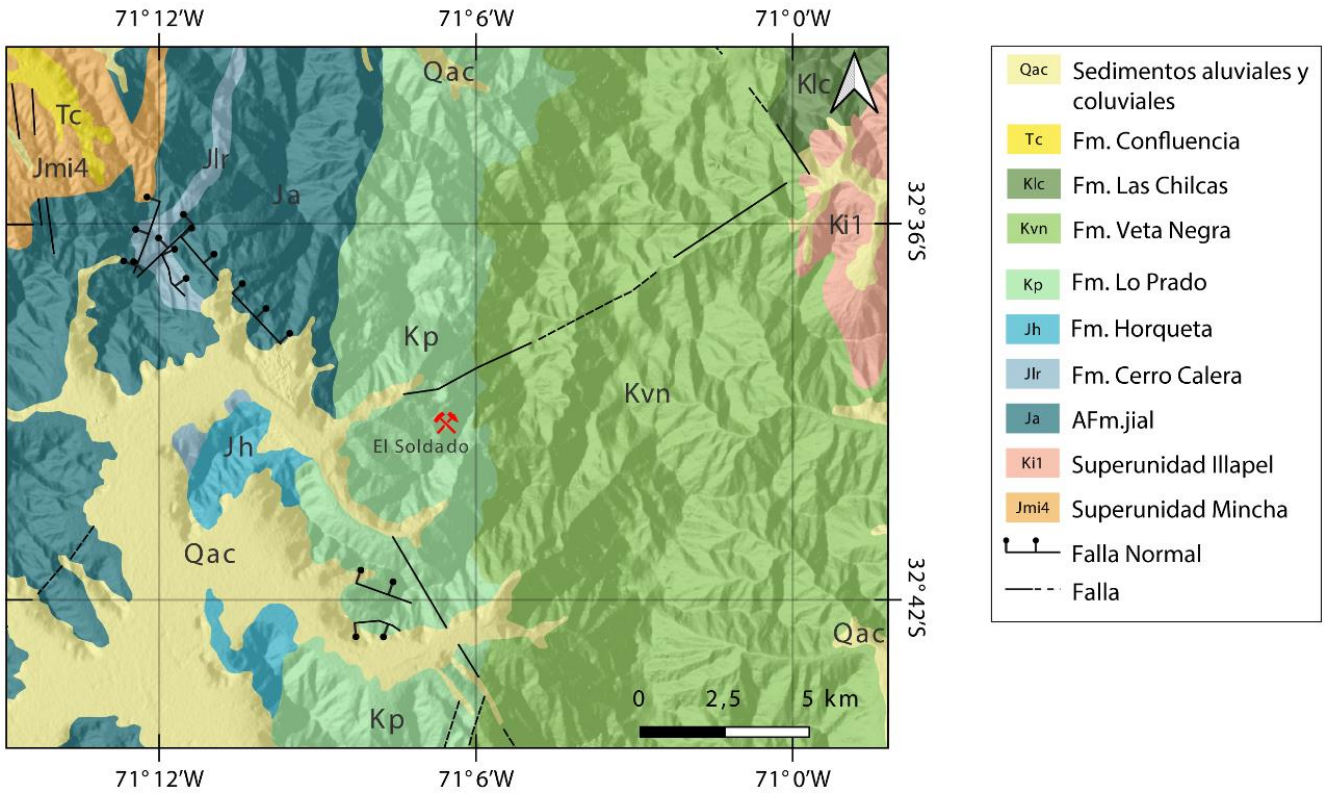

Figura 4. *Geología de la zona de estudio. Modificado de Rivano (1996).*

El sistema descrito se encuentra dentro de un pliegue homoclinal con una inclinación de 30° hacia el este, en donde los manteos disminuyen progresivamente hacia el oriente (Figura 5; Boric et al. 2002). La mineralización se hospeda en una docena de cuerpos mineralizados, distribuidos en un área aproximada de 2 km de largo, 0.8 km de ancho y 600 metros de extensión vertical (Wilson & Zentilli, 1999; Boric et al., 2002). Estos cuerpos mineralizados presentan una zonación característica, la que se encuentra controlada por estructuras preferenciales (Figura 5). La zonación consiste en un núcleo con presencia predominante de bornita-calcosina, y porcentaje menor de especularita, seguido por una zona rica de calcopirita, y una zona externa rica en pirita, la cual es de mayor abundancia en las raíces de los cuerpos mineralizados (Wilson, 1998; Boric et al., 2002). Además, existe una zonación a nivel distrital, con una concentración mayor de bornita, calcosina y bitumen hacia el sur, y mayor abundancia de calcopirita y pirita hacia el sector norte, generando así un aumento en la ley de Cu hacia el sur. Es importante destacar que El Soldado no presenta alteración supérgena intensa, debido principalmente a la ausencia de pirita en las zonas cercanas a la superficie y la abundancia de calcita, carbonatos y bitumen, generando una neutralización de las soluciones ácidas y no permitiendo que se generen procesos de lixiviación intensa (Boric et al., 2002).

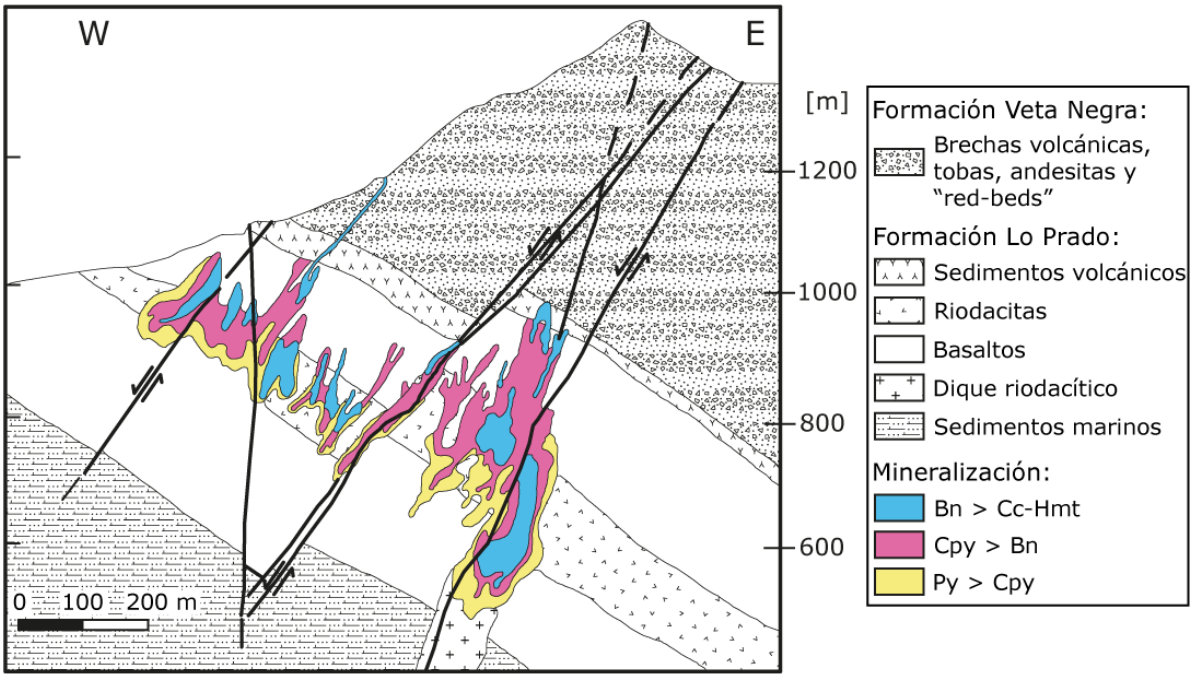

Figura 5. *Sección transversal mostrando las principales unidades rocosas, fallas y zonación mineralógica. Modificado de Boric et al. (2002). Bn: Bornita; Cc: Calcosina; Hmt: Hematita; Cpy: Calcopirita; Py: Pirita.*

Debido a su gran relevancia y envergadura, diversos estudios petrográficos y geoquímicos han sido llevados a cabo en El Soldado. En particular, Zentilli et al. (1994), Zentilli et al. (1997), y Wilson & Zentilli (1999) fueron los primeros que reportaron, y describieron, la presencia de materia orgánica asociada a la mineralización en el depósito, dando los primeros indicios del rol fundamental que juega el (piro)bitumen en su formación. Por otra parte, Wilson & Zentilli (1999) y Boric et al. (2002) identifican dos etapas en la formación del depósito: una primera etapa de pre-mena, entre los 130 y 110 Ma, caracterizada por la presencia de minerales de alteración, bitumen, y pirita framboidal, esta última posiblemente relacionada a un proceso de reducción de sulfato mediante acción bacteriana. Durante esta etapa, las temperaturas probablemente se encontraron entre los 60 y 100°C, restringidas a la presencia de petróleo líquido y a la posible actividad bacteriana. La segunda etapa, también llamada etapa de mena, habría ocurrido aproximadamente a los 103 ± 2 Ma, de acuerdo con edades $^{40}Ar/^{39}Ar$ en feldespato potásico (Wilson & Zentilli, 1999; Wilson et al., 2003b), y habría ocurrido posterior a un evento de diagénesis y a un máximo grado de metamorfismo a los ~110 Ma, y posterior a la intrusión y emplazamiento del Batolito Cretácico. La asociación de esta segunda etapa consiste principalmente en calcopirita, bornita y calcosina, con cantidades menores de hematita, magnetita y covelina. Las temperaturas habrían alcanzado los 300-350°C de acuerdo con estudios de inclusiones fluidas y a la ausencia de fases de alteración de alta temperatura (Holmgren, 1987; Klohn et al., 1990; Boric et al., 2002).

Datos de isótopos estables muestran valores de $\delta^{34}S$ bastante amplios (i.e., -11.1 a +28.0‰; Wilson et al., 2003a) consistentes con un proceso de fraccionamiento bacterial del sulfato. Por otra parte, estudios de inclusiones fluidas realizados en vetillas de cuarzo y calcita indican altas

salinidades para los fluidos hidrotermales (i.e., 21-26 wt.% $NaCl_{equiv}$; Holmgren, 1987; Klohn et al., 1990), lo cual podría implicar la acción de fluidos de cuenca profundos. Sumado a lo anterior, Wilson et al. (2003b) reportan altos niveles de Ar atmosférico, concluyendo que posiblemente exista influencia de aguas meteóricas connatas mezcladas con los fluidos mineralizadores. Por otra parte, análisis isotópicos de Pb realizados en El Soldado y otros depósitos estratoligados de Cu-(Ag) chilenos del centro de Chile (Tosdal & Munizaga, 2003; Kojima et al., 2009) señalan una ligera contribución de los sedimentos cretácicos, a lo que se le suma elevados valores $^{187}Os/^{188}Os$, que indican una posible contribución de Re/Os desde un reservorio cortical, posiblemente lutitas negras (Ruiz et al., 1997; Kojima et al., 2009). Finalmente, valores isotópicos de $\delta^{13}C$ en calcita (i.e., -20.2 a -4.2‰; Wilson et al., 2003a; Kojima et al., 2009) muestran una contribución de carbón biogénico, posiblemente relacionado a la presencia de (piro)bitumen.

Cada uno de estos estudios ha contribuido a un mejor entendimiento del depósito y de los procesos que propiciaron su formación. Dichos estudios indican que la materia orgánica habría jugado un rol fundamental en la mineralización, actuando como una trampa reductora de los complejos transportadores de metales. Además, habría una fuerte contribución de origen sedimentaria a la mineralización, lo cual puede ser corroborada con la signatura geoquímica de las principales fases minerales presentes en el depósito. De manera de contribuir a dichos estudios, en la presente tesis se realiza un análisis petrográfico y geoquímico de bitumen y sulfuros de ganga y mena presentes en El Soldado, de manera de identificar y comprender los procesos que propiciaron la formación del depósito, así como también las posibles fuentes de los fluidos hidrotermales, metales, y posibles herramientas que podrían ayudar a la exploración de zonas de similares características.

1.2. Objetivos

1.2.1. Objetivo general

El objetivo general de la presente tesis es determinar la signatura geoquímica de El Soldado mediante un estudio petrográfico y geoquímico del bitumen, así como de los sulfuros de ganga y mena. Además, se propone comparar las señales geoquímicas de los sulfuros presentes en El Soldado (pirita, calcopirita y bornita) con datos disponibles de otros depósitos estratoligados en Chile y a nivel mundial, así como con depósitos ubicados en la franja metalogénica de la Cordillera de la Costa, de manera de establecer potenciales herramientas exploratorias basadas en la geoquímica de sulfuros.

1.2.2. Objetivos específicos

I. Caracterizar la distribución y concentración de elementos mayores, menores y traza en bitumen, sulfuros de ganga (pirita), y sulfuros de mena (calcopirita, bornita y calcosina) presentes en El Soldado mediante una combinación de técnicas analíticas, incluyendo microsonda electrónica (EPMA), espectrometría de masas por plasma inductivamente acoplado con ablación láser (LA-ICP-MS), y micro-fluorescencia de rayos X (µ-XRF).

II. Identificar las señales geoquímicas de elementos traza presentes en los sulfuros, así como las posibles condiciones fisicoquímicas que propiciaron su concentración en dichos minerales.
III. Examinar el posible rol que ejerce la materia orgánica en la mineralización de El Soldado, mediante un análisis petrográfico y geoquímico del (piro)bitumen.
IV. Evaluar el uso de la geoquímica de elementos traza de los sulfuros como potencial herramienta de vectorización y de exploración hacia sistemas de similares características.
V. Elaborar un modelo genético actualizado de El Soldado, determinando su evolución temporal y contrastándolo con modelos previamente publicados

1.3. Hipótesis de trabajo

La concentración de elementos traza en los sulfuros de El Soldado reflejan la composición del fluido hidrotermal que lo formó, y por tanto, su estudio permite dilucidar el posible origen de éstos. En este contexto, se propone que El Soldado se habría formado a partir de fluidos mineralizadores de diversas fuentes, con una presencia relevante de fluidos de origen sedimentario, en donde la signatura sedimentaria de la etapa de pre-mena habría sido heredada hacia los minerales de la etapa de mena a través de procesos de reemplazo. Además, la materia orgánica habría actuado como agente reductor, sirviendo como una trampa redox para los fluidos hidrotermales y propiciando la precipitación de los sulfuros de Cu-(Fe).

1.4. Metodología

Para cumplir con los objeticos planteados se analizan 50 secciones transparentes pulidas obtenidas de la colección personal del Dr. Marcos Zentilli. Estas muestras son revisadas mediante un microscopio óptico de luz polarizada, modelo Leica DM2700. A partir de esto, se seleccionan 18 muestras representativas de los cuerpos de Osorno, Filo y Santa Clara (Anexo A), utilizando los siguientes criterios: muestras que contengan mineralización de ganga y de mena, presencia de materia orgánica en asociación a los sulfuros, y abundancia de los sulfuros y su paragénesis. Estas muestras son analizadas posteriormente mediante microscopía electrónica de barrido (SEM), utilizando un equipo FEI Quanta 250, ubicado en el Departamento de Geología, Universidad de Chile.

Posteriormente, se obtienen las concentraciones de elementos mayores y menores mediante análisis de microsonda electrónica (EPMA), utilizando un equipo JEOL JXA-85530-F Hyperprobe en el Laboratorio de microsonda de Rice University, Houston, Texas. Con esto, se procede a la obtención de concentración de elementos traza mediante espectrometría de masas por plasma inductivamente acoplado con ablación láser (LA-ICP-MS) en el Laboratorio de Espectrometría de Masas del Departamento de Geología de la Universidad de Chile. Finalmente, de manera de complementar el estudio, se realizan mapas composicionales de granos de bitumen utilizando microfluorescencia de rayos-X (μ-XRF) en el Laboratorio de Nutrición Vegetal de la Universidad de Talca, Chile. En el Anexo B se encuentra el detalle metodológico realizado para el presente trabajo.

1.5. Estructura de la tesis

La presente tesis se organiza en tres capítulos. En el Capítulo 1 se presentan la motivación, objetivos, hipótesis y metodología del trabajo realizado en la presente tesis. En el Capítulo 2 se expone el manuscrito desarrollado durante la investigación, titulado: *"Sedimentary signatures of sulfides from the El Soldado Cu-(Ag) deposit in central Chile"*, el que se presenta en inglés y se encuentra sometido y en proceso de revisión en la edición especial "*Sulphide chemistry of organic-rich sediment-hosted mineral deposits (SEDEX, Sed-Cu, HEBS, VMS): Applications to mineral exploration*" de la revista *Economic Geology*. En este capítulo se presentan los principales resultados obtenidos a lo largo del trabajo, las discusiones generadas y las implicancias para el estudio de este tipo de depósitos. En el Capítulo 3 se presentan las principales conclusiones obtenidas.

Finalmente, el texto de la tesis es complementado con anexos en los que se presentan el resumen informativo de las muestras analizadas (Anexo A), los detalles de la metodología (Anexo B), la base de datos de análisis por microsonda electrónica (EPMA) (Anexo C) y los datos obtenidos mediante espectrometría de masas por plasma inductivamente acoplado con ablación láser (LA-ICP-MS) (Anexo D).

CAPÍTULO 2:

SEDIMENTARY SIGNATURES OF SULFIDES FROM THE BITUMEN-BEARING EL SOLDADO STRATABOUND CU-(AG) DEPOSIT IN CENTRAL CHILE

Camila Alcoholado[1*], Martin Reich[1], Fernando Barra[1], Rurik Romero[1], Gelu Costin[2], Ricardo Cabeza[3]

[1]Department of Geology, Facultad de Ciencias Físicas y Matemáticas (FCFM), Universidad de Chile, Plaza Ercilla 803, Santiago, Chile.

[2]Department of Earth, Environmental and Planetary Sciences, Rice University, 6100 Main St, Houston, Texas, USA.

[3]Plant Nutrition Laboratory, Department of Crop Sciences, Faculty of Agricultural Sciences, University of Talca, Talca 3460000, Chile

*camila.alcoholado@ug.uchile.cl

Submitted to Economic Geology Special Issue: "Sulphide chemistry of organic-rich, sediment-hosted mineral deposits (SEDEX, Sed-Cu, HEBS, VMS): Applications to mineral exploration"

Keywords: *Stratabound Cu-(Ag) deposits, El Soldado, sulfides, (pyro)bitumen, trace element geochemistry, LA-ICP-MS, Coastal Cordillera, central Chile.*

2.1. ABSTRACT

The Early Cretaceous metallogenic belt of the Coastal Cordillera of central-northern Chile comprises a large variety of ore deposits, including iron oxide-apatite (IOA), iron oxide Cu-Au (IOCG), porphyry Cu and stratabound or "Manto-type" Cu-(Ag) deposits. In the latter, sulfide mineralization can occur in close association with residual petroleum or (pyro)bitumen, which raise questions about the source of metals and the role of hydrocarbons in ore formation. In the Coastal Cordillera belt, El Soldado stands out as the largest known stratabound Cu-(Ag) deposit in central Chile, and as a key example of Cu mineralization related to hydrocarbons. Despite its importance as a major source of Cu and Ag, the mineral chemistry of the main sulfide phases, e.g., pyrite, chalcopyrite, bornite and chalcocite, and the source of metals remain unconstrained. In this study, we report a comprehensive geochemical study of sulfides from El Soldado using a combination of petrography,

electron probe microanalysis (EPMA), laser ablation inductively coupled plasma mass spectrometry (LA-ICP-MS) and micro X-ray fluorescence (µ-XRF) analysis. Our results show that El Soldado sulfides incorporated a large variety of trace elements with pyrite being the main carrier, i.e., As (≤ 7,900 ppm), Mn (≤ 3,100 ppm), Cu (≤ 2,950 ppm), Ni (≤ 1,000 ppm), Pb (≤ 760 ppm), Tl (≤ 678 ppm), Co (≤ 285 ppm) and Mo (≤ 62 ppm). Copper-bearing sulfides are characterized by a different suite of trace elements with chalcopyrite containing relevant concentrations of Se (≤ 14,000 ppm), Mn (≤ 2,540 ppm), Pb (≤ 490 ppm), Sn (≤ 24 ppm), Ag (≤ 23 pm) and In (≤ 10 ppm). Similarly, bornite contains Se (≤ 6,800 ppm), Mn (≤ 1,610 ppm), Bi (≤ 530 ppm), Ag (≤ 460 ppm), Mo (≤ 388 ppm), Pb (≤ 322 ppm), V (≤ 110 ppm), Te (≤ 106 ppm) and Tl (≤ 13 ppm). Lastly, chalcocite is relatively poor in trace elements but contains significant concentrations of Fe (≤ 4.41 wt.%) and high Ag concentrations (≤ 0.13 wt.%). Vanadium, Mn, Mo and Tl can reach high concentrations in Cu-(Fe) sulfide phases (up to hundreds of ppm) indicating contributions from sedimentary sources in basinal or marine environments. Microprobe analyses of bitumen reveal high concentrations of S, Cl, Mn, Fe, Cu and Ag, while µ-XRF maps show both homogeneous and irregular distribution of some of these elements at the grain scale (e.g., S, Cl). This suggests that the organic phase may have incorporated those elements through interaction with ore-forming hydrothermal fluids, acting as an important redox trap, but also potentially providing certain components to the ore phases. Trace element ratios of Cu-(Fe) sulfides from El Soldado are compared with geochemical data from other ore deposits including stratabound and sediment-hosted copper deposits, IOCG, IOA and porphyry Cu systems. The Co/Ni (≋ 1) and Mn/Fe (~0.0001 to 0.000001) vs Mo (<100 ppm) relations in pyrite, the In/Se ratio in chalcopyrite (~0.1 to 0.001) and the Ag/Bi ratio in bornite (~100 to 0.1) point to a dominant sedimentary source for these metals in El Soldado, with possible contributions of connate, basinal, marine and/or meteoric waters. The revised genetic model proposed here is consistent with previous studies where three main stages have been identified. The first stage involved the deposition of the volcano-sedimentary sequence and generation of petroleum in the lower member of the Lo Prado Formation. The following stage is characterized by the upward migration of petroleum along structures and formation of bitumen and framboidal pyrite in the upper member of the Lo Prado Formation. The third and last stage comprised the precipitation of the Cu mineralization, primarily chalcopyrite, bornite and chalcocite, derived from externally-sourced hydrothermal fluids that interacted with bitumen and diagenetic pyrite from the host rocks. The proposed model emphasizes the replacement of pre-ore phases in the incorporation of key trace elements, such as Mn, Mo, V, Tl and S into the Cu-(Fe) sulfides. Our data support the use of these geochemical signatures as a discriminator for stratabound Cu mineralization, aiding exploration of new copper resources in the Coastal Cordillera metallogenic belt of Chile, and possibly elsewhere.

2.2. INTRODUCTION

Stratabound Cu-(Ag) deposits, commonly referred to as "Manto-type", occur within a belt of more than 1,000 km along the Coastal Cordillera of central and northern Chile (Fig. 6A). These deposits are of significant economic importance, representing the third largest copper source in Chile, following porphyry copper and iron oxide-copper-gold (IOCG) deposits (Fontboté, 1990;

Maksaev and Zentilli, 2002; Maksaev et al., 2007; Barra et al., 2017). Stratabound Cu-(Ag) deposits are hosted by volcanic and volcano-sedimentary sequences of Upper Jurassic to Lower Cretaceous age, defining two belts based on the age of the deposits and their distinct geological features. In the Upper Jurassic belt, deposits such as Michilla, Buena Esperanza, Mantos Blancos and Las Luces are predominantly found within volcanic rocks of La Negra Formation (Fig. 6A; Oliveros et al., 2008; Reich et al., 2013; Herazo et al., 2020; Maureira et al., 2023). On the other hand, deposits within the Lower Cretaceous belt, which extends further south between Copiapó and Santiago, are hosted in volcano-sedimentary sequences of Pabellón, Quebrada Marquesa or Lo Prado formations, with representative examples including El Soldado, Talcuna and Lo Aguirre (Boric et al., 2002; Saric et al., 2003; Cisternas and Hermosilla, 2006; Wilson and Zentilli, 2006). The sulfide mineralization in stratabound Cu-(Ag) deposits comprises pyrite, chalcopyrite, bornite, chalcocite and minor covellite, which in the case of the Lower Cretaceous deposits, is commonly associated with residual petroleum in the form of (pyro)bitumen (e.g., Zentilli et al., 1997; Wilson and Zentilli, 1999; Wilson and Zentilli, 2006).

Bitumen is a type of hydrocarbon that is soluble in organic solvents (Gaupp et al., 2008). Besides stratabound Cu-(Ag) deposits in Chile and Iran, several studies had demonstrated that the presence of hydrocarbons has great relevance for mineralization and metal enrichment in sediment-hosted systems such as Kupferschiefer Cu, Mississippi Valley-type Pb-Zn, Carlin-type Au and sedimentary Au-U deposits (Parnell et al., 1993; Spirakis and Heyll, 1993; Oszczepalski, 1999; Wilson and Zentilli, 2006; Large et al., 2011; Affouri et al., 2013; Fuchs et al., 2016; Perona et al., 2018; Saintilan et al., 2019; Maghfouri et al., 2020; Movahednia et al., 2022). Consequently, different authors have posited that organic matter plays a crucial role during the mineralization process, acting as a reducing agent for metal complexes and/or having a potential role in transporting metals and ligands (Zentilli et al., 1997; Wilson and Zentilli, 1999; Cisternas and Hermosilla, 2006; Rieger et al., 2008; Migdisov et al., 2017; Herazo et al., 2020). Despite these advances, the precise role of organic matter and sedimentary/basinal fluids in the genesis of Chilean stratabound Cu-(Ag) deposits remains undetermined, with different deposits showing variable degrees of presumable sedimentary contributions. Moreover, the paucity of Cu-(Fe) sulfides geochemical data precludes identification of geochemical signatures that could serve as vectors of this type of mineralization, aiding in the exploration of similar deposits in the Andean province and other tectonic settings.

In the present study we focus on El Soldado, the largest and most prominent of the Manto-type deposits in the Lower Cretaceous belt. The El Soldado deposit contains ~140.7 Mt @ 0.56% Cu (Anglo American, 2022) and is characterized by a distinctive assemblage of pyrite, chalcopyrite, bornite, chalcocite and abundant bitumen. Previous studies have proposed that the deposit was formed as a result of hydrothermal replacement of a biodegraded petroleum reservoir (Klohn et al., 1990; Zentilli et al., 1997; Wilson and Zentilli, 1999; Boric et al., 2002; Wilson et al., 2003a, b). Despite notable progress, very limited geochemical data are available for the different Cu-(Fe) sulfide minerals at El Soldado. This is also the case for several types of sediment-hosted deposits worldwide, where the main focus of study is pyrite, but the Cu-bearing sulfides have been mostly neglected (e.g., Gregory et al., 2015; Mukherjee and Large, 2017; Gregory et al., 2019, Herazo et

al., 2021). This scarcity of data, particularly regarding the trace element signatures of Cu-(Fe) sulfides, has hampered our understanding of the ore-forming processes in these mineral systems.

Here we use a combination of petrographic and microanalytical techniques to examine the major, minor and trace element composition of bitumen, pyrite, chalcopyrite, bornite and chalcocite from El Soldado. Specifically, we collected electron probe microanalyzer (EPMA), laser ablation inductively coupled plasma mass spectrometry (LA-ICP-MS) and micro X-ray fluorescence (μ-XRF) data to determine the grain-scale distribution and concentration of trace elements in order to identify specific geochemical signatures in sulfide minerals and bitumen. Our aim is to contribute to a more comprehensive understanding of the ore-forming processes at El Soldado and to provide new insights into the genetic model for stratabound Cu-(Ag) deposits within the Coastal Cordillera metallogenic province.

2.3. GEOLOGICAL SETTING

The convergent continental margin of western South America has been affected by complex tectonic shifts in the subduction angle during the Early Jurassic to Late Cretaceous (Coira et al., 1982; Mpodozis and Ramos, 1989; Mpodozis and Allmendinger, 1993; Charrier et al., 2007; Charrier et al., 2014; Jara et al., 2021a, b). These geodynamic changes led to the formation of an active magmatism arc and back-arc along the South American margin and diverse types of mineral deposits within the Coastal Cordillera of northern and central Chile, including stratabound Cu-(Ag), iron oxide-apatite (IOA), iron oxide-copper-gold (IOCG), skarn and porphyry Cu systems (Fontboté, 1990; Sillitoe, 2003; Maksaev et al., 2007; Sillitoe, 2010; Knipping et al., 2015; Barra et al., 2017; Ojeda et al., 2024). This morphotectonic configuration developed after a quiescent period of tectonic and volcanic activity along the continental margin between 240 and 194 Ma (Mpodozis and Kay, 1990; Charrier et al., 2007). The reactivation of plate tectonic motion during the Early Jurassic was triggered by the subduction of the Phoenix plate beneath the southwestern margin of Gondwana, generating a roll-back of the oceanic plate and a steep subduction angle. This tectonic regime resulted in extensional deformation at the continental margin, thinning of the continental crust, intense magmatic activity along the arc, formation of intra-arc basins between 28–35°S and back-arc basins between 21–27°S, and marine transgression-regression events to the east of the continental arc (Mpodozis and Ramos, 1989; Charrier et al., 2007; Oliveros et al., 2020; Jara et al., 2021a, b). This configuration prevailed until the beginning of the Late Cretaceous with the onset of a compressive stress regime related to a decrease in the subduction angle (Charrier et al., 2007), and an increase in the rate of oceanic crust production, probably associated with the mid-Cretaceous superplume (Larson, 1991; Larson and Kincaid, 1996; Tatsumi et al., 1998; Utsunomiya et al., 2007). This major tectonic stage, known as the Peruvian Phase (Steinmann, 1929; Charrier and Vicente, 1970; Reutter, 2001), led to the tectonic inversion of the previously formed basins, as well as the migration of the volcanic arc towards the east and the cessation of the volcanic activity in the western margin of South America (Coira et al., 1982; Mpodozis and Ramos, 1989; Ramos and Aleman, 2000; Maksaev and Zentilli, 2002; Charrier et al., 2007; Charrier et al., 2014).

The El Soldado stratabound Cu-(Ag) deposit, located 120 km north of Santiago (Fig. 1A), is hosted by volcano-sedimentary rocks of the upper member of the Early Cretaceous Lo Prado Formation (~145–133 Ma; Nasi and Thiele, 1982; Rivano, 1993; Aguirre et al., 1999; Fuentes et al., 2005). This unit corresponds to a 500 meter-thick sequence comprising felsic and basaltic lava flows, which occur interlayered with sedimentary and volcaniclastic rocks composed of calcilutites, calcarenites, breccias and conglomerates (Fig. 6B; Thomas, 1958; Piraces and Maksaev, 1977; Holmgren, 1987; Rivano, 1993; Boric et al., 2002). The upper member of the Lo Prado Formation was deposited in a subsiding extensional setting during the Early Cretaceous (Aberg et al., 1984; Vergara et al., 1995; Boric et al., 2002; Maksaev and Zentilli, 2002; Charrier et al., 2007; Boyce et al., 2020), as evidenced by plagioclase $^{40}Ar/^{39}Ar$ ages ranging ~123 and 119 Ma (Boric and Munizaga, 1994; Morata et al., 2006). The lower member of the Lo Prado Formation (Wall et al. 1999; Sellés and Gana, 2001), is a marine sedimentary sequence of Berriasian age composed of shales, siltstones, sandstones, calcareous arenites and organic matter that has an estimated thickness of about 1,500 m (Boric et al., 2002). The Lo Prado Formation is underlain by volcaniclastic rocks of the Early Jurassic to Middle Jurassic Horqueta Formation (Thomas, 1958; Rivano, 1993), and is overlain by volcanic rocks with intercalations of sedimentary rocks of the Cretaceous Veta Negra Formation (Thomas, 1958). The formation of this volcano-sedimentary sequence occurred in a transitional environment between terrestrial and marine zones representing the magmatic arc developed on the western margin of the South American continent. This is consistent with deposition in subsidence environments and extensional conditions (Aberg et al., 1984; Vergara et al., 1995; Boric et al., 2002; Charrier et al., 2007; Boyce et al., 2020).

The volcano-sedimentary sequence is disposed in a homoclinal structure with a 30°E dip (Fig. 6C). Deformation in the area is dominated by NS-NNW sinistral strike slip faults and by normal reactivated faults with dips of ~60°W (Boric et al., 2002). Plutonic rocks in the El Soldado area outcrop more than 10 km to the east of the mineralized bodies and correspond to intrusive rocks of mafic to intermediate composition of Jurassic to Cretaceous age apparently unrelated to the “Manto” mineralization (Rivano, 1993; Boric et al., 2002; Kojima et al., 2009).

2.4. GEOLOGY, ALTERATION AND MINERALIZATION

The El Soldado deposit consists of about a dozen of vein-like mineralized bodies, namely Morro, Catedral, Santa Clara, California, Arauco, Christine, Valdivia, Malvas, Osorno, Filo, encompassing an area of ~2 x 0.8 km^2 and extending vertically for ~600 m (Wilson and Zentilli, 1999; Boric et al., 2002). The ore bodies are mainly distributed along a NS to NNW-trending regional structural system consisting of strike-slip faults with a left-lateral motion and reactivated normal fault with dips of 60°W (Boric et al., 2002). The ore bodies are considered as “stratabound” because the mineralization is mostly contained within stratigraphic units, i.e., the upper member of the Lo Prado Formation. However, at a local scale these bodies are mostly discordant with a strong structural (feeder zones) and lithological (permeable strata) control (Klohn et al., 1990; Wilson and Zentilli, 1999; Boric et al., 2002). The sulfide mineralization at El Soldado is intimately associated

with (pyro)bitumen and consists of pyrite, chalcopyrite, bornite, chalcocite and minor amounts of covellite and digenite (Zentilli et al., 1997; Wilson and Zentilli, 1999; Boric et al., 2002).

Previous studies on the deposit identified two stages of formation, a pre-ore stage between ~130 and 110 Ma, and a Cu ore stage at ~110–90 Ma (Wilson and Zentilli, 1999; Boric et al., 2002; Wilson et al., 2003b). The pre-ore stage is characterized by a Ca-Na alteration with abundant calcite, K-feldspar, chlorite, epidote, prehnite, pumpellyite, quartz and albite, similar to low-grade regional metamorphism assemblages formed by burial of sedimentary sequences. Diagenetic pyrite is the main sulfide in this stage and is commonly observed with framboidal or rosette-shaped textures closely associated with (pyro)bitumen. The following Cu ore stage is characterized by the presence of Cu-(Fe) sulfides, e.g., chalcopyrite, bornite, chalcocite, digenite and covellite, which replaced the pre-existing pyrite. The ore sulfides are associated with a sodic and potassic alteration represented by calcite, K-feldspar, chlorite, quartz, albite and epidote (Boric et al., 2002). During this stage, the excess of Fe generated by pyrite replacement by Cu-(Fe) sulfides led to the formation of abundant hematite. At the deposit scale, the Cu-(Fe) sulfide mineralization is centered around faults (feeder zones) and display a concentric zonation where the central zone contains bornite, chalcocite and hematite, grading outward to a zone of bornite and chalcopyrite. The outermost zone is characterized by abundant diagenetic pyrite with hydrothermal pyrite precipitated during the ore stage (Fig. 6C; Wilson and Zentilli, 1999; Boric, 2002; Boric et al., 2002). It is important to note that chalcocite and digenite are primary (hypogene) and although oxidized zones do exist near the surface, supergene enrichment was not significant due to the high abundance of calcite and the lack of pyrite in the upper levels of the deposit (Wilson, 1998; Boric et al., 2002).

Fluid inclusion and stable isotope studies have provided some constraints on the formation conditions of El Soldado. The pre-ore stage is interpreted to have occurred when liquid hydrocarbons (petroleum) were generated in the lower member of the Lo Prado Formation, and later migrated into the upper member. The oil formation and migration likely occurred at temperatures between 60 and 100°C, based on oil-window temperatures and the involvement of bacterial activity— fundamental for the generation of framboidal pyrite (Wilson and Zentilli, 1999; Boric et al., 2002). The pre-ore stage has not been dated precisely due to the absence of suitable minerals for geochronology, but based on its stratigraphic level, i.e., after the formation of the upper member of the Lo Prado Formation, it has an estimated age between ~145 and 133 Ma (Nasi and Thiele, 1982; Rivano, 1993; Aguirre et al., 1999; Fuentes et al., 2005). On the other hand, the timing of the main Cu stage has been determined at 103 ± 2 Ma (K-feldspar $^{40}Ar/^{39}Ar$ age) possibly coeval with the emplacement of the Cretaceous batholith (Wilson et al., 2003b). The temperatures attained during the Cu mineralization stage were inferred at ~300–350°C based on the absence of high-temperature alteration assemblages and the study of fluid inclusions in calcite and quartz (Holmgren, 1987; Klohn et al., 1990; Wilson and Zentilli, 1999; Boric et al., 2002; Kojima et al., 2009).

Stable isotope data show a wide range of $\delta^{34}S$ values (–11.1‰ to +28.0‰), which is consistent with bacterial fractionation of sulfur (Boric et al., 2002; Wilson et al., 2003a). Holmgren (1987) and Klohn et al. (1990) carried out fluid inclusion studies in calcite and quartz veinlets and reported high salinities (21–26 wt.% $NaCl_{equiv}$), indicating involvement of basinal brines during the

formation of the Cu mineralization. Lastly, fission-track data in apatite suggest a cooling trend from ~300°C, after mineralization, to less than ~100°C at ~90 Ma. In addition, high levels of atmospheric Ar in K-feldspar point to the possible presence of meteoric or connate waters mixed with mineralizing fluids of possible sedimentary origin (Wilson et al., 2003b).

2.5. SAMPLES AND METHODS

2.5.1. Samples and petrography

Fifty drill core samples and their respective polished thin sections were obtained from the personal collection of Dr. Marcos Zentilli, which is the most comprehensive and well-documented sample set available for El Soldado. Detail description of these samples is reported in the Nicholas Wilson's PhD dissertation (Wilson, 1998). Eighteen samples were selected for major, minor and trace element analysis of sulfides and bitumen (App. A). The selection criteria included representative samples of pre-ore and main Cu mineralization, presence of organic matter (bitumen) and abundance of Cu-(Fe) sulfides. The selected samples were studied using transmitted and reflected polarized light microscopy and scanning electron microscopy (SEM). The SEM analyses were carried out with a FEI Quanta 250 instrument at the Department of Geology, Universidad de Chile. The SEM is equipped with secondary electron (SE), backscattered electron (BSE), and energy dispersive X-ray spectrometry (EDS) detectors. The analytical conditions were an accelerating voltage of 20 kV, a spot size of 5 µm and a working distance of 10 mm.

2.5.2. Electron probe microanalysis (EPMA)

The concentration of major, minor and trace elements in the sulfide phases (pyrite, chalcopyrite, bornite and chalcocite) and bitumen was determined using a JEOL JXA-85530-F Hyperprobe at the EPMA Laboratory, Rice University in Houston, Texas. The Cu-(Fe) sulfides phases were analyzed using the following conditions: an accelerating voltage of 15 kV, a beam current of 150 nA for all sulfides, and a beam diameter of 500 nm for pyrite and chalcopyrite, 10 µm for bornite and 700 nm for chalcocite. The sub-micron spatial resolution capabilities of the Hyperprobe allowed the analysis of fine-grained sulfides. Bitumen, in turn, was analyzed using an accelerating voltage of 15 kV, a beam current of 50 nA, and a beam diameter between 400 nm to 2 µm. Additional analytical conditions include (i) sulfides: PETJ for S (Kα), LIFL for Mn (Kα), LIF for Co (Kα), Fe (Kα), LIFH for Ni (Kα), Zn (Kα), PETH for Ag (Lα), Au (Mα), TAP for Se (Lα), As (Lα), Cu (Lα), and PETL for Te (Lα), Sb (Lα), Bi (Mα) and Pb (Mα), (ii) bitumen: LDE2 for C (Kα), PETJ for Ag (Lα), Sb (Lα), Ca (Kα), TAP for Zn (Lα), Cu (Lα), As (Lα), LIF for Fe (Kα), PETH for P (Kα), LIFH for Cr (Kα), Co (Kα), LED1 for O (Kα), PETL for S (Kα), Mo (Lβ), and LIFL for Mn (Kα). Calibrations were performed using (i) sulfides: ZnS (for Zn), Bi_2Se_3 (for Bi and Se), $Mn^{2+}SiO_3$ (for Mn), FeS_2 (for S), Sb_2S_3 (for Sb), $CuFeS_2$ (for Fe and Cu), Ag^0 (for Ag), Au^0 (for Au), FeAsS (for As), PbS (for Pb), Te^0 (for Te), $Mn^{2+}SiO_3$ (for Mn), Co^0 for Co, $(Ni, Fe)_9S_8$ (for Ni), (ii) bitumen: C^0 (for C), synthetic Ag^0 (for Ag), ZnS (for Zn), $CaMg(CO_3)_2$ (for Ca), $(Mg, Fe)_2SiO_4$ (for Fe), Sb_2S_3 (for Sb), P_2O_5 (for P), $FeCr_2O_4$ (for Cr), Co^0 (for Co), Fe_3O_4 (for O),

$CuFeS_2$ (for Cu), FeAsS (for As), FeS_2 (for S), Mo^0 (for Mo) and $Mn^{2+}SiO_3$ (for Mn). Mean detection limits for most elements were: 93–170 ppm (pyrite), 230 ppm and 0.21 wt.% (chalcopyrite), 24 ppm and 0.32 wt.% (bornite) and between 70 ppm and 0.110 wt.% (chalcocite). For bitumen, the mean detection limit ranged between 14 ppm and 0.125 wt.%. Lastly, wavelength dispersive spectrometry (WDS) X-ray maps were performed in pyrite and chalcopyrite using an accelerating voltage of 15 kV and a beam current of 50 nA. EPMA results for each of the phases are reported in Appendix C.

2.5.3. Laser ablation inductively coupled plasma mass spectrometry (LA-ICP-MS)

Laser ablation inductively coupled plasma mass spectrometry (LA-ICP-MS) was used to determine the concentration of trace elements in sulfide grains previously analyzed with EPMA. The analyses were carried out at the Mass Spectrometry Laboratory of the Department of Geology, Universidad de Chile, using a 193 nm ArF excimer laser coupled to a quadrupole ICP-MS (Thermo Fisher Scientific iCAP Q). Before sample analysis, the NIST SRM 610 reference material was ablated to ensure optimal levels of plasma robustness (i.e., $^{232}Th^+/^{238}U$ between 0.9 and 1), oxide production (i.e., $ThO^+/Th^+ < 0.6\%$) and double charged production (i.e., $^{22}M^+/^{44}Ca^{2+} < 0.05\%$). The spot size was 40 µm but a 25 µm spot was used in smaller grains or to avoid fractures, scratches and mineral inclusions. Each spot was ablated for 52.5 s with a background counting time of 30 s. The analysis was performed using a laser pulse frequency of 4 Hz, a fluence of 2.5 J/cm^2. Internal and external standards were used for calibration and data processing (Longerich et al., 1996). The MASS-1 synthetic sulfide reference material was used as the primary external standard (Wilson et al., 2002), and the GSE-1 glass as a secondary standard and quality control (Jochum et al., 2005). The Fe concentration previously obtained by EPMA was used as internal standard. Primary and secondary external standards were measured at the beginning and end of each round of analysis of about 15 to 20 spots. The analyzed isotopes were: ^{34}S, ^{51}V, ^{52}Cr, ^{53}Cr, ^{55}Mn, ^{59}Co, ^{60}Ni, ^{63}Cu, ^{65}Cu, ^{66}Zn, ^{69}Ga, ^{72}Ge, ^{73}Ge, ^{75}As, ^{77}Se, ^{82}Se, ^{95}Mo, ^{97}Mo, ^{107}Ag, ^{109}Ag, ^{111}Cd, ^{115}In, ^{118}Sn, ^{120}Sn, ^{121}Sb, ^{123}Sb, ^{125}Te, ^{195}Pt, ^{197}Au, ^{202}Hg, ^{205}Tl, ^{206}Pb, ^{207}Pb, ^{208}Pb, ^{209}Bi. The median detection limits are reported in Appendix D, and only data above the detection limit of the instrument were used for the analysis.

2.5.4. Micro X-ray fluorescence (µ-XRF)

Elemental mapping of (pyro)bitumen was carried out at the Plant Nutrition Laboratory of the University of Talca, Chile, using a Bruker M4 Tornado Plus micro X-ray fluorescence spectrometer**,** equipped with a rhodium target X-ray tube that operates at 50 kV and 600 µA. The instrument is equipped with an XFlash silicon drift, and no filter was used for the analysis. The beam size and distance between spots was 20 µm for better resolution. Polished thin sections were scanned for Cu, S, Fe, Cl and Ca. µ-XRF images were processed by using the ESPRIT image acquisition software.

2.6. RESULTS

2.6.1. Mineral assemblages and paragenesis

Mineralization at El Soldado is divided in two main stages: a pre-ore and a main Cu ore stage (Wilson and Zentilli, 1999; Boric et al., 2002). The pre-ore assemblage is characterized by hydrothermal minerals including calcite, chlorite, epidote, albite, K-feldspar, quartz, sericite and clays (Sato, 1984; Sillitoe, 1992). In addition, zeolites, prehnite and pumpellyite— possibly of metamorphic origin— are commonly found filling vesicles in the host rocks. Hydrothermal minerals are observed either replacing the primary silicate mineralogy or filling veinlets and fractures. In the pre-ore assemblage, bitumen displays typical textures of cracking (Figs. 7A, B, 8A-D), where fractures and pores are filled by calcite, prehnite, quartz and bornite (Figs. 7A, 8A). Diagenetic pyrite is present as framboidal grains <50 µm, disseminated in the groundmass (Fig. 7C), and surrounded by hydrothermal pyrite (Fig. 8C), bornite (Figs. 7D, 8E) or bitumen (Fig. 8D).

The main ore assemblage is characterized by replacement textures dominated by Cu-(Fe) sulfides (Figs. 7, 8). The most important ore sulfides are chalcopyrite, bornite and chalcocite, and are observed filling veinlets, amygdales and bitumen fractures, and also as disseminated grains within the host rock. Pyrite is also found in this stage, forming euhedral grains ranging in size from ~20 and 100 µm surrounded by chalcopyrite (Figs. 7B, 8B). In addition, pyrite is observed as large aggregates being replaced by chalcopyrite in fractures (Fig. 7E), surrounded by bitumen (Fig. 7B), surrounding framboidal pyrite from the pre-ore stage (Fig. 8C), and as rosette forms with sizes ~1 mm (Fig. 8F).

Chalcopyrite is observed surrounding small euhedral pyrite grains, replacing pyrite, replaced by bornite (Figs. 7, 8), and forming aggregates ranging in size between 100 and 1,000 µm. Bornite is commonly found filling fractures within bitumen (Figs. 7A, 8A), associated with chalcopyrite (Figs. 7F, 8G-I), as veinlets (Figs. 7D, 8G), disseminated in the host rock (Fig. 7F), and forming aggregates 50 to ~500 µm in size. Bornite can also be replaced by chalcocite and occasionally by covellite (Fig. 7D). In addition, and as reported in literature (Holmgren, 1987; Boric et al., 2002), the excess Fe generated by the progressive replacement of pre-existing pyrite led to the formation of hematite on the rims of some Cu-(Fe) sulfide grains (Fig. 8H).

The proposed paragenetic sequence of hydrothermal alteration and mineralization is presented in Figure 9.

2.6.2. Major, minor and trace element geochemistry

All EPMA and LA-ICP-MS data of the analyzed samples are reported in Appendices C and D. Boxplots for bitumen, pyrite, chalcopyrite, bornite and chalcocite are shown in Figure 10 and bitumen µ-XRF maps are presented in Figure 11. WDS maps of selected sulfides grains are shown in Figure 12.

2.6.2.1. Bitumen geochemistry (pre-ore assemblage)

Bitumen analyses yielded C and O concentrations between 91.05–95.51 and 2.35–5.21 wt.%, respectively (App. C). In addition, S (median = 0.772 wt.%), Ca (median = 0.042 wt.%), and Fe (median = 0.137 wt.%) were detected in all spots, whereas Mn, Cu and Ag were measured in more than 60% of the analyses with median concentrations of 82, 232 and 256 ppm, respectively (Fig. 10A). Phosphorous, Cr, Co, Zn, Mo and Sb are present in less than 25% of the analyses with median concentrations <150 ppm. Bitumen was not measured by LA-ICP-MS, due to the absence of an appropriate external standard and potential carbon contamination of the mass spectrometer lines.

The elemental distribution in bitumen was mapped using µ-XRF (Fig. 11). Chemical imaging of bitumen grains shows the presence of S, Cu, Cl, Fe, Ca, Tl and As. Sulfur is found homogeneously distributed within bitumen grains (Figs. 11B, G). Copper and Fe were not detected in bitumen, although Cu-(Fe) sulfides are observed filling fractures or as overgrowths on some grains (Figs. 11C, E, J). Chlorine is homogeneously distributed within (pyro)bitumen (Figs. 11D, J), and Ca is observed within fractures reflecting the presence of calcite (Fig. 11E). Other elements such as Tl and As are homogeneously distributed in bitumen but at relatively low concentrations (Figs. 11H, I).

Elemental analysis of framboidal pyrite from the pre-ore stage was complicated by the small grain size (<5 µm; Figs. 7C-D, 8C-E), porous texture and matrix effect. Therefore, no reliable EMPA and LA-ICP-MS data (>95 wt.% total) were obtained for the diagenetic pyrite.

2.6.2.2. Geochemistry of pyrite and Cu-(Fe) sulfides (main Cu assemblage)

Pyrite from the ore stage is represented by euhedral and large aggregates (Figs. 7B, 8B). EPMA data show that S and Fe range between 50.39 and 53.50 wt.% and from 44.44 to 46.69 wt.%, respectively (App. C). Cobalt, Cu, As and Au were detected in most spots with median concentrations of 614, 532, 1,010 and 757 ppm, respectively (segmented lines, Fig. 10B). High As (up to 1.93 wt.%) coupled to low S concentrations (~50.39 wt.%) were measured in euhedral pyrite grains (App. C). Manganese, Ni and Ag were detected in more than 30% of the spots with median concentrations of 289, 157 and 130 ppm, respectively (segmented lines, Fig. 10B). Selenium, Sb and Te were rarely detected. WDS X-ray maps on euhedral pyrite grains show a distinct zonation with As-rich/S-poor bands and S-rich/As-poor areas (Figs. 12B-D, F-H). Copper was not detected in these pyrite grains.

Trace element concentrations in pyrite were further investigated by using LA-ICP-MS. In most spots the following elements were systematically detected (App. D; Fig. 10B): Mn (9.1–3,100 ppm), Cu (62.1–2,950 ppm), As (24–7,900 ppm), Mo (2.5–61.9 ppm), Ag (0.81–8.9 ppm) and Pb (1.33–760 ppm). Cobalt, Ni, Zn and Tl were detected in ~50–60% of the analyses with maximum concentrations of 285, 1,000, 193 and 678 ppm, respectively (Fig. 10B). All other elements reached concentrations below 100 ppm and were only detected in a few spots (App. D). Notably, Au was detected in almost 40% of the analyses (App. D). However, unlike the results from EPMA (App. C), the concentrations reached a maximum of approximately 0.13 ppm. This discrepancy may be

attributed to differences in beam size between the two techniques, likely causing a dilution effect in the LA-ICP-MS analyses when detecting clusters of micro-to nano-sized Au inclusions.

Chalcopyrite, bornite and chalcocite have significant concentrations of different trace element (i.e., 10' to 1,000's of ppm), while chalcocite is host of only minor amounts of these (Figs. 10C-E). EPMA data of chalcopyrite show slight variations in the concentration of Cu (33.43–36.18 wt.%), Fe (29.38–31.52 wt.%), and S (34.62–35.65 wt.%) (App. C). Zinc, Ag and Au were detected in 63% to 82% of the spots with median concentrations of 480, 141 and 580 ppm, respectively (Fig. 10C). Selenium, Pb and Bi were detected in ~20% of the analyses with median concentrations of 45, 2,838 and 129 ppm, respectively, whereas As, Sb and Te were observed in less than 15% of the analyses with concentrations below 100 ppm.

LA-ICP-MS data of chalcopyrite show that indium was detected systematically with concentrations ranging from 2.1 to 9.8 ppm (Fig. 10C). Lead was detected in almost 80% of analyses with concentrations between 0.1 and 490 ppm. Chromium (16–220 ppm), Mn (26–2,540 ppm), Se (89–14,000 ppm), Ag (4.5–23 ppm) and Sn (8.5–23.7 ppm) were detected in several spots (~25–60% of the analyses), while V (20–80 ppm) and Au (0.02–0.8 ppm) were observed in ~25% of the spots (Fig. 10C). Cobalt, Sb, Te and Bi were measured in 10–20% of the points, with median concentrations below 30 ppm (Co: 14–140 ppm, Sb: 10.3–26 ppm, Te: 1.7–23 ppm, Bi: 0.21–6.5 ppm). All other elements were detected in less than 10% of the cases with most concentrations falling below the detection limit (App. D; Fig. 10C).

EMPA data show that bornite has variable concentrations of Cu (56.17–68.31 wt.%), Fe (7.97–15.49 wt.%), and S (24.97–29.30 wt.%) (App. C). Other metals including Zn (up to 1,905 ppm) and Ag (up to 1,659 ppm) were detected in more than 50% of the spots (Fig. 10D). Gold and Bi were detected in more than 25% of the spots with median concentrations of 149 and 93 ppm, respectively. Median concentrations of Mn (114 ppm), As (45 ppm), Se (46 ppm), Sb (40.5 ppm), Te (46.5 ppm) and Pb (1,888 ppm) vary between 10's to 100's of ppm. However, Mn, As and Pb are observed with high concentrations reaching up to 951, 3,743 and 2,342 ppm, respectively. Minor and trace elements were further analyzed using LA-ICP-MS (Fig. 10D). Silver (25–460 ppm), Pb (0.27–322 ppm) and Bi (2–530 ppm) were detected in more than 80% of the spots. Thallium was measured in almost 50% of the analyses with concentrations ranging from 0.09 to 13.4 ppm. Manganese, Se and Te display the higher concentration values in the dataset, i.e., Mn (14.9–1,610 ppm), Se (50–6,800 ppm, with one outlier up to 90,000 ppm) and Te (1.2–106 ppm, with outliers up to 2,100 ppm) (Fig. 10D). All other elements have concentrations below 200 ppm and are detected in less than 30% of the points (App. C; Fig. 10D). It is important to mention that, as in the case of pyrite, the differences in Au concentrations in EPMA and LA-ICP-MS in chalcopyrite and bornite may be due to an effect of the incident beam size, a possible effect of dilution and presence of mineral inclusions.

Lastly, the concentration of major and minor elements in chalcocite was determined only by EPMA (App. C; Fig. 10E), due to its small grain size (<30–40 µm) and to its intimate textural association with bornite. EPMA data show values for Cu and S ranging from 74.43 to 80.33 wt.% and 19.83 to 22.59 wt.%, respectively. Iron and Ag were measured in all spots indicating that this

sulfide is a major repository for Ag. Iron concentrations range from 0.41 to 4.41 wt.%, while Ag contents are significantly high reaching the 1,000 ppm-level (0.02–0.13 wt.%). The rest of the analyzed elements were detected in less than 30% of the cases, i.e., Co (520 ppm), As (310 ppm), Se (450 ppm), Sb (490 ppm) and Pb (3,080 ppm) (median concentrations; Fig. 10E). Re-calculation of the chemical formula for all data points (n = 23) yielded an average value of approximately 1.98 atoms per formula unit of Cu per each S (i.e., $Cu_{1.98}S$). The cationic proportion ranges between djurleite ($Cu_{1.94}S$) and chalcocite (Cu_2S), hence, the formal end-member term chalcocite is used throughout the text.

2.7. DISCUSSION

Sulfide minerals incorporate trace elements in a variety of forms, including solid solution (Fleet et al., 1989; Reich et al., 2005; Deditius et al., 2014), deformation-related dislocations (Dubosq et al., 2019; Fougerouse et al., 2021; Verberne et al., 2022), and through the formation of mineral nanoparticles or nanophases (Cook and Chryssoulis, 1990; Reich et al., 2006; Hochella et al., 2008; Deditius et al., 2011; Ciobanu et al., 2012; Ehrig et al., 2023). Identifying the different mechanisms of incorporation of trace elements in sulfides is important to understand the partitioning behavior of metal(loid)s through ore genesis, the enrichment (or depletion) during hydrothermal alteration and to track the physicochemical conditions of the mineralizing fluids (e.g., T-X-pH-fO_2-fS_2). Furthermore, sulfides such as pyrite, chalcopyrite, bornite and chalcocite are ubiquitous in diverse types of ore deposits including porphyry Cu, epithermal Au-Cu, stratabound Cu-(Ag) and IOCG deposits, hence, their geochemical composition can be useful to trace metal sources and as a potential tool for mineral exploration as documented, for example, in the Andean province (Reich et al., 2016; Román et al., 2019; Crespo et al., 2020; Herazo et al., 2021; Rivas-Romero et al., 2021). In the El Soldado stratabound Cu-(Ag) deposit, our data show that pyrite, chalcopyrite, bornite and chalcocite have diverse trace elements with concentrations ranging from parts per million to weight percent levels, some of which are diagnostic of specific environments and/or formation conditions (Apps. C, D; Fig. 10). In the following sections, we discuss the data within the context of sulfide geochemistry and their significance for ore-forming processes in stratabound Cu-(Ag) systems.

2.7.1. Trace element enrichment in pyrite: Tracking a sedimentary source of metals

Hydrothermal pyrite from the ore stage hosts a large variety of trace elements including Cu, As, Tl, Mn, Mo, Co and Ni (Apps. C, D; Fig. 10B). Among those elements, Cu can reach concentrations up to the 1,000 ppm range, suggesting that this metal is either structurally bound or forming micro- to nano-sized inclusions of Cu-bearing minerals. This interpretation is drawn from both a relatively flat (structurally bound element, Fig. 13A) and spiky (inclusions, Fig. 13B) profile in the time-resolved LA-ICP-MS depth plot. Arsenic, on the other hand, has variable concentrations ranging from 24 to 7,900 ppm and does not show a clear negative correspondence with S (App. C), as often reported in the literature. However, substitution of S with As is likely reflected by high As values (up to 1.93 wt.%) that are associated with low concentrations of S (~50.4 wt.%; App. C),

and the occurrence of As-rich and S-poor bands observed in pyrite WDS maps (Figs. 12B, D). The most likely form of incorporation of As in pyrite from El Soldado is in solid solution— interpreted from the relatively flat LA-ICP-MS depth profiles (Figs. 13A, B)— although replacement of S with As^{-1}, and As^{+3} with Fe, or even the presence of nano-scale inclusions of amorphous As-Fe-S cannot be ruled out (Reich et al., 2005; Deditius et al., 2008; Deditius et al., 2009; Deditius et al., 2014; Tardani et al., 2017). In fact, a strong correlation between As and Au in the pyrite structure, where the solubility limit of Au is function of the As content, has been reported for pyrite in other deposit types (Reich et al., 2005; Deditius et al., 2014). In this study, Au was not frequently detected by LA-ICP-MS, with concentrations up to 0.128 ppm. In contrast, Au was detected in several EPMA spots with concentrations up to ~1,000 ppm. This noticeable difference may be due to the smaller spot size of the EMPA technique, which allows a higher spatial resolution to detect micro- to nano-size inclusion clusters. Therefore, Au is most likely present as micro/nano particles and in solid solution (Fig. 14A).

Thallium is an important element in pyrite, with concentrations varying between 12.7 and 678 ppm. The presence of Tl in pyrite has been related to the presence of As, where the incorporation of the latter may distort the crystal structure, generating a space in the Fe d-like valence band, and enhancing the formation of vacancies that promote a stoichiometric or non-stoichiometric substitution of heavy metals such as Tl, Hg or Cd (Chouinard et al., 2005; Deditius et al., 2008; Deditius and Reich, 2016). Our data point to incorporation of Tl in solid solution as reflected by the relatively flat ^{205}Tl profile (Fig. 13B), and the fact that most analyses fall below the solubility limit defined by Deditius and Reich (2016) (Fig. 14B). Thallium is often related to sedimentary and marine environments (Ikramuddin et al., 1986; Deditius and Reich, 2016; Herazo et al., 2021; Erlandsson et al., 2022; Mederski et al., 2022), and can be highly enriched in rocks with organic matter under reducing conditions (Zelenski et al., 2009; George et al., 2019). The sedimentary signature of pyrite from El Soldado is also supported by the presence of Mn, an element that can reach concentrations up to 3,100 ppm (median = 183 ppm; Fig. 10B). Manganese (Mn^{2+}) is apparently incorporated in solid solution based on the relatively flat (but noisy) depth profile (Figs. 13A, B; Jacobs et al., 1985), but the observed Tl and Cu peaks could reflect the presence of inclusions (Fig. 13A). Like Tl, high values of Mn in pyrite have been associated with marine sediments, where it can be absorbed from seawater or local pore water in seafloor muds during pyrite formation (Huerta-Diaz and Morse, 1992; Calvert and Pedersen, 1993; Shikazono et al., 1994; Large et al., 2007; Large et al., 2009; Large et al., 2014; Gregory et al., 2015).

The concentration of Mo in pyrite (2.5–61.9 ppm, median = 18 ppm; Fig. 10B) is also consistent with a sedimentary contribution. The Mo abundance is frequently used as an indicator of euxinic conditions in marine systems (Helz et al., 1996; Helz et al., 2011; Chappaz et al., 2014; Gregory et al., 2015; Siebert et al., 2015). Moreover, research has shown that Mo can be incorporated into organic matter (Huerta-Diaz and Morse, 1992; Helz et al., 1996; Helz et al., 2011; King et al., 2018), further strengthening its association with bitumen in El Soldado. Lastly, pyrite is characterized by Co/Ni ratios $\lessapprox 1$ (Fig. 14C), which are often interpreted as related to low temperature and sedimentary environments (Loftus-Hills and Solomon, 1967; Bralia et al., 1979; Bajwah et al., 1987; Gregory et al., 2015; Reich et al., 2016).

In summary, the occurrence of Cu, As, Tl, Mn, Mo, Co and Ni in hydrothermal pyrite from the main Cu ore stage, which often replaces pre-ore framboidal pyrite associated with bitumen (Fig. 8C), suggests an important contribution from sedimentary sources. This interpretation supports the hypothesis that the deposit formed as a result of the influx of hydrothermal fluids of mixed origin into a biodegraded petroleum reservoir (Wilson and Zentilli, 1999). In addition, it is likely that the above-mentioned trace elements may have been incorporated into the hydrothermal sulfides by replacement of the pre-ore assemblage.

2.7.2. Geochemical signatures of Cu-(Fe) sulfides

Chalcopyrite is host to a variety of trace elements including Pb, Sb, Se, Ag, Mn and In, either in solid solution or in the form of micro- to nano-sized mineral inclusions (Fig. 10C). Selenium can reach concentrations up to the 1,000 ppm range, while Te displays low to intermediate concentrations between ~1 and 23 ppm (Fig. 10C). Several studies have reported that Se and Te are often found in chalcopyrite replacing S^{2-} (Huston et al., 1995; Wohlgemuth-Ueberwasser et al., 2015; George et al., 2018), or forming mineral nano-inclusions. The occurrence of both elements in chalcopyrite has been attributed by several authors to the high solubility exhibited by these elements at moderate to high temperatures (i.e., ~350°C; Auclair et al., 1987; Huston et al., 1995; Butler and Nesbitt, 1999; Wohlgemuth-Ueberwasser et al., 2015), a temperature consistent with reported ore formation conditions at El Soldado (Wilson and Zentilli, 1999; Boric et al., 2002). Indium is another element that is frequently detected and hosted in chalcopyrite (Kieft and Damman, 1990; Huston et al., 1995; George et al., 2016; Carvalho et al., 2018). At El Soldado, indium is ubiquitous with concentrations typically ranging from ~2 to 10 ppm (Fig. 10C). The spiky and irregular LA-ICP-MS depth-concentration profiles (Fig. 13C) indicates that this element may be found as micro- to nano-sized inclusions in chalcopyrite, but a coupled substitution of Fe^{+3} for In^{+3} and Cu^{+} cannot be ruled out (Shannon, 1976; Schwarz-Schampera and Herzig, 2002; George et al., 2018). Indium shows a subtle but discernible positive trend with Se (Fig. 14D), which may be related to the incorporation of both elements within chalcopyrite at temperatures of 350°C (Auclair et al., 1987; Qian et al., 1998; Frenzel et al., 2016; Carvalho et al., 2018). Within this context, it has also been reported that in Cl-rich systems indium can be transported as chloride complexes at temperatures of ~330 to 350°C (Seward et al., 2000; Schwarz-Schampera and Herzig, 2002; Wood and Samson, 2006), and that a decrease in temperature and dilution related to mixing with meteoric waters— as may be the case for El Soldado— may result in complex destabilization and indium incorporation in the sulfide phase.

Our data show that chalcopyrite has low concentrations of Ag (< 23 ppm), compared to other Chilean stratabound Cu-(Ag) deposits such as Mantos Blancos, where chalcopyrite has up to 2,211 ppm of Ag (Reich et al., 2013). Silver in chalcopyrite is possibly related to micro to nano-inclusions of galena as suggested by the tenuous correspondence between Ag and Pb (Fig. 14E), and by the high concentrations of Ag (up to ~1,000 ppm) detected in EPMA (App. C; Fig. 14F). In addition, the subtle correspondence between Cu and Ag may hint at a potential structural substitution between these two elements (Fig. 14F).

Chalcopyrite from El Soldado also contains elements associated with sedimentary environments including V, Mn, Mo and Tl (App. D; Fig. 10C). The presence of V in chalcopyrite has been related to reducing environments, as both elements have low solubility under reducing conditions, indicating an important redox control in its incorporation into sulfides (Mills et al., 1994; Butler and Nesbitt, 1999). Manganese, Mo and Tl, on the other hand, are rarely reported in chalcopyrite and, when present, they are typically associated with submicron-sized inclusions (George et al., 2018, Caraballo et al., 2022). Nevertheless, the occurrence of those elements in chalcopyrite is consistent with a component derived from a marine or basinal sedimentary source and highlights the significance of organic matter as a reducing agent within the deposit (Ikramuddin et al., 1986; Emerson and Huested, 1991; Huerta-Diaz and Morse, 1992; Helz et al., 1996; Large et al., 2014; Gregory et al., 2015; Mederski et al., 2022).

Bornite, the second most abundant Cu-bearing sulfide in the El Soldado deposit, contains Pb, Se, Bi, Ag, Mn, Mo and Tl with similar, or sometimes slightly higher, concentrations in comparison with chalcopyrite (Fig. 10D). In particular, bornite is a prime host for Ag, detected in over 90% of the analyses with concentrations reaching up to 460 ppm. LA-ICP-MS depth profiles suggests that Ag may occur in solid solution and as micro- to nano-sized inclusions (Figs. 13E, F). Furthermore, EPMA data show a broad positive correspondence between Ag and Cu indicating a possible coupling or ionic substitution between both elements (Fig. 14G). However, the wide variation in Ag concentrations (i.e., 10’ to 1,000’s of ppm) (Fig. 14G) in bornite could also indicate the presence of Ag-bearing nano-inclusions such as galena and stromeyerite. Bismuth is another element that is frequently detected in bornite from different ore deposits (Cook et al., 2011), and the consistent presence of this element at El Soldado (Fig. 10D) may be related to its incorporation has solid solution, probably replacing Fe (Crespo et al., 2020), as can be corroborated by the relatively flat (but noisy) depth-concentration profile (Figs. 13E, F), which mimics those of Fe and Cu. Furthermore, bi-variate plots show a broad positive trend of Ag and Bi (Fig. 14H), pointing to structurally related substitutions. It has been reported that simultaneous incorporation of certain elements such as As (or Sb and Bi) can increase the solid solubility of Ag in bornite (Cook et al., 2011; Reich et al., 2013; Kelepile et al., 2020), although the presence of Ag-Bi bearing-inclusions cannot be ruled out.

Trace elements in bornite such as Mo, Mn and Tl also support the notion of a strong contribution from organic and marine sources (e.g., Huerta-Diaz and Morse, 1992; Helz et al., 1996). Molybdenum concentrations range from 1.1 to 388 ppm (Fig. 10D) and show no visible correspondence with other elements. In addition, high Mn concentrations in bornite (14.9–1,610 ppm; App. D; Fig. 10D), are considered anomalous when compared to other deposit types (Cook et al., 2011), where it is commonly related to the presence of mineral inclusions (Brodbeck et al., 2022). In El Soldado, Mn can be associated with solid solution incorporation or mineral inclusions as shown by the time-resolved depth profiles (Figs. 13E, F). Lastly, Tl is detected in most LA-ICP-MS analyses with concentrations ranging between 0.09 and 13.4 ppm (Fig. 5D) and have a slightly similar pattern when compared to the profile of Fe (Fig. 13E), which may suggest that this element is incorporated in bornite structure. However, Tl shows a noticeable correspondence with Pb (Fig. 14I), which probably suggests the presence of Tl-Pb-bearing inclusions. The consistent presence

of Tl in bornite may be related to a sedimentary or marine source— as previously proposed for pyrite and chalcopyrite (Ikramuddin et al., 1986; Deditius and Reich, 2016; Herazo et al., 2021; Erlandsson et al., 2022; Mederski et al., 2022)— and possibly related to organic matter (Zelenski et al., 2009; George et al., 2019).

Lastly, chalcocite is a poor host of trace elements in comparison to the other sulfides (App. C; Fig. 10E), but Ag is consistently detected in all microprobe analyses, often with some of the highest concentrations of the dataset (up to 0.126 wt.%. Fig. 10E). Overall, Ag concentration in chalcocite is almost double the values in bornite from the same sample (up to 0.057 wt.%; App. C), in agreement with previous works on chalcocite–bornite pairs showing that Ag preferentially partitioning into chalcocite while Bi into bornite (Cook et al., 2011; Cioacă et al., 2014). Unlike the other sulfides, chalcocite from El Soldado shows no evidence of elements typical of a sedimentary signature. This may be partly due to the lack of LA-ICP-MS data on chalcocite— due to its small size and its intimate association with bornite— and by its lower content of Fe in comparison with bornite, which may inhibit the incorporation of elements such as Mo, Mn and V in favor of Fe. Finally, the high concentration of Ag in chalcocite, may be due to the higher concentration of Cu in its structure, when compared to bornite, which probably facilitates the incorporation of Ag by replacement of Cu when both minerals co-precipitate.

2.7.3. Elemental ratios in pyrite and Cu-(Fe) sulfides

Sulfide trace element geochemistry allows us not only to identify potential metal sources but can also be used as a tool for ore deposit discrimination and mineral exploration (e.g., Gregory et al., 2015; Mukherjee and Large, 2017; Gregory et al., 2019; Herazo et al., 2021; Rivas et al., 2021). Here we compare the geochemical signatures of the El Soldado Cu-(Fe) sulfides with published data from other mineral deposits, in order to constrain the conditions of ore formation and to provide tools to discriminate between different deposit types.

- Co/Ni ratios in pyrite

It has been proposed that high Co/Ni ratios ($\gtrapprox$ 1) are related to high temperature environments associated with a mafic or ultramafic source— mainly due to the compatible nature of Co and its high concentration in magmas of this nature, derived from partial melting of the mantle— while Co/Ni ratios $\lessapprox$ 1 are linked to low temperature and sedimentary environments (Loftus-Hills and Solomon, 1967; Bralia et al., 1979; Bajwah et al., 1987; Gregory et al., 2015; Reich et al., 2016; Román et al., 2019; Herazo et al., 2021; Rivas-Romero et al., 2021). Furthermore, high Ni values and low Co/Ni ratios have been related to pyrite associated with organic-rich sedimentary rocks (Dill and Kemper, 1990; Scott et al., 2009; Herazo et al., 2021), which is consistent with pyrite data from El Soldado. This is also in agreement with sulfur isotope data for the deposit, which show a wide range of $\delta^{34}S$ values (–11.1 to + 28.0‰; Wilson et al. 2003a). The essential role of hydrocarbons and bacteria in the formation of diagenetic pyrite is corroborated by this signature, and by the wide range of $\delta^{34}S$ values in Cu-(Fe) sulfides of the ore-phase (–12.7 to +19.0‰), which shows that a significant portion of the sulfur of the pre-ore pyrite was recycled with no significant homogenization, fractionation, or addition of new sulfur. This relationship between the

pre-ore and ore phase can also be evidenced by the In/Se and Ag/Bi ratios in chalcopyrite and bornite, respectively (Figs. 15B, C).

Figure 15A shows a comparison of Co and Ni values for pyrite from different ore deposit types from the Coastal Cordillera of northern Chile and southern Peru. IOCG and IOA deposits have a wide range of Co/Ni values (~1,000 to ~0.1; Reich et al., 2016; Li et al., 2017; Li et al., 2018; Rojas et al., 2018; del Real et al., 2020), whereas pyrite from stratabound Cu-(Ag) deposits in Chile display a more narrow range of Co/Ni ratios (~10 to ~0.1) with most points plotting around Co/Ni =1 (Herazo et al., 2021). Pyrite from El Soldado and other stratabound Cu-(Ag) deposits were formed at relatively low to intermediate temperatures, i.e., 150–360°C (Wilson and Zentilli, 1999; Boric et al., 2002; Kojima et al., 2009), while IOCG and IOA deposits form at much higher temperatures, i.e., up to 600 and 850°C, respectively (Chen et al., 2011; del Real et al., 2020; Reich et al., 2022). However, when Co and Ni concentrations of pyrite from Chilean porphyry Cu deposits are considered (Crespo et al., 2020; Rivas et al., 2021), these overlap with the field of Chilean stratabound Cu-(Ag) deposits, suggesting that temperature is not the main control on the concentration of these elements but rather the source of these metals (Vasyukova and Williams-Jones, 2022; Williams-Jones and Vasyukova, 2022).

Pyrite analyses from this study were also compared with data from the Kupferschiefer stratiform (Foltyn et al., 2022) and Iranian "Manto-type" Cu-(Ag) deposits (Sadati et al., 2016), which also have a notable sedimentary signature. In particular, the data from the Kupferschiefer Cu deposits falls within the same range of pyrites from Chilean stratabound deposits, supporting the strong contribution of sedimentary and/or organic matter sources in the formation of these deposits. In summary, the Co/Ni ratios in pyrite from El Soldado are comparable to those of other stratabound Cu-(Ag) deposits (~10–0.1) and are significantly lower when compared to pyrite from IOA and IOCG deposits (Fig. 15A). Our findings underscore the potential of Co/Ni ratios as a tool for discriminating between stratabound Cu-(Ag), IOCG and IOA deposits in the Coastal Cordillera of north-central Chile and southern Peru.

- In/Se ratios in chalcopyrite

It has been reported that the concentrations of In and Se in chalcopyrite are dependent on temperature with a higher solubility associated with high-temperature (>350°C) hydrothermal fluids (Auclair et al., 1987; Qian et al., 1998; Huston et al., 1995; Butler and Nesbitt, 1999; Wohlgemuth-Ueberwasser et al., 2015; Frenzel et al., 2016; Carvalho et al., 2018). Furthermore, it has been studied that an abrupt decrease in temperature caused by mixing of ore-forming fluids with cold meteoric waters may be an effective mechanism for In-chloride complexes destabilization (Seward et al., 2000; Schwarz-Schampera and Herzig, 2002; Wood and Samson, 2006). For this reason, the In/Se ratio in chalcopyrite can be used to discriminate between different temperatures of mineral deposit formation (e.g., Rivas et al., 2021).

The In/Se ratio of chalcopyrite from El Soldado ranges between 0.1 and ~0.005 (Fig. 15B), which differs greatly with reported values for the Kupferschiefer sediment-hosted Cu deposits (In/Se < ~0.0001 to ~ 10; Foltyn et al., 2022). On the other hand, the Brazilian Jaguar IOCG deposit shows chalcopyrite In/Se ratios of ~0.001–1, similar to those from El Soldado, but have much

lower values of In and Se, and are related to higher temperature hydrothermal fluids (Mansur et al., 2023). Indium concentrations in chalcopyrite reported for Chilean Cu porphyry systems (Crespo et al., 2020; Rivas et al., 2021) are also similar to those in El Soldado but the former have higher In/Se ratios (i.e., ~0.01–1; Fig. 15B). Furthermore, the In/Se ratios from El Soldado are similar to those reported for chalcopyrite from the low temperature (~250–350°C) chloritic and quartz-sericite alteration types in the Chuquicamata porphyry Cu deposit (Rivas et al., 2021). The results obtained in this study are not conclusive with respect to the temperature formation of the different deposit types, inferring that in addition to temperature, there may be a redox and pH control in the incorporation of these elements in chalcopyrite (Yamamoto, 1976; Huston et al., 1995). Furthermore, mixing of the hydrothermal fluid with lower temperature meteoric fluids— as proposed for the El Soldado deposit (Wilson et al., 2003a, b)— cannot be ruled out as a mechanism of precipitation of these elements in chalcopyrite,

In addition to the above, high Se contents have been attributed to carbonaceous rocks or oceanic sediments (Loftus-Hills and Solomon, 1967; Schirmer et al., 2014), where high S/Se (>10,000) are associated with shales or sedimentary units (Auclair et al., 1987). The S/Se content determined by EPMA at El Soldado show a median of ~7,800 (App. C), a rather low value when compared with other sedimentary rocks (Auclair et al., 1987), which suggest that the source rock and temperature may not be the only factors controlling the incorporation of Se in chalcopyrite.

- Ag/Bi ratios in bornite

The Ag/Bi ratio in bornite has also been used to discriminate between different temperature assemblages (e.g., Cook et al., 2011; Crespo et al., 2020; Rivas et al., 2021), where it has been reported that bornite may incorporate high amounts of Ag and Bi upon cooling, where low-temperature assemblages have the higher concentrations of both elements (Crespo et al., 2020). This is not fully consistent with the data shown in Figure 15C, where it is shown that bornite from stratabound Cu-(Ag) deposits show much higher Ag/Bi ratios (~100 to 0.1) than IOCG and porphyry Cu deposits (Fig. 10C; Cook et al., 2011; Crespo et al., 2020; Rivas et al., 2021), but are significant lower in comparison with bornite from the Kupferschiefer deposit (Ag/Bi ratios up to ~10,000), mainly because the latter has very low Bi concentrations (<0.2 ppm; Foltyn et al., 2022; Fig. 15C).

The observed differences in the Ag/Bi ratio may be due to the physicochemical conditions of the hydrothermal fluid (T, pH, fO_2-fS_2). For the Kupferschiefer ores, the formation temperatures are estimated between 130 and 200°C (Bechtel et al., 1999; Foltyn et al., 2022). On the other hand, porphyry and IOCG-type deposits generally form at higher temperatures (i.e., ~300–600°C; Gustafson and Hunt, 1975; Hohf et al., 2023; Yu et al., 2024), whereas the estimated temperature for El Soldado Cu mineralization is ~300–350°C (Wilson and Zentilli, 1999; Boric et al., 2002). These differences can also be related to the source of Ag (e.g., magmatic, volcanic host rocks, sediments). In the case of El Soldado, Ag values in bornite are low when compared to Jurassic stratabound deposits (e.g., Mantos Blancos, Las Luces; Reich et al., 2013; Maureira et al., 2023), possibly reflecting different sources (sedimentary vs. magmatic). The differences observed in Figure 15C may also point to a more complex control on Ag incorporation in bornite, where the effect of co-

crystallizing sulfide phases such as chalcocite (Cook et al., 2011)— which is commonly associated with bornite in Chilean stratabound deposits— plays a more relevant role. This characteristic association may be indicative of low formation temperatures for the deposit (i.e., <300°C; Maureira et al., 2023).

2.7.4. Role of bitumen on sulfide mineralization

Our results show that the geochemistry of sulfides from El Soldado record distinctive marine and/or basinal sedimentary signatures. In this context, bitumen may have played a relevant role in the formation of the deposit, where it acted as a redox "trap" and reducing agent, triggering Cu sulfide precipitation by destabilization of chloride-metal complexes (Wilson and Zentilli, 1999; Wilson and Zentilli, 2006). Furthermore, Herazo et al. (2020) proposed that bitumen in the Lorena/Las Luces stratabound Cu-(Ag) deposit (Fig. 6A), might have contributed some sulfur, chlorine and possibly metals (i.e., Fe, Cu, V, among others) during the main Cu ore stage. These elements might have been released from the pre-existing bitumen through its interaction with externally derived Cu-rich hydrothermal fluids. Our EPMA and µ-XRF data of bitumen are comparable to those reported for El Soldado (Wilson and Zentilli, 1999) and Lorena (Herazo et al., 2020). Sulfur concentration in bitumen from El Soldado varies within a narrow range (0.69–0.85 wt.%, median = 0.77 wt.%; App. C), and µ-XRF elemental maps show a homogeneous distribution of this element (Figs. 11B, G), supporting the idea that bitumen inherited sulfur from the interaction of the bitumen-bearing host rock with infiltrating hydrothermal fluids. Despite this, the sulfur isotope data for ore sulfides ($\delta^{34}S$ = –12.7 to +19.0‰) reported by Wilson et al. (2003a) supports a contribution from bitumen and pre-ore pyrite to the Cu-(Fe) sulfides. However, this interpretation requires further investigation.

The presence of chlorine in bitumen from El Soldado was first reported by Wilson and Zentilli (1999) and our µ-XRF maps show that Cl is homogeneously distributed within grains (Figs. 11D, J). These results can be interpreted as the incorporation of Cl into bitumen due to interaction with mineralizing fluids, which likely caused destabilization of Cu-chloride complexes, triggering Cu-(Fe) sulfide precipitation. In addition, EPMA data from bitumen grains also show elevated contents of trace metals (App. C). For example, Cu and Fe concentrations can reach up to 380 and 2,294 ppm, respectively; however, these elements were not observed in the µ-XRF elemental maps (Fig. 11), most likely due to the higher detection limits of this technique. Wilson and Zentilli (1999) reported EMPA concentrations of Cu and Fe of up to >1 wt.% in anisotropic domains of the bitumen. Those authors interpreted these results as the incorporation of base metals from the hydrothermal fluid into the organic phase during the main Cu mineralization stage. Other elements such as Cr, Co, Zn, Mo and Sb were identified only in a few spots (App. C), with the majority of the analyses falling below the detection limit of EMPA. Silver was detected in most EPMA analyses, but it was not observed in bitumen µ-XRF maps. Lastly, Mn concentration in bitumen can reach hundreds ppm and is similar to those values reported for the El Soldado sulfides (App. C; Fig. 10). This high concentration of Mn in bitumen might be related to the oil (petroleum) source, i.e., the lower member of the Lo Prado Formation, where MnO contents reach a maximum of 0.58 wt.% (Boric et al., 2002).

In summary, our results are consistent with previously reported data for El Soldado and other stratabound Cu-(Ag) deposits in the Chilean Coastal Cordillera, where Cu sulfides are found closely associated with bitumen (Cisternas and Hermosilla, 2006; Wilson and Zentilli, 2006; Carrillo-Rosúa et al., 2014; Herazo et al., 2020). We conclude that the presence of metals and ligands in bitumen, as reported here, is most likely the result of the interaction of the organic matter with the infiltrating Cu-rich, externally sourced hydrothermal fluid. This redox trap-fluid interaction resulted in the destabilization of metal-chloride complexes and the consequent Cu sulfide precipitation.

2.7.5. Genetic model for the El Soldado deposit

Four parameters should be addressed in discussing the genetic model of Chilean stratabound or "Manto-type" Cu-(Ag) deposits: the source of fluids, metals and sulfur, and the role of bitumen (Ruiz et al., 1965; Sato, 1984; Fontboté, 1990; Maksaev and Zentilli, 2002; Kojima et al., 2003; Kojima et al., 2009; Oliveros et al., 2008; Maureira et al., 2023). At El Soldado, the primary inquiry revolves around the source of the hydrothermal fluids responsible for the copper mineralization. In this context, it has been suggested that Cu in Chilean stratabound Cu-(Ag) deposits might not be derived from a magmatic source but may be closely related to the circulation of sedimentary/basinal fluids heated by a cooling intrusion at depth (Kojima et al., 2003; Wilson et al., 2003b). The results presented in this study indicate a distinctive sedimentary signature in the sulfides analyzed (pyrite, chalcopyrite and bornite), which is evidenced by the consistent presence of some elements characteristic of this type of environment, particularly in the case of pyrite, which can incorporate significant amounts of Mn, Mo and Tl. A sedimentary contribution to the ore system is also supported by a highly radiogenic initial $^{187}Os/^{188}Os$ ratio of ~4.0 (Ruiz et al., 1997) and by stable isotope data ($\delta^{34}S$, $\delta^{13}C$, $\delta^{18}O$) that suggest that Cu mineralization was likely related to the circulation of basinal and/or meteoric fluids, with little or no magmatic contribution (Kojima et al., 2003; Wilson et al., 2003b).

Further insight on the ore-forming processes and the role of hydrocarbons at El Soldado is provided by the Mn, Fe and Mo content in pyrite. Smrzka et al. (2024) report that Mn/Fe vs. Mo data allow to discriminate pyrite forming in oil or methane seeps. Trace element data from El Soldado and other stratabound deposits show that pyrite was probably formed in a methane-rich environment (Fig. 16), which may indicate variable sulfidic conditions and a process of sulphate driven anaerobic oxidation of methane (Scholz et al., 2013; Smrzka et al., 2024). In contrast, pyrite from oil seeps is characteristic of highly and persistent sulfidic conditions (Scholz et al., 2013; Smrzka et al., 2024), mainly because Mo behaves as a non-conservative element under these conditions and forms bonds with Fe sulfides and S-rich organic molecules (Emerson and Huested, 1992; Huerta-Diaz and Morse, 1992; Scholz et al., 2013). Wilson and Zentilli (1999) reported the presence of abundant degassing vesicles in bitumen from El Soldado, which suggests that the process of petroleum degassing was widespread in the deposit and that methane was dissolved in liquid oil under high pressure conditions, and later exsolved during decompression ascending to the top of the oil reservoir. Hence, both methane and bacterial fractionation of sulfate may have played an important role in the formation of the deposit.

Figure 17 illustrates a modified conceptual model for the formation of the El Soldado deposit based on our new data and previous works (Wilson, 1998; Wilson and Zentilli, 1999; Boric et al., 2002). The first stage of formation was defined by the deposition of the volcano-sedimentary sequence (Lo Prado Formation), its continuous burial under an extensional tectonic regime, and the extrusion of rhyodacites in a shallow marine environment (~145–127 Ma; Fig. 17A). The presence of abundant organic matter in the lower member of this formation, coupled with the ongoing burial processes, facilitated the generation of petroleum. Subsequently, petroleum migrated into the upper member of the Lo Prado Formation through normal faults (Fig. 17B) and accumulated due to the presence of an impermeable layer on the top of the strata (~127–110 Ma; Fig. 17C). It has been proposed that petroleum generation and migration during the pre-ore stage occurred at temperatures ≳60°C according to oil-window temperatures (Wilson and Zentilli, 1999; Boric et al., 2002). Diagenetic (framboidal) pyrite began to form at the accumulation site (or in the source rocks) while petroleum was still liquid. Sulfur stable isotope data indicate that this pyrite would have formed by bacterial sulfate reduction at temperatures below ~100°C (Wilson et al., 1999; Wilson et al., 2003a; Fig. 17C). The large range in $\delta^{34}S$ values of pyrite (–11.1 to +28.0‰) is suggestive of a sedimentary source of sulfur, consistent with pyrite formed by bacterial sulfate reduction, rather than a homogenized igneous or metamorphic source (Wilson et al., 2003a). The progressive burial of the volcano-sedimentary sequence led to increasing temperatures (~120°C), subsequent maturation of liquid petroleum, and finally the formation of bitumen (Fig. 17D). This process is evidenced by (pyro)bitumen $\delta^{13}C$ values ranging from –30 to –26‰, indicating that it is a residue of the original liquid petroleum (Wilson et al., 2003a).

The main stage of Cu mineralization at El Soldado occurred around ~103 Ma and was related to the circulation of hydrothermal fluids of sedimentary and meteoric origin (Figs. 17E, F). Fluids circulated through faults cross-cutting the volcanic and volcaniclastic strata, most likely driven by burial metamorphism and distal magmas related to the emplacement of the Cretaceous batholith. These fluids leached Cu from the host rocks (Veta Negra and Lo Prado Formation; Fig. 17E), and later mixed with meteoric fluids. This is supported $\delta^{13}C$ and $\delta^{18}O$ data in calcite (–4.2 and –20.2‰; Wilson et al., 2003a), which indicate a mixture of oxidized organic carbon derived from bitumen and inorganic carbon from the mineralizing fluid. Furthermore, $^{87}Sr/^{86}Sr$ ratios in calcite from the alteration assemblage (0.7041–0.7051) suggest inheritance from the subaerial andesitic rocks that overlay the deposit, which underwent a leaching process by hydrothermal fluids (Fig. 17E).

The Cu-rich hydrothermal fluids interacted with the pre-ore assemblage, heated the bitumen transforming it into pyrobitumen, and precipitated the main Cu ore assemblage along faults and fractures, mainly by the replacement of the pre-ore assemblage (Fig. 17F). According to Wilson et al (2003a) the $\delta^{34}S$ signature of the ore stage Cu-(Fe) sulfides (–12.7 and +19.0‰) is similar to those of the pre-ore stage pyrite (–11.1 to +28.0‰). This indicates that sulfur from the diagenetic pyrite was almost entirely recycled, supporting a crucial role of hydrocarbons and bacteria in the formation of the deposit. Further cooling and circulation of the hydrothermal fluid along permeable strata resulted in the observed concentric zoning of sulfides around the normal faults/feeder dikes. We conclude that the Cu-(Fe) sulfides of the ore stage inherited, at least some components from

the pre-ore stage phases (diagenetic pyrite and bitumen) including S, V, Mn, Ni, As, Mo, and Tl, reflecting the important contribution from a marine and sedimentary/basinal source.

2.8. CONCLUDING REMARKS

Geochemical data reported in this study reveal that sulfides from the El Soldado deposit have significant concentrations of trace elements ranging from sub-ppm to wt.% levels. Pyrite is the main host for trace elements, followed by bornite, chalcopyrite and chalcocite, albeit to a lesser extent. The conspicuous presence of Mo, Mn, Tl, and V, Ni and Mo in sulfides suggest a distinctive marine or sedimentary/basinal contribution in the formation of El Soldado, consistent with the presence of organic matter (bitumen) in close association with the main Cu mineralization. Some elements, including Mn, Fe, and S, are likely to have been inherited from the sedimentary source, while others such as Cu, Ag, S, and Cl may have resulted from leaching of the volcanic-volcaniclastic host rocks during the main ore stage. Organic matter appears to have played a key role in the genesis of the deposit, acting as a redox trap and potentially acting as a reductant for metal-chloride complexes and facilitating the precipitation of Cu-(Fe) sulfides (Wilson and Zentilli, 1999). It is clear from our data and previous studies that bitumen contributed some components to the ore system, however, the extent of this contribution remains unconstrained but apparently is variable depending on the volume of hydrocarbons in each given system.

Comparative analysis of sulfide data from El Soldado with similar deposits in Chile and Iran, and with other deposit types including IOCG, IOA, porphyry Cu, and sediment-hosted Cu deposits, highlights distinctive Co/Ni ratios in pyrite that may be indicative of low temperature formation conditions. Although El Soldado and other Chilean stratabound Cu-(Ag) deposits are distinctly differentiated from IOCG–IOA deposits within the same metallogenic belt, the Co/Ni ratios of stratabound deposits overlap with those of porphyry systems. Additionally, sediment-hosted Kupferschiefer Cu deposits fall within the range of Chilean stratabound Cu-(Ag) deposits, emphasizing the contribution of sedimentary sources in this type of deposits. In-Se and Ag-Bi relations in chalcopyrite and bornite, respectively, were tested and compared with different deposit types worldwide. While the In/Se ratio in chalcopyrite might not be related to the temperature of the mineralizing fluids, the Ag/Bi ratio in bornite shows potential for fingerprinting low temperature mineralization. In addition, the Mn/Fe ratio vs. Mo concentration plot for pyrite allows identifying the potential derivation from methane seeps as originally proposed by Smrzka et al. (2024).

The new data presented in this study supports and refines the early genetic model proposed for the El Soldado deposit (Wilson, 1998; Boric, 2002). The evolution of the ore system is characterized by an early stage of burial of the volcano-sedimentary sequence and consequent generation of petroleum at temperatures >60°C. As this burial continued, the previously formed petroleum began to migrate through favorable structures towards the upper member of the Lo Prado Formation. Concurrently, diagenetic framboidal pyrite began to form at a time when oil was still in a liquid state. Continuous burial resulted in petroleum maturation and bitumen formation, thus forming the pre-ore association (stage 2). The ore mineralization was formed by fluids of marine sedimentary and/or basinal origin, which mixed with meteoric water, as they circulate through the

volcano-sedimentary sequence— probably driven by Cretaceous batholith intrusion and regional heat— leaching Cu from the host rocks and leading to the formation of the chalcopyrite-bornite-chalcocite mineralization. This ore assemblage inherited the sedimentary signature of the fluids and of the pre-ore stage assemblage.

Additional research should be undertaken on other stratabound Cu-(Ag) deposits within the Coastal Cordillera of northern-central Chile to improve our understanding of how trace elements are incorporated into sulfide phases such as pyrite, chalcopyrite, bornite and chalcocite. Some of the strategic elements found in this type of ore deposits, such as Cu, Ag, Ni and Co, will play a role in facilitating the green energy transition, while some others may pose potential environmental risks and challenges in mineral processing (As, Sb, Pb). We expect this study will stimulate further investigation into the origin and exploration of stratabound Cu-(Ag) deposits, while also providing valuable data for future studies aimed at assessing their critical mineral potential.

2.9. ACKNOWLEDGMENTS

We extend our gratitude to Dr. Marcos Zentilli for generously providing his sample collection of El Soldado for our study. The authors would also like to thank ANID for providing support through FONDECYT Regular grant #1230161 to MR. The LA-ICP-MS system was funded by the CONICYT-FONDECYT instrumentation project EQM120098, while the µ-XRF instrument was funded by the FONDEQUIP project number EQM200239. We also thank Christian Nievas for his help with SEM analyses, and students at University of Talca for their assistance in the use of the µ-XRF instrument. CA acknowledges funding from ANID scholarship # 22230553. Additionally, a sincere appreciation is extended to the Society of Economic Geologists (SEG) for their generous support to the lead author, through a Graduate Student Fellowship.

2.10. REFERENCES

Aberg, G., Aguirre, L., Levi, B., and Nystrom, J.O., 1984, Spreading-subsidence and generation of ensialic marginal basins: an example from the early Cretaceous of central Chile (B.P. Kokelaar & M.F. Howells, Eds.): Geological Society, London, Special Publications, v. 16, p. 185–193.

Affouri, H., Montacer, M., and Disnar, J.R., 2013, Organic geochemistry of the cenomanian-turonian Bahloul formation petroleum source rock, central and northern Tunisia: Resource Geology, v. 63, p. 262–287.

Aguirre, L., Féraud, G., Morata, D., Vergara, M., and Robinson, D., 1999, Time interval between volcanism and burial metamorphism and rate of basin subsidence in a Cretaceous Andean extensional setting: Tectonophysics, v. 313, p. 433–447.

AngloAmerican, 2022, Ore Reserves and Mineral Resources Report 2021, 54 p.

Auclair, G., Fouquet, Y., and Bohn, M., 1987, Distribution of Selenium in high-temperature hydrothermal sulfide deposits at 13° North, East Pacific Rise: The Canadian Mineralogist, v. 25, p. 577–587.

Bajwah, Z.U., Seccombe, P.K., and Offier, R., 1987, Trace element distribution, Co:Ni ratios and genesis of the Big Cadia iron-copper deposit, New South Wales, Australia: Mineralium Deposita, v. 22, p. 292–300.

Barra, F., Reich, M., Selby, D., Rojas, P., Simon, A., Salazar, E., and Palma, G., 2017, Unraveling the origin of the Andean IOCG clan: A Re-Os isotope approach: Ore Geology Reviews, v. 81, p. 62–78.

Bechtel, A., Elliott, W.C., Wampler, J.M., and Oszczepalski, S., 1999, Clay mineralogy, crystallinity, and K-Ar ages of illites within the Polish Zechstein Basin; implications for the age of Kupferschiefer mineralization: Economic Geology, v. 94, p. 261–272.

Boric, R., 2002, Geology, Mineral Zoning, and Lithochemistry of The El Soldado Manto Type Copper Deposit, Chile. MSc Thesis: Halifax, Canadá, Dalhousic University: 250 p.

Boric, R., and Munizaga, F., 1994, Geocronología Ar/Ar y Rb/Sr del depósito estratoligado de cobre El Soldado (Chile central). Comunicaciones, Universidad de Chile, p. 135–148.

Boric, R., Holmgren, C., Wilson, N., and Zentilli, M., 2002, The Geology Of The Soldado Manto Type Cu (Ag) Deposit, Central Chile: Hydrothermal Iron Oxide Copper-Gold & Related Deposits: A Global Perspective, v. 2, p. 163–184.

Boyce, D., Charrier, R., and Farías, M., 2020, The First Andean Compressive Tectonic Phase: Sedimentologic and Structural Analysis of Mid-Cretaceous Deposits in the Coastal Cordillera, Central Chile (32°50′S): Tectonics, v. 39, p. 1–24.

Bralia, A., Sabatini, G., and Troja, F., 1979, A Revaluation of the Co/Ni Ratio in Pyrite as Geochemical Tool in Ore Genesis: Mineralium Deposita, v. 14, p. 353–374.

Brodbeck, M., McClenaghan, S.H., Kamber, B.S., and Redmond, P.B., 2022, Metal(loid) Deportment in Sulfides from the High-Grade Core of the Bingham Canyon Porphyry Cu-Mo-Au Deposit, Utah: Economic Geology, v. 117, p. 1521–1542.

Butler, I.B., and Nesbitt, R.W., 1999, Trace element distributions in the chalcopyrite wall of a black smoker chimney: insights from laser ablation inductively coupled plasma mass spectrometry (LA-ICP-MS): Earth and Planetary Science Letters, v. 167, p. 335–345.

Calvert, S.E., and Pedersen, T.F., 1993, Geochemistry of Recent oxic and anoxic marine sediments: Implications for the geological record: Marine Geology, v. 113, p. 67–88.

Caraballo, E., Dare, S., and Beaudoin, G., 2022, Variation of trace elements in chalcopyrite from worldwide Ni-Cu sulfide and Reef-type PGE deposits: implications for mineral exploration: Mineralium Deposita, v. 57, p. 1293–1321.

Carrillo-Rosúa, J., Boyce, A.J., Morales-Ruano, S., Morata, D., Roberts, S., Munizaga, F., and Moreno-Rodríguez, V., 2014, Extremely negative and inhomogeneous sulfur isotope signatures in Cretaceous Chilean manto-type Cu-(Ag) deposits, Coastal Range of central Chile: Ore Geology Reviews, v. 56, p. 13–24.

Carvalho, J.R.S., Relvas, J.M.R.S., Pinto, A.M.M., Frenzel, M., Krause, J., Gutzmer, J., Pacheco, N., Fonseca, R., Santos, S., Caetano, P., Reis, T., and Gonçalves, M., 2018, Indium and selenium distribution in the Neves-Corvo deposit, Iberian Pyrite Belt, Portugal: Mineralogical Magazine, v. 82, p. S5–S41.

Chappaz, A., Lyons, T.W., Gregory, D.D., Reinhard, C.T., Gill, B.C., Li, C., and Large, R.R., 2014, Does pyrite act as an important host for molybdenum in modern and ancient euxinic sediments? Geochimica et Cosmochimica Acta, v. 126, p. 112–122.

Charrier, R., and Vicente, J.C., 1970, Liminary and geosyncline Andes: Major orogenic phases and synchronical evolutions of the central and Magellan sectors of the Argentine Chilean Andes, in Solid Earth Problems Conference, Upper Mantle Project, Buenos Aires: p. 451–470.

Charrier, R., Pinto, L., and Rodríguez, M.P., 2007, Tectonostratigraphic evolution of the Andean Orogen in Chile, in Moreno, T. and Gibbons, W. eds., The Geology of Chile: London, The Geological Society, p. 21–114.

Charrier, R., Ramos, V.A., Tapia, F., and Sagripanti, L., 2014, Tectono-stratigraphic evolution of the Andean Orogen between 31 and 37°S (Chile and Western Argentina): Geological Society Special Publication, v. 399, p. 13–61.

Chen, H., Kyser, T.K., and Clark, A.H., 2011, Contrasting fluids and reservoirs in the contiguous Marcona and Mina Justa iron oxide–Cu (–Ag–Au) deposits, south-central Perú: Mineralium Deposita, v. 46, p. 677–706.

Chouinard, A., Paquette, J., and Williams-Jones, A.E., 2005, Crystallographic controls on trace-element incorporation in auriferous pyrite from the Pascua Epithermal High-Sulfidation deposit, Chile-Argentina: The Canadian Mineralogist, v. 43, p. 951–963.

Cioacă, M.E., Munteanu, M., Qi, L., and Costin, G., 2014, Trace element concentrations in porphyry copper deposits from Metaliferi Mountains, Romania: A reconnaissance study: Ore Geology Reviews, v. 63, p. 22–39.

Ciobanu, C.L., Cook, N.J., Utsunomiya, S., Kogagwa, M., Green, L., Gilbert, S., and Wade, B., 2012, Gold-telluride nanoparticles revealed in arsenic-free pyrite: American Mineralogist, v. 97, p. 1515–1518.

Cisternas, M.E., and Hermosilla, J., 2006, The role of bitumen in strata-bound copper deposit formation in the Copiapo area, Northern Chile: Mineralium Deposita, v. 41, p. 339–355.

Coira, B., Davidson, john, Mpodozis, C., and Ramos, V., 1982, Tectonic and Magmatic Evolution of the Andes of Northern Argentina and Chile: Earth-Science Reviews, v. 18, p. 303–332.

Cook, N.J., and Chryssoulis, S.L., 1990, Concentrations of "Invisible Gold" in the common sulfides: Canadian Mineralogist, v. 28, 16 p.

Cook, N.J., Ciobanu, C.L., Danyushevsky, L. V., and Gilbert, S., 2011, Minor and trace elements in bornite and associated Cu-(Fe)-sulfides: A LA-ICP-MS study Bornite mineral chemistry: Geochimica et Cosmochimica Acta, v. 75, p. 6473–6496.

Crespo, J., Reich, M., Barra, F., Verdugo, J.J., Martínez, C., Leisen, M., Romero, R., Morata, D., and Marquardt, C., 2020, Occurrence and distribution of silver in the world-class Río Blanco porphyry Cu-Mo deposit, Central Chile: Economic Geology, v. 115, p. 1619–1644.

Deditius, A.P., and Reich, M., 2016, Constraints on the solid solubility of Hg, Tl, and Cd in arsenian pyrite: American Mineralogist, v. 101, p. 1451–1459.

Deditius, A.P., Utsunomiya, S., Renock, D., Ewing, R.C., Ramana, C. V., Becker, U., and Kesler, S.E., 2008, A proposed new type of arsenian pyrite: Composition, nanostructure and geological significance: Geochimica et Cosmochimica Acta, v. 72, p. 2919–2933.

Deditius, A.P., Utsunomiya, S., Ewing, R.C., and Kesler, S.E., 2009, Nanoscale "liquid" inclusions of As-Fe-S in arsenian pyrite: American Mineralogist, v. 94, p. 391–394.

Deditius, A.P., Utsunomiya, S., Reich, M., Kesler, S.E., Ewing, R.C., Hough, R., and Walshe, J., 2011, Trace metal nanoparticles in pyrite: Ore Geology Reviews, v. 42, p. 32–46.

Deditius, A.P., Reich, M., Kesler, S.E., Utsunomiya, S., Chryssoulis, S.L., Walshe, J., and Ewing, R.C., 2014, The coupled geochemistry of Au and As in pyrite from hydrothermal ore deposits: Geochimica et Cosmochimica Acta, v. 140, p. 644–670.

Dill, H., and Kemper, E., 1990, Crystallographic and chemical variations during pyritization in the upper Barremian and lower Aptian dark claystones from the Lower Saxonian Basin (NW Germany): Sedimentology, v. 37, p. 427–443.

Dubosq, R., Rogowitz, A., Schweinar, K., Gault, B., and Schneider, D.A., 2019, A 2D and 3D nanostructural study of naturally deformed pyrite: assessing the links between trace element mobility and defect structures: Contributions to Mineralogy and Petrology, v. 174, 16 p.

Ehrig, K., Ciobanu, C.L., Verdugo-Ihl, M.R., Dmitrijeva, M., Cook, N.J., and Slattery, A., 2023, Lifting the cloak of invisibility: Gold in pyrite from the Olympic Dam Cu-U-Au-Ag deposit, South Australia: American Mineralogist, v. 108, p. 259–276.

Emerson, S.R., and Huested, S.S., 1991, Ocean anoxia and the concentrations of molybdenum and vanadium in seawater: Marine Chemistry, v. 34, p. 177–196.

Erlandsson, V.B., Wallner, D., Ellmies, R., Raith, J.G., and Melcher, F., 2022, Trace element composition of base metal sulfides from the sediment-hosted Dolostone Ore Formation (DOF) Cu-Co deposit in northwestern Namibia: Implications for ore genesis: Journal of Geochemical Exploration, v. 243, 23 p.

Fleet, M.E., MacLean, P.J., and Barbier, J., 1989, Oscillatory-zoned As-bearing pyrite from stratabound and stratiform gold deposits: an indicator of ore fluid evolution: Economic Geology Monograph, v. 6, p. 356–362.

Foltyn, K., Bertrandsson Erlandsson, V., Zygo, W., Melcher, F., and Pieczonka, J., 2022, New perspective on trace element (Re, Ge, Ag) hosts in the Cu-Ag Kupferschiefer deposit, Poland: Insight from a LA-ICP-MS trace element study: Ore Geology Reviews, v. 143, 23 p.

Fontboté, L., 1990, Stratabound Ore Deposits in the Andes: A Review and a Classification According to Their Geotectonic Setting. In: Fontboté, L., Amstutz, G.C., Cardozo, M., Cedillo, E., Frutos, J. (eds) Stratabound Ore Deposits in the Andes. Special Publication No. 8 of the Society for Geology Applied to Mineral Deposits, vol 8. Springer, Berlin, Heidelberg, 812 p.

Fougerouse, D., Reddy, S.M., Aylmore, M., Yang, L., Guagliardo, P., Saxey, D.W., Rickard, W.D.A., and Timms, N., 2021, A new kind of invisible gold in pyrite hosted in deformation-related dislocations: Geology, v. 49, p. 1225–1229.

Frenzel, M., Hirsch, T., and Gutzmer, J., 2016, Gallium, germanium, indium, and other trace and minor elements in sphalerite as a function of deposit type - A meta-analysis: Ore Geology Reviews, v. 76, p. 52–78.

Fuchs, S., Williams-Jones, A.E., and Przybylowicz, W.J., 2016, The origin of the gold and uranium ores of the Black Reef Formation, Transvaal supergroup, South Africa: Ore Geology Reviews, v. 72, p. 149–164.

Fuentes, F., Feraud, B., Aguirre, L., and Morata, D., 2005, Ar-40/Ar-39 dating ofvolcanism and subsequent very low-grade metamorphism in a subsiding basin: Example of the Cretaceous lava series from central Chile: Chemical Geology, v. 214, p. 157–177.

Gaupp, R., Möller, P., Lüders, V., Di Primio, R., Littke, R., Urai, J.L., Nover, G., Zwach, C., Ondrak, R., Schöner, R., Krooss, B.M., Cramer, B., Plessen, B., and Machel, H.G., 2008, Fluid in sedimentary basins: An overview, in Dynamics of Complex Intracontinental Basins: The Central European Basin System: Springer Berlin Heidelberg, p. 346–458.

George, L.L., Cook, N.J., and Ciobanu, C.L., 2016, Partitioning of trace elements in co-crystallized sphalerite-galena-chalcopyrite hydrothermal ores: Ore Geology Reviews, v. 77, p. 97–116.

George, L.L., Cook, N.J., Crowe, B.B.P., and Ciobanu, C.L., 2018, Trace elements in hydrothermal chalcopyrite: Mineralogical Magazine, v. 82, p. 59–88.

George, L.L., Biagioni, C., Lepore, G.O., Lacalamita, M., Agrosì, G., Capitani, G.C., Bonaccorsi, E., and d'Acapito, F., 2019, The speciation of thallium in (Tl,Sb,As)-rich pyrite: Ore Geology Reviews, v. 107, p. 364–380.

Gregory, D.D., Large, R.R., Halpin, J.A., Baturina, E.L., Lyons, T.W., Wu, S., Danyushevsky, L., Sack, P.J., Chappaz, A., Maslennikov, V. V, and Bull, S.W., 2015, Trace Element Content of Sedimentary Pyrite in Black Shales: Economic Geology, v. 110, p. 1389–1410.

Gregory, D.D., Cracknell, M.J., Large, R.R., McGoldrick, P., Kuhn, S., Maslennikov, V. V., Baker, M.J., Fox, N., Belousov, I., Figueroa, M.C., Steadman, J.A., Fabris, A.J., and Lyons, T.W., 2019, Distinguishing ore deposit type and barren sedimentary pyrite using laser ablation-inductively coupled plasma-mass spectrometry trace element data and statistical analysis of large data sets: Economic Geology, v. 114, p. 771–786.

Gustafson, L., and Hunt, J., 1975, The porphyry copper deposit at El Salvador, Chile: Economic Geology, v. 70, p. 857–912.

Helz, G.R., Miller, C.V., Charnock, J.M., Mosselmans, J.F.W., Pattrick, R.A.D., Garner, C.D., and Vaughan, D.J., 1996, Mechanism of molybdenum removal from the sea and its concentration in black shales: EXAFS evidence: Geochimica et Cosmochimica Acta, v. 60, p. 3631–3642.

Helz, G.R., Bura-Nakić, E., Mikac, N., and Ciglenečki, I., 2011, New model for molybdenum behavior in euxinic waters: Chemical Geology, v. 284, p. 323–332.

Herazo, A., Reich, M., Barra, F., Morata, D., del Real, I., and Pagès, A., 2020, Assessing the role of bitumen in the formation of stratabound Cu-(Ag) deposits: Insights from the Lorena deposit, Las Luces district, northern Chile: Ore Geology Reviews, v. 124, 21 p.

Herazo, A., Reich, M., Barra, F., Morata, D., and Del Real, I., 2021, Trace Element Geochemistry of Pyrite from Bitumen-Bearing Stratabound Cu-(Ag) Deposits, Northern Chile: ACS Earth and Space Chemistry, v. 5, p. 566–579.

Hochella, M.F., Lower, S.K., Maurice, P.A., Penn, R.L., Sahai, N., Sparks, D.L., and Twining, B.S., 2008, Nanominerals, Mineral Nanoparticles, and Earth Systems: Science, v. 319, p. 1631–1635.

Hohf, M., Trumbull, R.B., Cuadra, P., and Solé, M., 2023, Tourmaline Breccias from the Río Blanco-Los Bronces Porphyry Copper District, Chile: Constraints on the Fluid Source and the Utility of Tourmaline Composition for Exploration: Economic Geology, v. 118, p. 779–800.

Holmgren, C., 1987, Antecedentes para un modelo genético del yacimiento El Soldado, V Región de Valparaíso: Revista Geológica de Chile, v. 14, p. 3–18.

Huerta-Diaz, M.A., and Morse, J.W., 1992, Pyritization of trace metals in anoxic marine sediments: Geochimica et Cosmochimica Acta, v. 56, p. 2681–2702.

Huston, D.L., Sie, S.H., Suter, G.F., Cooke, D.R., Both, R.A., Huston, D.L., Sie, S.H., and Suter, G.F., 1995, Trace Elements in Sulfide Minerals from Eastern Australian Volcanic-Hosted Massive Sulfide Deposits: Part I. Proton Microprobe Analyses of Pyrite, Chalcopyrite, and Sphalerite, and Part II. Selenium Levels in Pyrite: Comparison with (5348 Values and Implications for the Source of Sulfur in Volcanogenic Hydrothermal Systems Part I. Proton Microprobe Analyses of Pyrite, Chalcopyrite, and Sphalerite Introduction and Previous Studies: Economic Geology, v. 90, p. 1167–1196.

Ikramuddin, M., Besse, L., and Nordstrom, M., 1986, Thallium in the Carlin-type gold deposits: Applied Geochemistry, v. 1, p. 493–502.

Jacobs, L., Emerson, S., and Skei, J., 1985, Partitioning and transport of metals across the O2/H2S interface in a permanently anoxic basin: Framvaren Fjord, Norway: Geochimica et Cosmochimica Acta, v. 49, p. 1433–1444.

Jara, J.J., Barra, F., Reich, M., Morata, D., Leisen, M., and Romero, R., 2021a, Geochronology and petrogenesis of intrusive rocks in the Coastal Cordillera of northern Chile: Insights from zircon U-Pb dating and trace element geochemistry: Gondwana Research, v. 93, p. 48–72.

Jara, J.J., Barra, F., Reich, M., Leisen, M., Romero, R., and Morata, D., 2021b, Episodic construction of the early Andean Cordillera unravelled by zircon petrochronology: Nature Communications, v. 12, p. 1–8.

Jochum, K.P., Willbold, M., Raczek, I., Stoll, B., and Herwig, K., 2005, Chemical characterisation of the USGS reference glasses GSA-1G, GSC-1G, GSD-1G, GSE-1G, BCR-2G, BHVO-2G and BIR-1G using EPMA, ID-TIMS, ID-ICP-MS and LA-ICP-MS: Geostandards and Geoanalytical Research, v. 29, p. 285–302.

Kelepile, T., Bineli Betsi, T., Franchi, F., and Shemang, E., 2020, Partitioning and distribution of silver in sediment-hosted Cu-Ag deposits: Evidence from the Ghanzi-Chobe Belt portion of the Kalahari Copper Belt: Ore Geology Reviews, v. 124, 23 p.

Kieft, K., and Damman, A.H., 1990, Indium-bearing chalcopyrite and sphalerite from the Gasborn area, West Bergslagen, central Sweden: Mineralogical Magazine, v. 54, p. 109–112.

King, E.K., Perakis, S.S., and Pett-Ridge, J.C., 2018, Molybdenum isotope fractionation during adsorption to organic matter: Geochimica et Cosmochimica Acta, v. 222, p. 584–598.

Klohn, E., Holmgren, C., and Ruge, H., 1990, El Soldado, a Stratabound Copper Deposit Associated with Alkaline Volcanism in the Central Chilean Coastal Range, in Fontboté, G., Amstutz, G.C., Cardozo, M., Cedillo, E., and Frutos, J. eds., Stratabound ore deposits in the Andes: Special Publication of the Society for Geology Applied to Mineral Deposits, p. 435–448.

Knipping, J.L., Bilenker, L.D., Simon, A.C., Reich, M., Barra, F., Deditius, A.P., Lundstrom, C., Bindeman, I., and Munizaga, R., 2015, Giant Kiruna-type deposits form by efficient flotation of magmatic magnetite suspensions: Geological Society of America, v. 43, p. 591–594.

Kojima, S., Astudillo, J., Rojo, J., Tristá, D., and Hayashi, K.I., 2003, Ore mineralogy, fluid inclusion, and stable isotopic characteristics of stratiform copper deposits in the coastal Cordillera of northern Chile: Mineralium Deposita, v. 38, p. 208–216.

Kojima, S., Trista-Aguilera, D., and Hayashi, K.I., 2009, Genetic Aspects of the Manto-Type Copper Deposits Based on Geochemical Studies of North Chilean Deposits: Resource Geology, v. 59, p. 87–98.

Large, R., Maslennikov, V., Robert, F., Danyushevsky, L., and Chang, Z., 2007, Multistage Sedimentary and Metamorphic Origin of Pyrite and Gold in the Giant Sukhoi Log Deposit, Lena Gold Province, Russia: Economic Geology, v. 102, p. 1233–1267.

Large, R., Danyushevsky, L., Hollit, C., Maslennikov, V., Meffre, S., Gilbert, S., Bull, S., Scott, R., Emsbo, P., Thomas, H., Singh, B., and Foster, J., 2009, Gold and Trace Element Zonation in

Pyrite Using a Laser Imaging Technique: Implications for the Timing of Gold in Orogenic and Carlin-Style Sediment-Hosted Deposits: Economic Geology, v. 104, p. 635–668.

Large, R., Bull, S., and Maslennikov, V., 2011, A carbonaceous sedimentary source-rock model for Carlin-type and orogenic gold deposits: Economic Geology, v. 106, p. 331–358.

Large, R.R., Halpin, J.A., Danyushevsky, L. V., Maslennikov, V. V., Bull, S.W., Long, J.A., Gregory, D.D., Lounejeva, E., Lyons, T.W., Sack, P.J., McGoldrick, P.J., and Calver, C.R., 2014, Trace element content of sedimentary pyrite as a new proxy for deep-time ocean-atmosphere evolution: Earth and Planetary Science Letters, v. 389, p. 209–220.

Larson, R.L., 1991, Geological consequences of superplumes: Geology, v. 19, p. 963–966.

Larson, R.L., and Kincaid, C., 1996, Onset of mid-Cretaceous volcanism by elevation of the 670 km thermal boundary layer: Geology, v. 24, p. 551–554.

Li, R., Chen, H., Xia, X., Yang, Q., Li, L., Xu, J., Huang, C., and Danyushevsky, L. V., 2017, Ore fluid evolution in the giant Marcona Fe-(Cu) deposit, Perú: Evidence from in-situ sulfur isotope and trace element geochemistry of sulfides: Ore Geology Reviews, v. 86, p. 624–638.

Li, R., Chen, H., Xia, X., Yang, Q., Danyushevsky, L. V., and Lai, C., 2018, Using integrated in-situ sulfide trace element geochemistry and sulfur isotopes to trace ore-forming fluids: Example from the Mina Justa IOCG deposit (southern Perú): Ore Geology Reviews, v. 101, p. 165–179.

Loftus-Hills, G., and Solomon, M., 1967, Cobalt, Nickel and Selenium in Sulphides as Indicators of Ore Genesis: Mineralium Deposita, v. 2, p. 228–242.

Longerich, H.P., Jackson, S.E., and Günther, D., 1996, Laser ablation inductively coupled plasma mass spectrometric transient signal data acquisition and analyte concentration calculation: Journal of Analytical Atomic Spectrometry, v. 11, p. 899–904.

Maghfouri, S., Rastad, E., Borg, G., Hosseinzadeh, M.R., Movahednia, M., Mahdavi, A., and Mousivand, F., 2020, Metallogeny and temporal–spatial distribution of sediment-hosted stratabound copper (SSC-type) deposits in Iran; implications for future exploration: Ore Geology Reviews, v. 127, 30 p.

Maksaev, V., and Zentilli, M., 2002, Chilean Strata-Bound Cu-(Ag) Deposit: Overview: In Porter, T.M. (Ed.), Hydrothermal Iron Oxide Copper-Gold & Related Deposits: A Global Perspective, v. 2, PGC Publishing, Adelaide, p. 185–205.

Maksaev, V., Townley, B., Palacios, C., and Camus, F., 2007, Metallic Ore Deposits, in Moreno, T. and Gibbons, W. eds., The Geology of Chile: London, The Geological Society of London, p. 177–199.

Mansur, E.T., Dare, S.A.S., Filho, C.F.F., Miranda, A.C.R., and Monteiro, L.V.S., 2023, The distribution of trace elements in sulfides and magnetite from the Jaguar hydrothermal nickel deposit: Exploring the link with IOA and IOCG deposits within the Carajás Mineral Province, Brazil: Ore Geology Reviews, v. 152, 27 p.

Maureira, I., Barra, F., Reich, M and Palma, G., 2023, Geology of the Altamira and Las Luces deposits, Coastal Cordillera, northern Chile: implications for the origin of stratabound Cu–(Ag) deposits. Mineralium Deposita, v. 58, p. 379–402.

Mederski, S., Pršek, J., Majzlan, J., Kiefer, S., Dimitrova, D., Milovský, R., Koch, C.B., and Kozień, D., 2022, Geochemistry and textural evolution of As-Tl-Sb-Hg-rich pyrite from a sediment-hosted As-Sb-Tl-Pb ± Hg ± Au mineralization in Janjevo, Kosovo: Ore Geology Reviews, v. 151, 26 p.

Migdisov, A.A., Guo, X., Xu, H., Williams-Jones, A.E., Sun, C.J., Vasyukova, O., Sugiyama, I., Fuchs, S., Pearce, K., and Roback, R., 2017, Hydrocarbons as ore fluids: Geochemical Perspectives Letters, v. 5, p. 47–52.

Mills, R.A., Thomson, J., Elderfield, H., Hinton, R.W., and Hyslop, E., 1994, Uranium enrichment in metalliferous sediments from the Mid-Atlantic Ridge: Earth and Planetary Science Letters, v. 124, p. 35–47.

Morata, D., Féraud, G., Schärer, U., Aguirre, L., and Belmar, L., 2006, A new geochronological framework for Lower Cretaceous magmatism in the Coastal Range of central Chile: XI Congreso Geológico Chileno, Antofagasta, Chile, August 7–11, 2006, Proceedings, p. 509–512.

Movahednia, M., Maghfouri, S., Fazli, N., Rastad, E., Ghaderi, M., and González, F.J., 2022, Metallogeny of Manto-type stratabound Cu-(Ag) mineralization in Iran: Relationship with Neo-Tethyan evolution and implications for future exploration: Ore Geology Reviews, v. 149, 28 p.

Mpodozis, C., and Allmendinger, R.W., 1993, Extensional tectonics, Cretaceous Andes, northern Chile (27°S): Geological Society of America Bulletin, v. 105, p. 1462–1477.

Mpodozis, C., and Kay, S., 1990, Provincias magmáticas ácidas y evolución tectónica de Gondwana: Andes chilenos (28-31°S): Revista Geológica de Chile, v. 17, p. 153–180.

Mpodozis, C., and Ramos, V., 1989, The Andes of Chile and Argentina, in Ericksen, G.E., Cañas-Pinochet, M.T., and Reinemund, J.A. eds., Geology of the Andes and its relation to hydrocarbon

and mineral resources: Texas, Circumpacific Council for Energy and Mineral Resources: Earth Science Series, p. 59–90.

Mukherjee, I., and Large, R., 2017, Application of pyrite trace element chemistry to exploration for SEDEX style Zn-Pb deposits: McArthur Basin, Northern Territory, Australia: Ore Geology Reviews, v. 81, p. 1249–1270.

Nasi, C., and Thiele, R., 1982, Estratigrafía del Jurásico y Cretácico de la Cordillera de la Costa, al sur del Río Maipo, entre Melipilla y Laguna de Aculeo (Chile central). Revista Geológica de Chile, v. 16, p. 81–99.

Ojeda, A., Barra, F., Reich, M., Romero, R., and Tapia, M.J., 2024, Evolution and fertility of magmas associated with iron oxide-apatite (IOA) deposits, Coastal Cordillera, Northern Chile: A zircon petrochronology perspective: Gondwana Research, v. 131, p. 38–56.

Oliveros, V., Féraud, G., Aguirre, L., Ramírez, L., Fornari, M., Palacios, C., and Parada, M., 2008, Detailed 40 Ar/ 39 Ar dating of geologic events associated with the Mantos Blancos copper deposit, northern Chile: Mineralium Deposita, v. 43, p. 281–293.

Oliveros, V., Vásquez, P., Creixell, C., Lucassen, F., Ducea, M.N., Ciocca, I., González, J., Espinoza, M., Salazar, E., Coloma, F., and Kasemann, S.A., 2020, Lithospheric evolution of the Pre- and Early Andean convergent margin, Chile: Gondwana Research, v. 80, p. 202–227.

Oszczepalski, S., 1999, Origin of the Kupferschiefer polymetallic mineralization in Poland: Mineralium Deposita, v. 34, p. 599–613.

Parnell, J., Kucha, H., and Landais, P., 1993, Bitumens in Ore Deposits: Springer Berlin Heidelberg.

Perona, J., Canals, À., and Cardellach, E., 2018, Zn-Pb mineralization associated with salt diapirs in the basque-cantabrian Basin, Northern Spain: Geology, geochemistry, and genetic model: Economic Geology, v. 113, p. 1133–1159.

Piraces, R., and Maksaev, V., 1977, Geología de la Hoja Quillota: Instituto de Investigaciones Geológicas, Chile, no. 1 map scale 1:250.000, 64 p.

Qian, Z., Xinzhi, Z., Jiayong, P., and Shuxun, S., 1998, Geochemical Enrichment and Mineralization of Indium: Chinese Journal of Geochemistry, v. 17, p. 221–225.

Ramos, V., and Aleman, A., 2000, Tectonic evolution of the Andes. In: Cordani, U.G. et al (editors): Tectonic Evolution of South America, p. 635–685.

del Real, I., Thompson, J.F.H., Simon, A.C., and Reich, M., 2020, Geochemical and isotopic signature of pyrite as a proxy for fluid source and evolution in the Candelaria-Punta del Cobre iron oxide copper-gold District, Chile: Economic Geology, v. 115, p. 1493–1517.

Reich, M., Kesler, S.E., Utsunomiya, S., Palenik, C.S., Chryssoulis, S.L., and Ewing, R.C., 2005, Solubility of gold in arsenian pyrite: Geochimica et Cosmochimica Acta, v. 69, p. 2781–2796.

Reich, M., Utsunomiya, S., Kesler, S.E., Wang, L., Ewing, R.C., and Becker, U., 2006, Thermal behavior of metal nanoparticles in geologic materials: Geology, v. 34, p. 1033–1036.

Reich, M., Palacios, C., Barra, F., and Chryssoulis, S., 2013, "Invisible" silver in chalcopyrite and bornite from the Mantos Blancos Cu deposit, northern Chile: European Journal of Mineralogy, v. 25, p. 453–460.

Reich, M., Simon, A.C., Deditius, A., Barra, F., Chryssoulis, S., Lagas, G., Tardani, D., Knipping, J., Bilenker, L., Sánchez-Alfaro, P., Roberts, M.P., and Munizaga, R., 2016, Trace element signature of pyrite from the Los Colorados Iron Oxide-Apatite (IOA) deposit, Chile: A missing link between Andean IOA and Iron Oxide Copper-Gold Systems?: Economic Geology, v. 111, p. 743–761.

Reich, M., Simon, A.C., Barra, F., Palma, G., Hou, T., and Bilenker, L.D., 2022, Formation of iron oxide–apatite deposits: Nature Reviews Earth and Environment, v. 3, p. 758–775.

Reutter, K.J., 2001, Le Ande centrali: elemento di un'orogenesi di margine continentale attivo: Acta Naturalia de l'Ateneo Parmense, v. 37, p. 5–37.

Rieger, A., Schwark, L., Cisternas, M.-E., and Miller, H., 2008, Genesis and Evolution of Bitumen in Lower Cretaceous Lavas and Implications for Strata-bound Copper Deposits, North Chile: Economic Geology, v. 103, p. 387–404.

Rivano, S., 1993, Hoja Quillota y Portillo 1:250.000. Servicio Nacional de Geología y Minería: Carta Geológica de Chile, no. 73, 202 p.

Rivas-Romero, C., Reich, M., Barra, F., Gregory, D., and Pichott, S., 2021, The relation between trace element composition of Cu-(Fe) sulfides and hydrothermal alteration in a porphyry copper deposit: Insights from the Chuquicamata underground mine, Chile: Minerals, v. 11, 29 p.

Rojas, P.A., Barra, F., Deditius, A., Reich, M., Simon, A., Roberts, M., and Rojo, M., 2018, New contributions to the understanding of Kiruna-type iron oxide-apatite deposits revealed by magnetite ore and gangue mineral geochemistry at the El Romeral deposit, Chile: Ore Geology Reviews, v. 93, p. 413–435.

Román, N., Reich, M., Leisen, M., Morata, D., Barra, F., and Deditius, A.P., 2019, Geochemical and micro-textural fingerprints of boiling in pyrite: Geochimica et Cosmochimica Acta, v. 246, p. 60–85.

Ruiz, C., Aguirre, L., Corvalan, J., Klohn, C., and Klohn, E., 1965, Geología y yacimientos metalíferos de Chile: Instituto de Investigaciones Geológicas, Santiago, Chile. 302 p.

Ruiz, J., Freydier, C., McCandless, T., Chesley, J., and Munizaga, F., 1997, Re-Os isotope systematics of sulfides from base-metal porphyry and manto-type mineralization in Chile: International Geology Review, v. 39, p. 317–324.

Sadati, S.N., Yazdi, M., Mao, J., Behzadi, M., Adabi, M.H., Lingang, X., Zhenyu, C., and Mokhtari, M.A.A., 2016, Sulfide mineral chemistry investigation of sediment-hosted stratiform copper deposits, Nahand-Ivand area, NW Iran: Ore Geology Reviews, v. 72, p. 760–776.

Saintilan, N.J., Spangenberg, J.E., Chiaradia, M., Chelle-Michou, C., Stephens, M.B., and Fontboté, L., 2019, Petroleum as source and carrier of metals in epigenetic sediment-hosted mineralization: Scientific Reports, v. 9, 7 p.

Saric, N., Kreft, C., and Huete, C., 2003, Geología del yacimiento Lo Aguirre, Chile: Revista Geológica de Chile, v. 30, p. 317–331.

Sato, T., 1984, Manto type copper deposits in Chile: a review: Bulletin of the Geological Survey of Japan, v. 35, p. 565–582.

Schirmer, T., Koschinsky, A., and Bau, M., 2014, The ratio of tellurium and selenium in geological material as a possible paleo-redox proxy: Chemical Geology, v. 376, p. 44–51.

Scholz, F., McManus, J., and Sommer, S., 2013, The manganese and iron shuttle in a modern euxinic basin and implications for molybdenum cycling at euxinic ocean margins: Chemical Geology, v. 355, p. 56–68.

Schwarz-Schampera, U., and Herzig, P.M., 2002, Indium: Geology, Mineralogy and Economics: Berlin, Heidelberg, Springer Berlin Heidelberg, 262 p.

Scott, R., Meffre, S., Woodhead, J., Gilbert, S., Berry, R., and Emsbo, P., 2009, Development of Framboidal Pyrite During Diagenesis, Low-Grade Regional Metamorphism, and Hydrothermal Alteration: Economic Geology, v. 104, p. 1143–1168.

Sellés, D., and Gana, P., 2001, Geología del área Talagante-San Francisco de Mostazal: regiones Metropolitana de Santiago y del Libertador General Bernardo O'Higgins, Gobierno de Chile,

Servicio Nacional de Geología y Minería. Serie Geología Básica no. 74, 1 mapa escala 1:100.000, 1 anexo, Santiago, 30 p.

Seward, T.M., Henderson, C.M.B., and Charnock, J.M., 2000, Indium III chloride complexing and solvation in hydrothermal solutions to 350°C: an EXAFS study: Chemical Geology, v. 167, p. 117–127.

Shannon, R., 1976, Revised effective ionic radii and systematic studies of interatomic distances in halides and chalcogenides: Acta Crystallographica Section A, v. 32, p. 751–767.

Shikazono, N., Nakata, M., and Tokuyama, E., 1994, Pyrite with high Mn content from the Nankai Trough formed from subduction-induced cold seepage: Marine Geology, v. 118, p. 303–313.

Siebert, C., Pett-Ridge, J.C., Opfergelt, S., Guicharnaud, R.A., Halliday, A.N., and Burton, K.W., 2015, Molybdenum isotope fractionation in soils: Influence of redox conditions, organic matter, and atmospheric inputs: Geochimica et Cosmochimica Acta, v. 162, p. 1–24.

Sillitoe, R.H., 1992, Gold and copper Metallogeny of the central Andes: Past, present and future exploration objectives: Economic Geology, v. 87, p. 2205–2216.

Sillitoe, R.H., 2003, Iron oxide-copper-gold deposits: An Andean view: Mineralium Deposita, v. 38, p. 787–812.

Sillitoe, R.H., 2010, Porphyry Copper Systems: Economic Geology, v. 105, p. 3–41.

Smrzka, D., Lin, Z., Monien, P., Chen, T., Bach, W., Peckmann, J., and Bohrmann, G., 2024, Pyrite-based trace element fingerprints for methane and oil seepage: Geochemical Perspectives Letters, v. 29, p. 33–37.

Spirakis, C.S., and Heyll, A. V, 1993, Organic Matter (Bitumen and Other Forms) as the Key to Localisation of Mississippi Valley-Type Ores: Special Publication of the Society for Geology Applied to Mineral Deposits, v. 9, p. 381–398.

Steinmann, G., 1929, Geologie von Peru: Kart Winter, Heidelberg, p. 409–432.

Tardani, D., Reich, M., Deditius, A.P., Chryssoulis, S., Sánchez-Alfaro, P., Wrage, J., and Roberts, M.P., 2017, Copper–arsenic decoupling in an active geothermal system: A link between pyrite and fluid composition: Geochimica et Cosmochimica Acta, v. 204, p. 179–204.

Tatsumi, Y., Shinjoe, H., Ishizuka H, Sager, W.W., and Klaus, A., 1998, Geochemical evidence for a mid-Cretaceous superplume: Geology, v. 26, p. 151–154.

Thomas, H., 1958, Geología de la Cordillera de la Costa entre el Valle de La Ligua y la Cuesta de Barriga: Instituto de Investigaciones Geológicas, Boletín no. 2, p. 1–80.

Utsunomiya, A., Ota, T., Windley, B., Suzuki, N., Uchio, Y., Munekata, K and Maruyama, S., 2007, History of the Pacific Superplume: Implications for Pacific Paleogeography Since the Late Proterozoic. In: Yuen, D.A., Maruyama, S., Karato, SI., Windley, B.F. (eds) Superplumes: Beyond Plate Tectonics. Springer, Dordrecht, p. 262–408.

Vasyukova, O. V., and Williams-Jones, A.E., 2022, Constraints on the Genesis of Cobalt Deposits: Part II. Applications to Natural Systems: Economic Geology, v. 117, p. 529–544.

Verberne, R., Reddy, S.M., Saxey, D.W., Fougerouse, D., Rickard, W.D.A., Quadir, Z., Evans, N.J., and Clark, C., 2022, Dislocations in minerals: Fast-diffusion pathways or trace-element traps?: Earth and Planetary Science Letters, v. 584, 10 p.

Vergara, M., Levi, B., Nyström, J. o, and Cancino, A., 1995, Jurassic and Early Cretaceous Island arc volcanism, extension, and subsidence in the Coast Range of central Chile: Geological Society of American Bulletin, v. 107, p. 1427–1440.

Wall, R., Sellés, D., and P, G., 1999, Área Tiltil-Santiago, Región Metropolitana, Mapas Geológicos, N°11, 1 mapa escala 1:100.000: Santiago, Servicio Nacional de Geología y Minería, 1 p.

Williams-Jones, A.E., and Vasyukova, O. V., 2022, Constraints on the Genesis of Cobalt Deposits: Part I. Theoretical Considerations: Economic Geology, v. 117, no. 3, p. 513–528.

Wilson, N., 1998, The role of petroleum in the formation of The El Soldado copper deposit, Chile: Hydrothermal replacement of a biodegrades petroleum reservoir. Ph. D Thesis: Halifax, Canada, Dalhousie University, 418 p.

Wilson, N., and Zentilli, M., 1999, The Role of Organic Matter in the Genesis of the El Soldado Volcanic-Hosted Manto-Type Cu Deposit, Chile: Economic Geology, v. 94, p. 1115–1136.

Wilson, N., Zentilli, M., and Spiro, B., 2003a, A sulfur, carbon, oxygen, and strontium isotope study of the volcanic-hosted El Soldado Manto-Type copper deposit, Chile: The essential role of bacteria and petroleum: Economic Geology, v. 98, p. 163–174.

Wilson, N., Zentilli, M., Reynolds, P.H., and Boric, R., 2003b, Age of mineralization by basinal fluids at the El Soldado manto-type copper deposit, Chile: 40Ar/39Ar geochronology of K-feldspar: Chemical Geology, v. 197, p. 161–176.

Wilson, N.S.F., and Zentilli, M., 2006, Association of pyrobitumen with copper mineralization from the Uchumi and Talcuna districts, central Chile: International Journal of Coal Geology, v. 65, p. 158–169.

Wilson, S.A., Ridley, W.I., and Koenig, A.E., 2002, Development of sulfide calibration standards for the laser ablation inductively-coupled plasma mass spectrometry technique: Journal of Analytical Atomic Spectrometry, v. 17, p. 406–409.

Wohlgemuth-Ueberwasser, C.C., Viljoen, F., Petersen, S., and Vorster, C., 2015, Distribution and solubility limits of trace elements in hydrothermal black smoker sulfides: An in-situ LA-ICP-MS study: Geochimica et Cosmochimica Acta, v. 159, p. 16–41.

Wood, S.A., and Samson, I.M., 2006, The aqueous geochemistry of gallium, germanium, indium and scandium: Ore Geology Reviews, v. 28, p. 57–102.

Yamamoto, M., 1976, Relationship between Se/S and Sulfur Isotope Ratios of Hydrothermal Sulfide Minerals: Mineralium Deposita, v. 11, p. 197–209.

Yu, J., Morrissey, L.J., Hand, M., Payne, J.L., and Chen, Y.-J., 2024, The Fe-Cu disconnect: unraveling a composite iron oxide copper-gold deposit in the Olympic Fe-Cu-Au province, Gawler Craton: Economic Geology, v. 119, p. 189–199.

Zelenski, M., Garavelli, A., Pinto, D., Vurro, F., Moëlo, Y., Bindi, L., Makovicky, E., and Bonaccorsi, E., 2009, Tazieffite, Pb20Cd2(As,Bi)22S50CI10, a new chloro-sulfosalt from Mutnovsky volcano, Kamchatka Peninsula, Russian Federation: American Mineralogist, v. 94, p. 1312–1324.

Zentilli, M., Munizaga, F., Graves, M.C., Boric, R., Wilson, N.S.F., Mukhopadhyay, P.K., and Snowdon, L.R., 1997, Hydrocarbon Involvement in the Genesis of Ore Deposits: An Example in Cretaceous Stratabound (Manto-Type) Copper Deposits of Central Chile: International Geology Review, v. 39, p. 1–21.

2.11. FIGURES

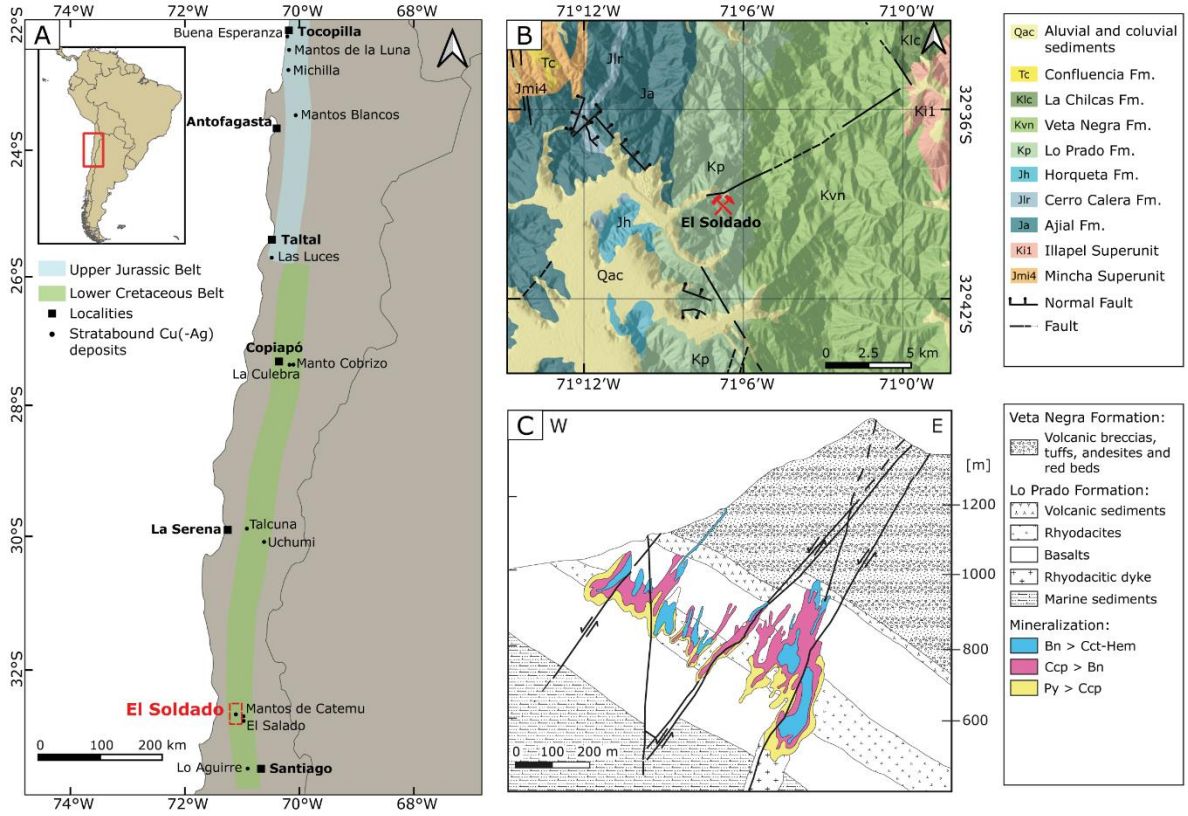

Figura 6. *(A) Location map of the Lower Cretaceous and Upper Jurassic stratabound Cu-(Ag) deposits along the Coastal Cordillera of central-northern Chile (modified from Herazo et al., 2020) (B) Geological map of the El Soldado district, showing the location of the deposit (modified from Rivano, 1996) (C) East-west cross section of the El Soldado deposit at coordinate N-750 (modified from Boric, 2002). Host formations are shown, as well as structures and mineralized ore bodies and sulfide zonation. Bn: bornite; Cct: chalcocite; Hem: hematite; Ccp: chalcopyrite; Py: pyrite.*

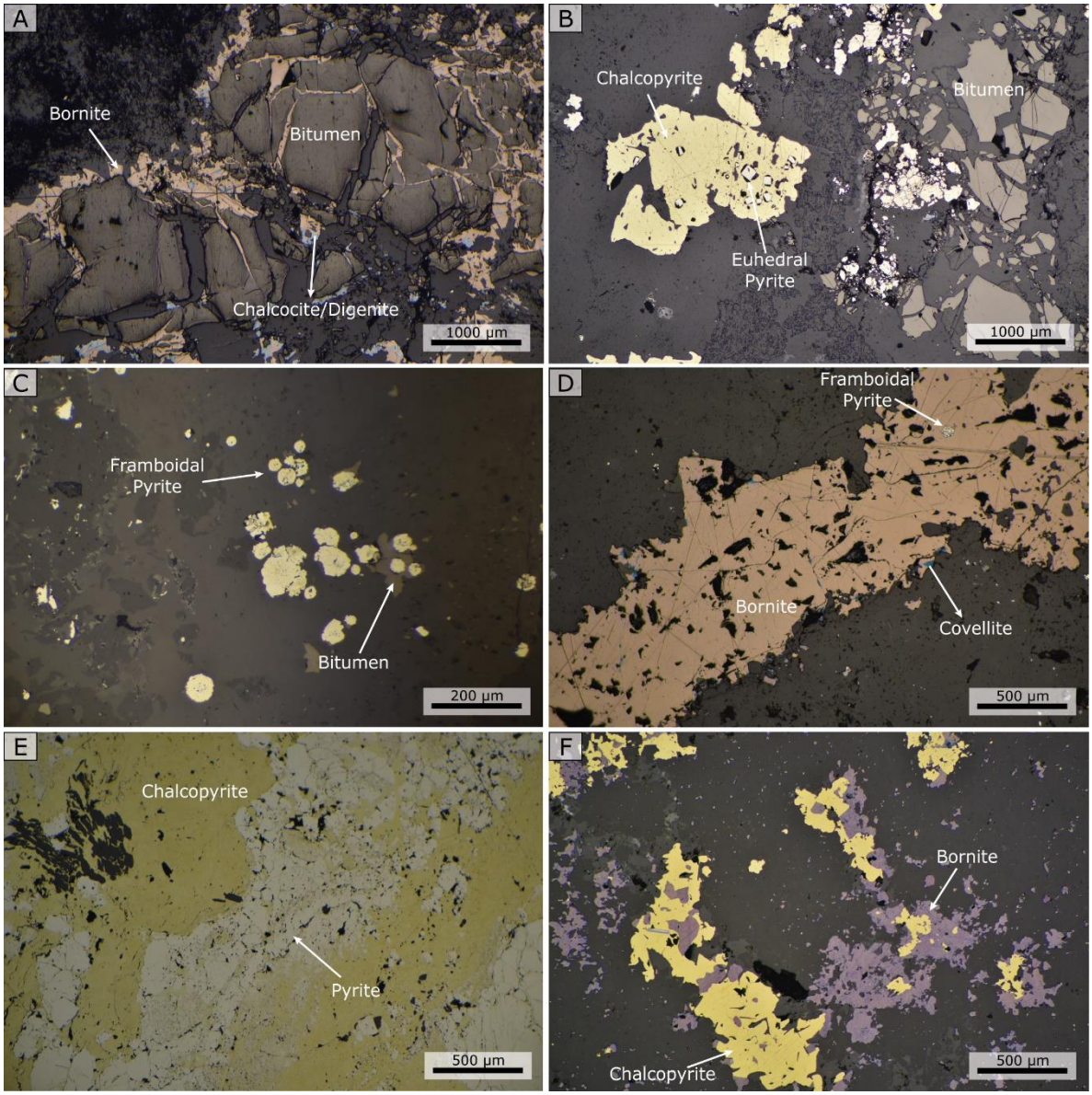

Figura 7. *Reflected light photomicrographs of representative Cu-(Fe) sulfide assemblages from the El Soldado deposit. (A) Bitumen fractures filled with bornite. (B) Chalcopyrite grains surrounding euhedral pyrite grains, together with fractured bitumen grains. (C) Framboidal pyrite in close association with bitumen. (D) Framboidal pyrite completely surrounded by bornite. Also observed is scarce covellite replacing bornite along rims and fractures. (E) Abundant chalcopyrite surrounding and replacing pyrite. (F) Chalcopyrite replaced by bornite.*

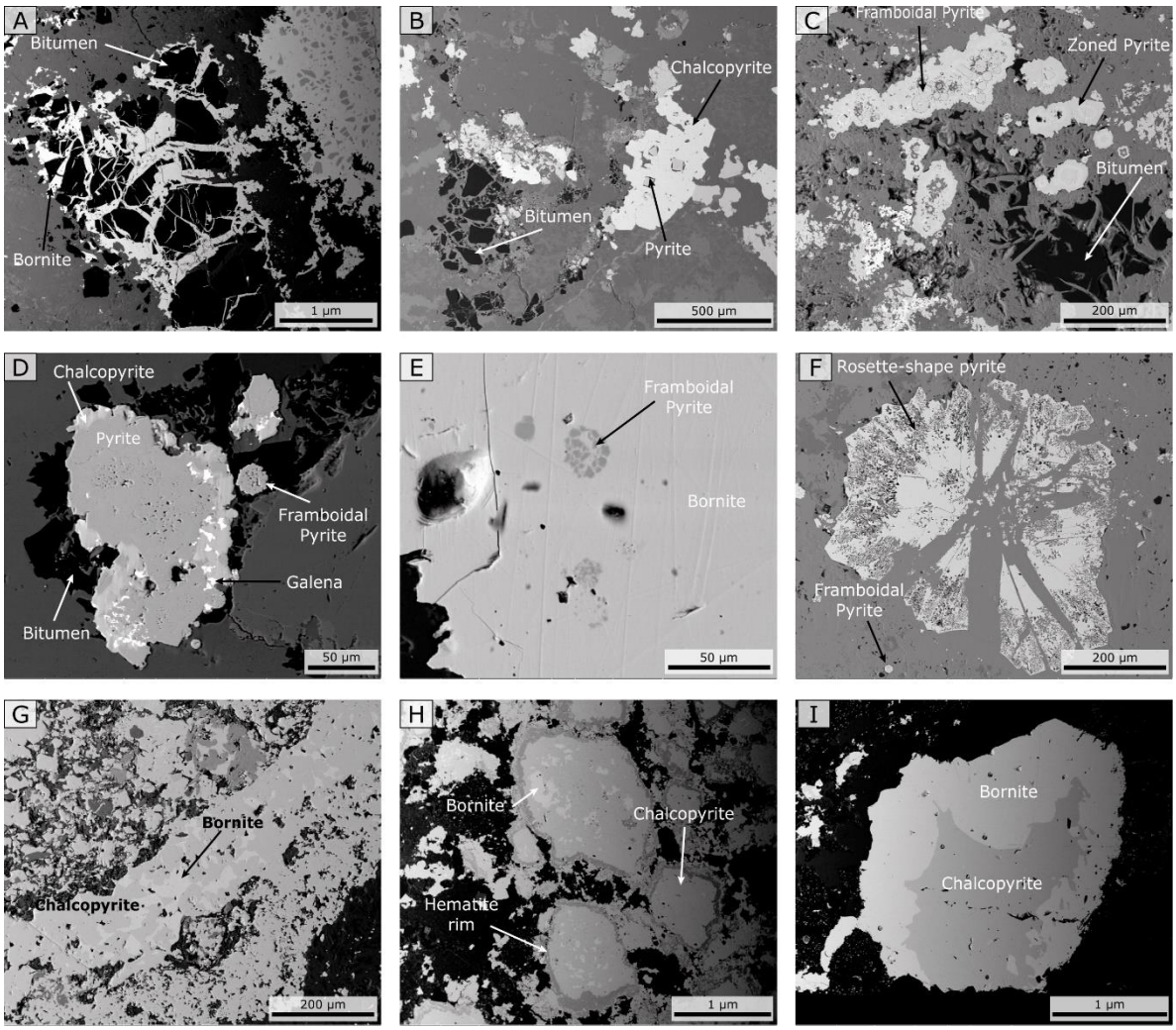

Figura 8. *SEM backscattered electron (BSE) images showing representative pre-ore and ore stage assemblages. (A) Bornite filling fractures in bitumen. (B) Euhedral pyrite surrounded by chalcopyrite. (C) Cracked bitumen and framboidal pyrite from the pre-ore stage surrounded by pyrite from the ore stage (D) Framboidal pyrite in close association with bitumen. Pyrite grains partially replaced by chalcopyrite. Also observed are galena inclusions. (E) Framboidal pyrite replaced by bornite. (F) Rosette-shaped pyrite. (G) Abundant bornite replacing chalcopyrite. (H) Bornite replacing chalcopyrite grains with hematite rims. (I) Bornite replacing a chalcopyrite grain.*

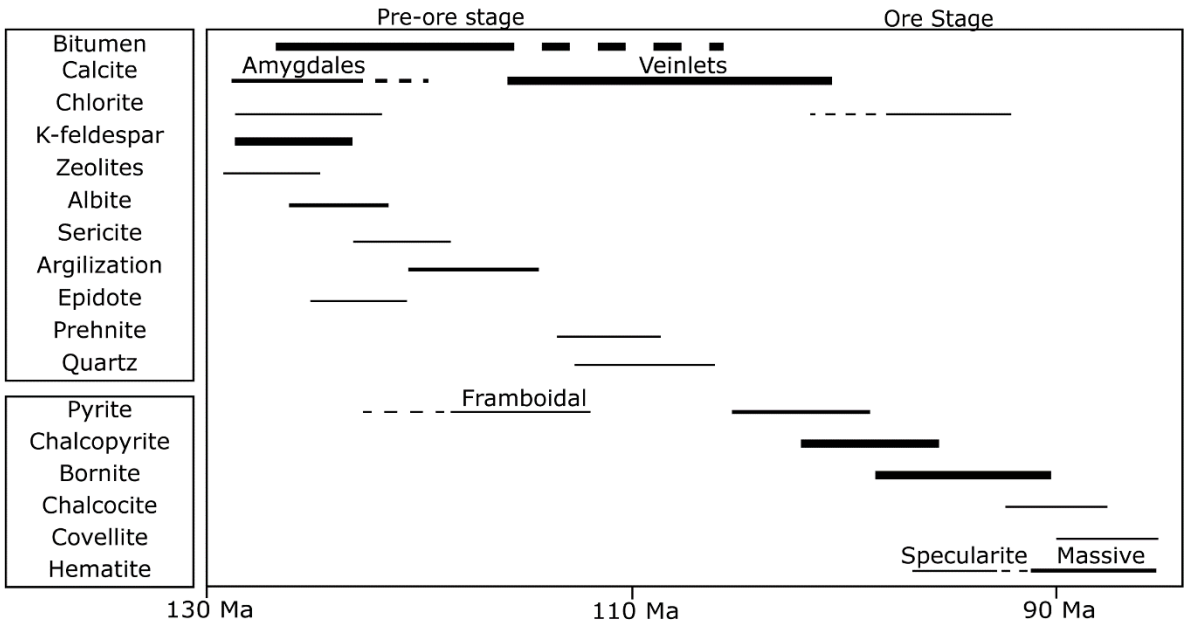

Figura 9. *Paragenetic sequence for the El Soldado deposit. The thickness of the lines reflects relative amounts: high, intermediate, and low. Dashed lines denote uncertainty regarding the extent of the mineral temporality. Ages are based on the work of Boric et al. (2002).*

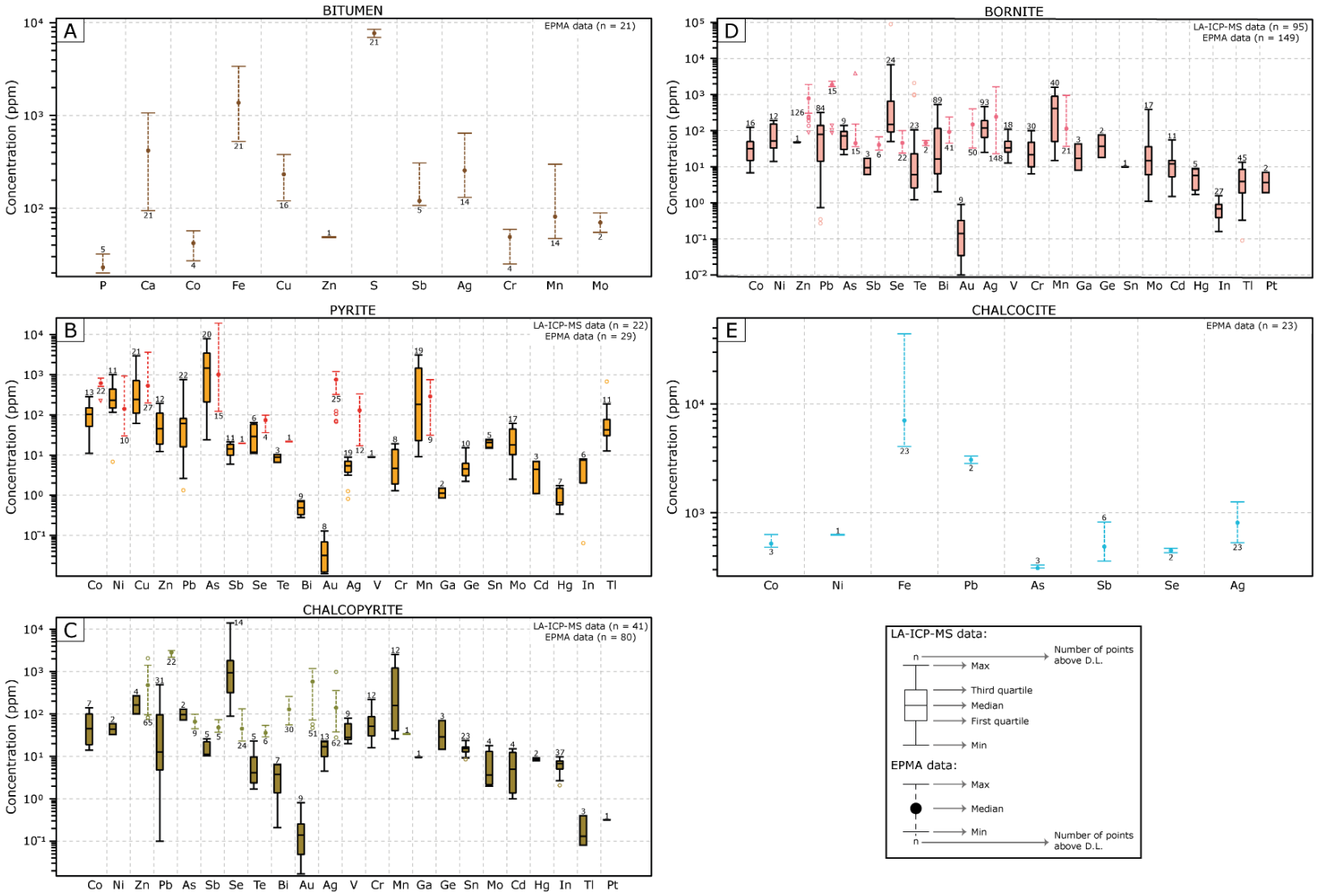

Figura 10. *Boxplot diagram for minor and trace elements in bitumen (A), pyrite (B), chalcopyrite (C), bornite (D) and chalcocite (E) from El Soldado deposit. EPMA statistics are shown as segmented lines or brackets, and LA-ICP-MS data are shown as boxes. Element concentration is in parts per million (ppm), plotted on a vertical logarithmic scale. Outliers are indicated as circles and triangles for each element above and below brackets and boxes, respectively. A circle outlier is considered as >1.5 × (Q3-Q1) from the box, and a triangle outlier is >3.0 × (Q3-Q1) from the box.*

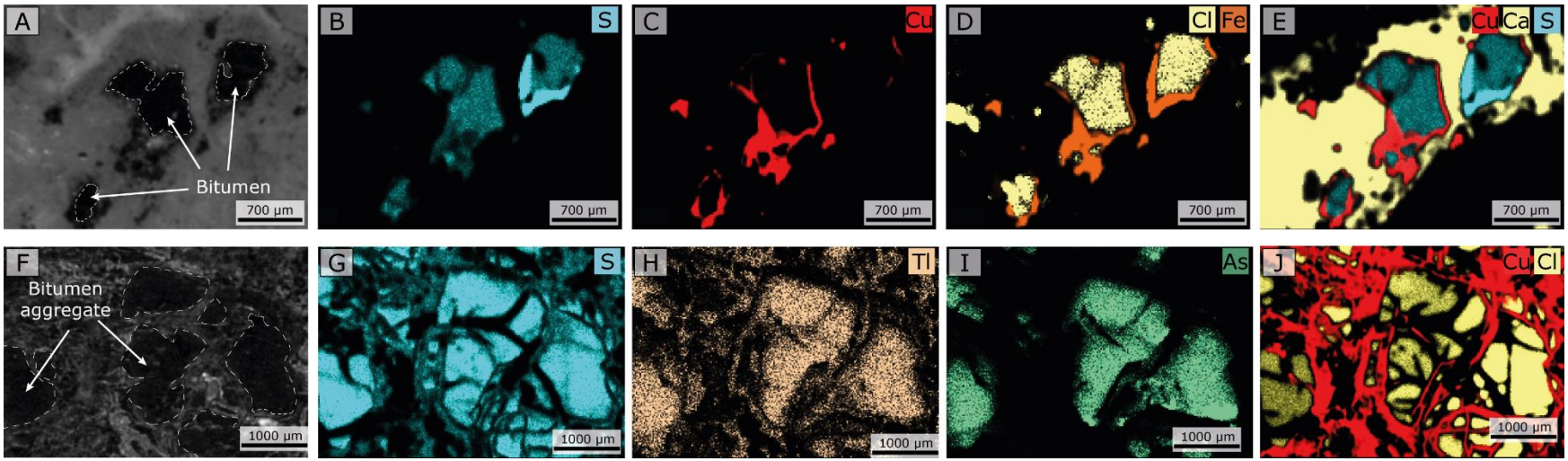

Figura 11. *µ-XRF elemental maps of bitumen grain from the El Soldado deposit. (A) and (F) show BSE images of the mapped areas*

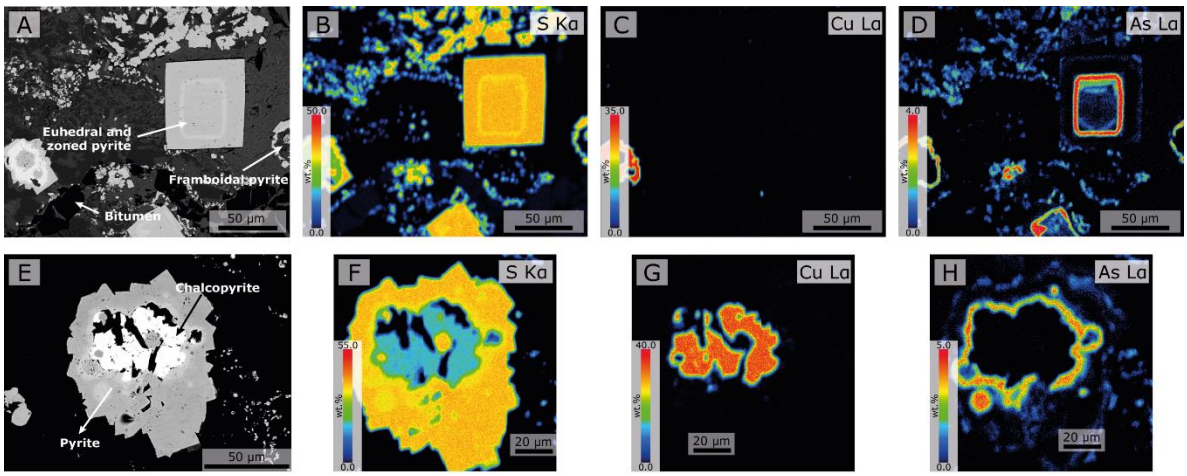

Figura 12. *Electron microprobe WDS X-ray maps of euhedral from El Soldado (B-D). Panels F-H show maps of a composite chalcopyrite-pyrite grain. Color bars indicate the wt.% elemental concentration. (A) and (E) show BSE images of the sulfide grains analyzed.*

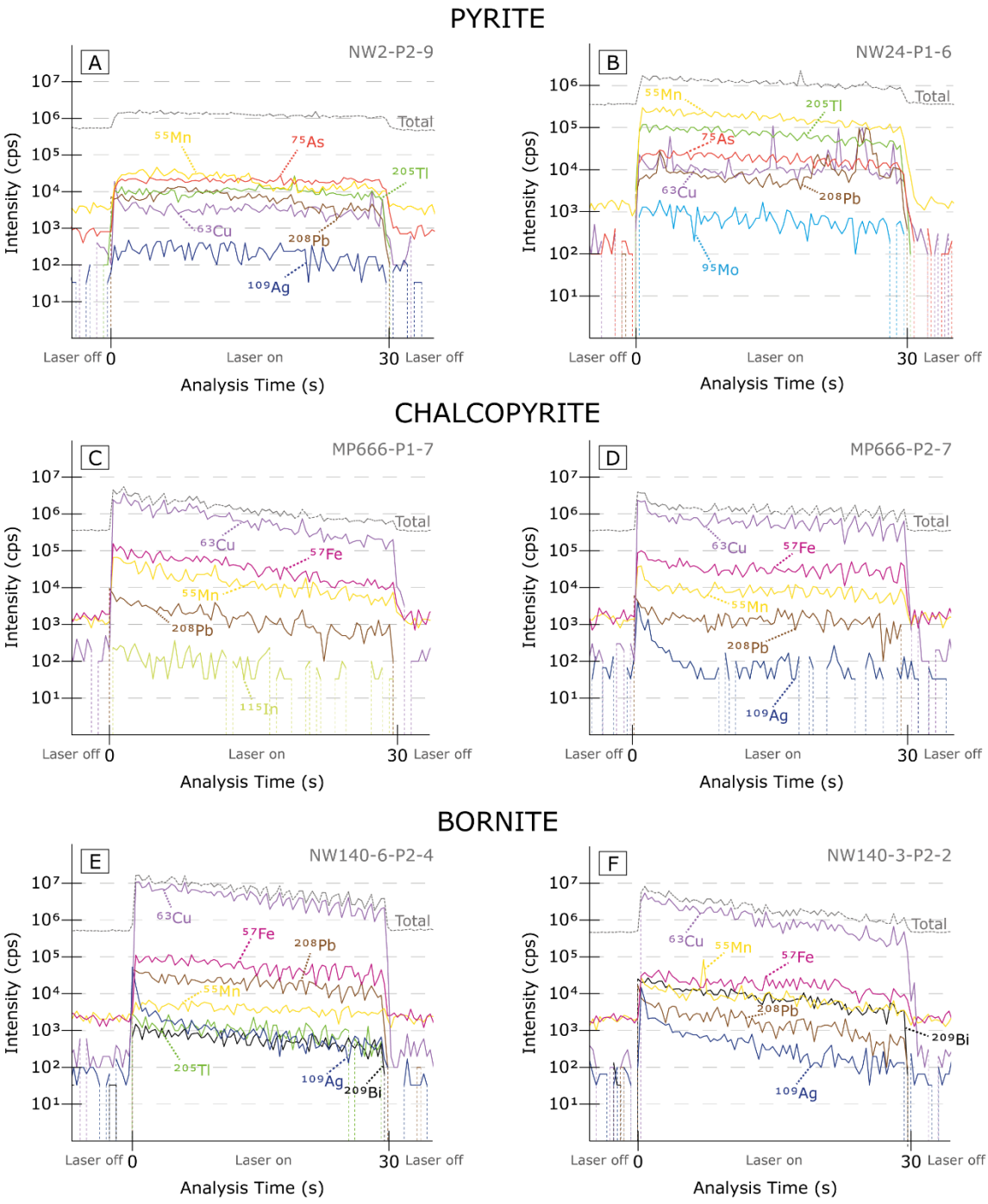

Figura 13. *LA-ICP-MS depth-concentration profiles (time vs. intensity) of selected isotopes in Cu-(Fe) sulfides from El Soldado deposit. (A-B) Pyrite profiles show concentration spectra for ^{55}Mn, ^{63}Cu, ^{75}As, ^{95}Mo, ^{109}Ag, ^{205}Tl and ^{208}Pb. (C-D) Chalcopyrite profiles for ^{55}Mn, ^{57}Fe, ^{63}Cu, ^{109}Ag, ^{115}In and ^{208}Pb. (E-F) Bornite profiles for ^{55}Mn, ^{57}Fe, ^{63}Cu, ^{109}Ag, ^{205}Tl, ^{208}Pb and ^{209}Bi.*

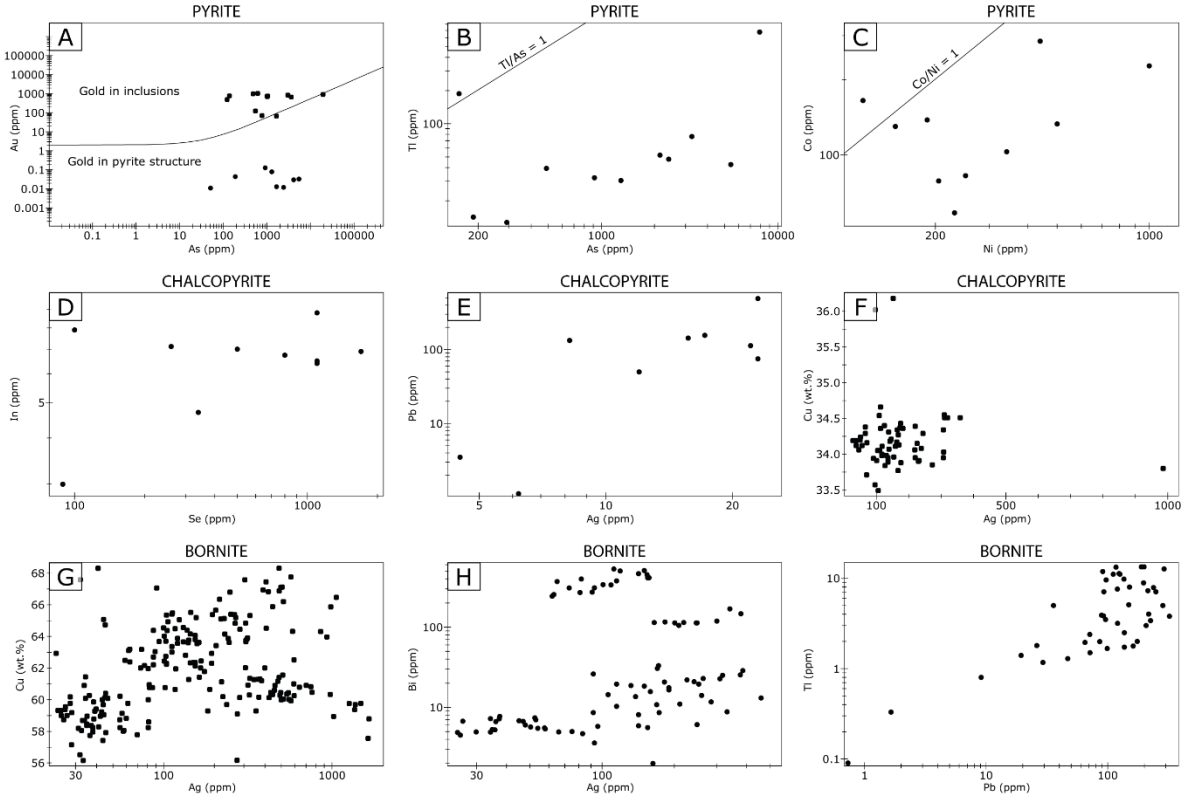

Figura 14. *Elemental biplots for pyrite, chalcopyrite and bornite from the El Soldado deposit. (A) Au (ppm) vs. As (ppm) scatterplot for pyrite. Circles indicate LA-ICP-MS data, while squares indicate EPMA values. The solubility limit is defined by Reich et al. (2005). (B) Tl (ppm) vs. As (ppm) scatterplot for pyrite. The solubility limit is defined by Deditius and Reich (2016). (C) Co (ppm) vs. Ni (ppm) scatterplot for pyrite. (D) In (ppm) vs. Se (ppm) scatterplot for chalcopyrite. (E) Pb (ppm) vs. Ag (ppm) scatterplot for chalcopyrite. (F) Cu (wt.%) vs. Ag (ppm) scatterplot for chalcopyrite. Only EPMA data are used for this plot. (G) Cu (wt.%) vs. Ag (ppm) scatterplot for bornite. Only EPMA data are used for this plot. (H) Bi (ppm) vs. Ag (ppm) scatterplot for bornite. (I) Tl (ppm) vs. Pb (ppm) scatterplot for bornite.*

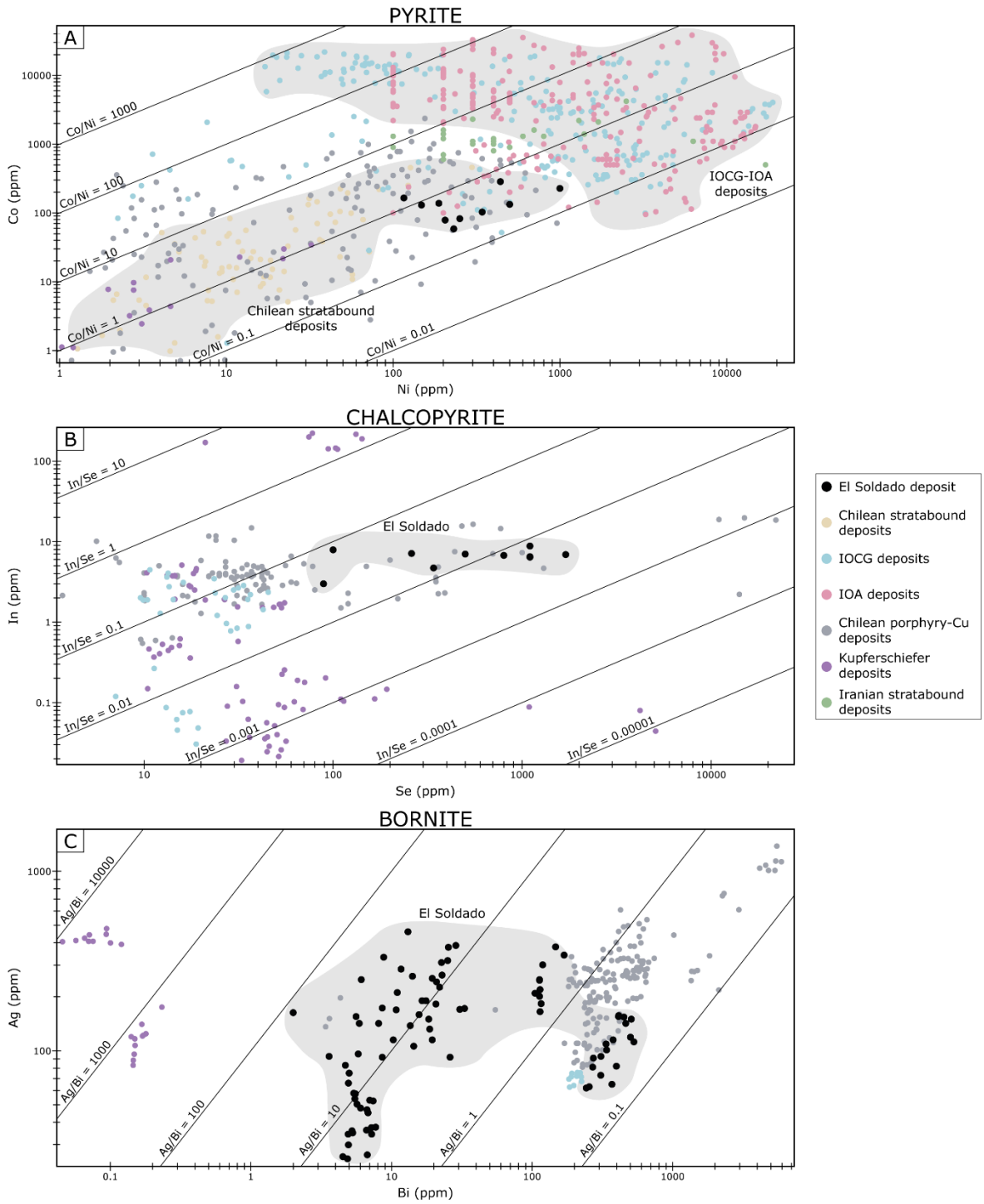

Figura 15. *Elemental concentration scatterplots for pyrite (A), chalcopyrite (B) and bornite (C) from El Soldado, compared with other deposits in Chile and elsewhere. Data source: Chilean stratabound Cu-(Ag) deposits (Lorena, Manto Cobrizo, La Culebra; Herazo et al., 2021), IOCG deposits (Candelaria, Marcona, Mina Justa pyrite; del Real et al., 2020; Li et al., 2017, 2018; Jaguar chalcopyrite; Mansur et al., 2023; and Olympic Dam bornite; Cook et al., 2011), IOA deposits (Los Colorados, El Romeral; Reich et al., 2016; Rojas et al., 2018), Chilean porphyry-Cu deposits (Chuquicamata and Río Blanco; Rivas et al., 2021; Crespo et al., 2020), Kupferschiefer deposits (Foltyn et al., 2022), and Iranian stratabound Cu deposits (Sadati et al., 2016).*

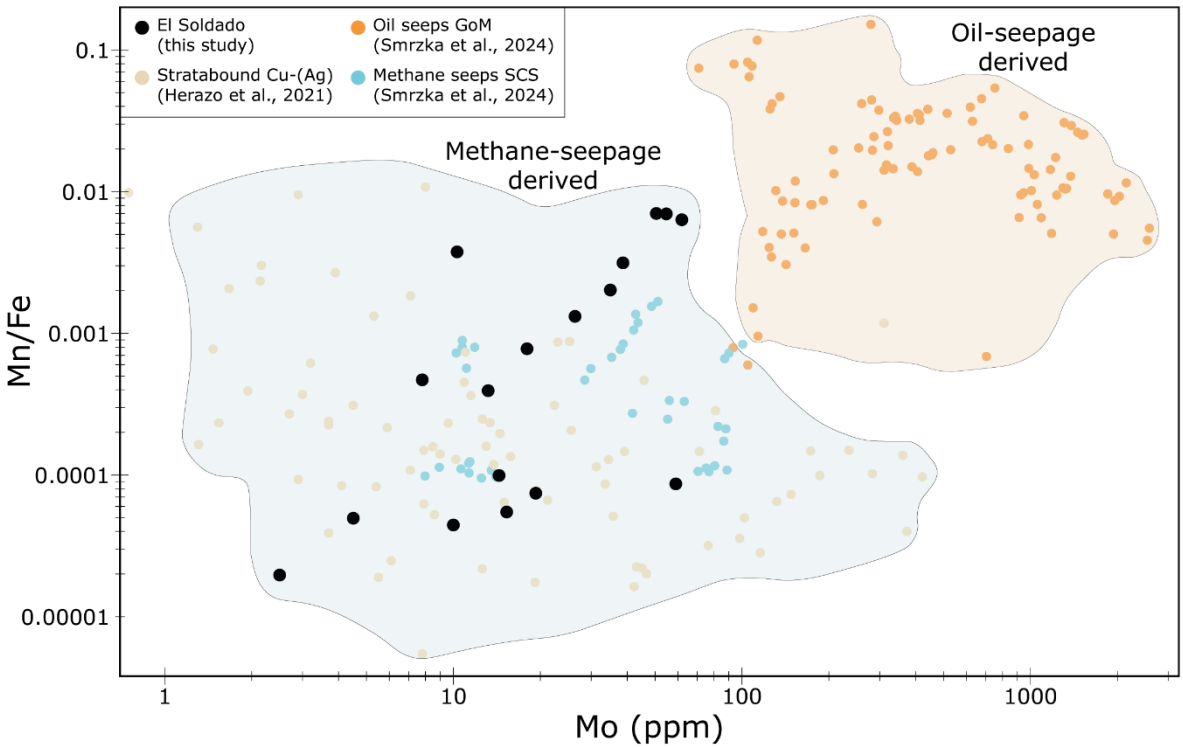

Figura 16. *Mn/Fe ratios vs. Mo plot for pyrite from the El Soldado deposit and sedimentary environments. Data source: Chilean stratabound Cu-(Ag) deposits (Herazo et al., 2021), Gulf of Mexico and South China Sea (Smrzka et al., 2024). The two fields shown were defined by Smarzka et al. (2024), i.e., pyrite derived from methane-seeps and from crude oil-seeps.*

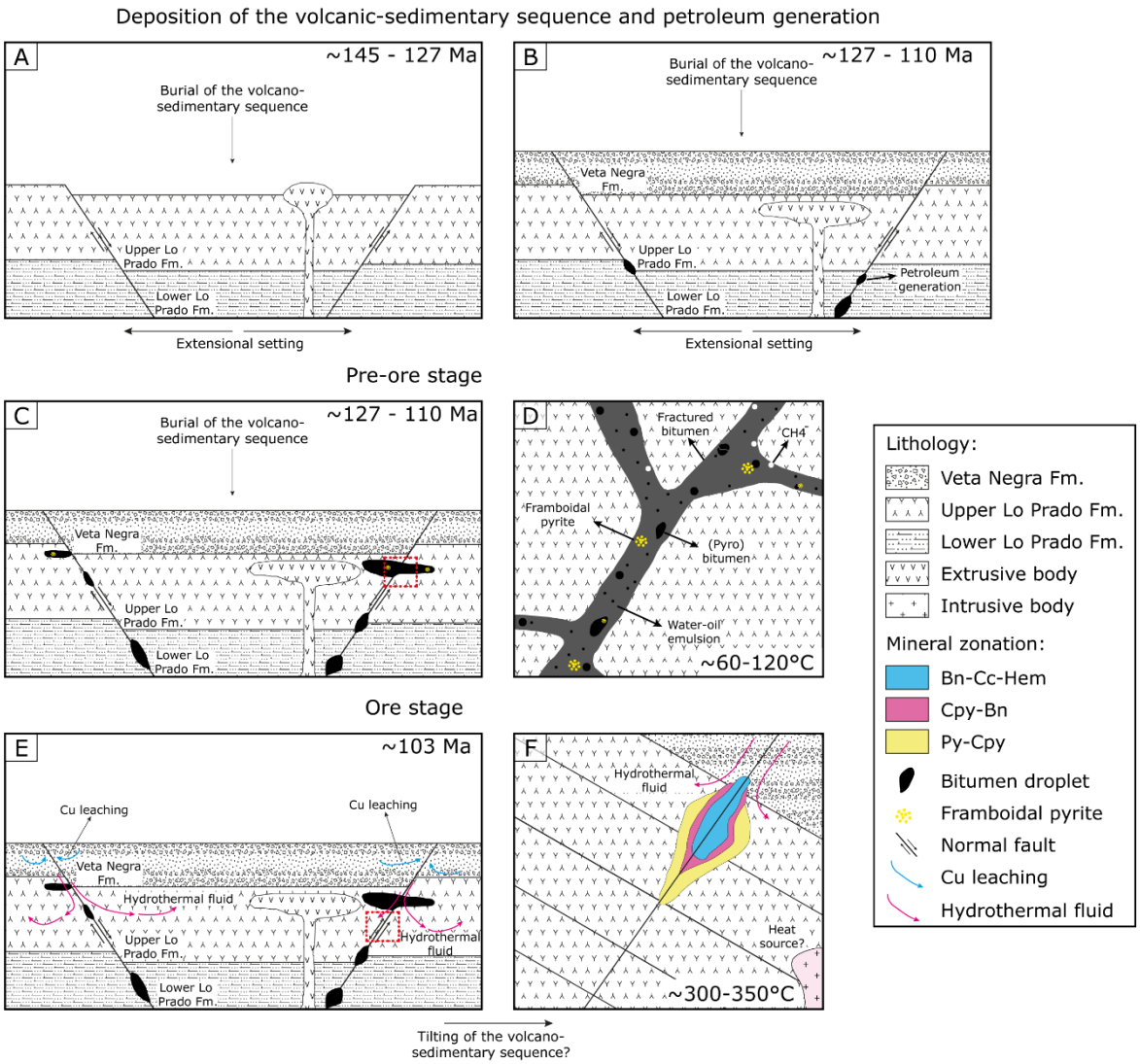

Figura 17. *Genetic model proposed for the El Soldado deposit, modified from Wilson (1998) and Boric (2002). (A) and (B) Deposition of the volcano-sedimentary host sequence and generation of petroleum in the source rocks (lower member Lo Prado Fm.). (C) and (D) Petroleum migrated upward into Lo Prado Fm. (upper member); framboidal pyrite was formed within the organic phase and host rock. Rising temperatures due to continued burial of the strata led to oil maturation and bitumen formation (pre-ore assemblage). (E) and (F) The Cu mineralization formed from hydrothermal fluids of derived from connate waters, which circulated through faults/fractures in the volcano-sedimentary sequence, leaching Cu and other metals. Some Cu(-Fe) sulfides precipitated by reduction with bitumen and replaced pre-ore pyrite. Bitumen was transformed into (pyro)bitumen due to reaction with the hydrothermal fluid. The ore bodies show a characteristic zoning with a high Cu grade (bornite-chalcocite) core grading outward to lower Cu grades. Figure not to scale.*

CAPÍTULO 3:
CONCLUSIONES

El estudio de la geoquímica de sulfuros ha cobrado relevancia durante los últimos años, sobre todo con el desarrollo de técnicas analíticas cada vez más precisas, capaces de detectar y cuantificar un amplio espectro de concentraciones de elementos en distintas fases minerales. En este contexto, el presente estudio proporciona nuevos antecedentes acerca de la química mineral de sulfuros de Cu-(Fe) del yacimiento estratoligado de Cu-(Ag) de El Soldado, ubicado en la Cordillera de la Costa de Chile Central.

Los resultados indican que los sulfuros de ganga (pirita) y mena (calcopirita, bornita, calcosina) presentes en El Soldado presentan concentraciones significativas de elementos traza, en rangos que varían desde decenas a miles de ppm, incluso llegando a niveles de wt.%. Dentro de los sulfuros analizados, se tiene que la pirita es el principal huésped de elementos traza del depósito, incorporando Mn, Co, Ni, Cu, As, Mo, Ag, Tl y Pb. Por otra parte, la bornita alberga elementos como Mn, Se, Mo, Ag, Tl y Pb, mientras que la calcopirita, el principal mineral de mena del depósito, incorpora concentraciones menores de Mn, Se, Ag, In y Pb. Finalmente, la calcosina es un huésped menor de elementos traza, incorporando Fe y Ag. Los elementos detectados se encuentran mayoritariamente en forma de solución sólida, pero también pueden ocurrir formando micro a nano-inclusiones minerales.

Elementos traza tales como el V, Mn, Ni, Mo y Tl, incorporados en los sulfuros de El Soldado, son característicos de ambientes sedimentarios marinos, lo cual estaría relacionado con la abundante presencia de bitumen dentro de las muestras analizadas, proveniente del miembro inferior de la Fm. Lo Prado. La presencia de dichos elementos en los sulfuros de mena indicaría que éstos pudieron haber sido heredados desde esta fuente sedimentaria como resultado de reacciones de reemplazo mineral de las asociaciones de pirita-bitumen preexistentes (o de pre-mena) ocurridas durante la etapa de mineralización de cobre. Por otra parte, los análisis de µ-XRF en granos de bitumen indican que esta fase incorpora elementos como S y Cl de manera homogénea, probablemente debido a la interacción con fluidos hidrotermales, en concordancia con lo planteado por Wilson & Zentilli (1999). Sin embargo, aún es necesario investigar con mayor detalle la posible contribución de metales y ligantes que podría realizar la materia orgánica en El Soldado.

Al ser comparadas con otros tipos de depósitos chilenos y del mundo, las signaturas geoquímicas de los sulfuros de El Soldado indican una fuerte componente sedimentaria en la mineralización, la cual estaría caracterizada por la abundancia de materia orgánica, por la prevalencia de condiciones reducidas, y por fluidos hidrotermales de temperaturas intermedias (≤350°C). Dichos fluidos hidrotermales tendrían un origen variado, incluyendo una mezcla de fluidos connatos, meteóricos y marinos, con una potencial contribución menor de fluidos magmáticos-hidrotermales. En particular, se tiene que las razones de Co/Ni en pirita generan campos distintivos para los depósitos estratoligados chilenos, mientras que las razones de Ag/Bi en bornita de El Soldado, muestra ciertas similitudes con depósitos de carácter sedimentario (i.e., depósitos de tipo Kupferschiefer

y estratoligados de Cu-(Ag) iraníes). La razón In/Se en calcopirita no muestra diferencias significativas, y pareciera no discriminar de manera efectiva mineralización de bajas a intermedias temperaturas. Es por esto que, particularmente en el caso de la pirita, la razón Co/Ni puede ser una herramienta útil para la exploración de depósitos de características similares a los estratoligados de Cu-(Ag), y podría potencialmente ser utilizada en los depósitos de la Cordillera de la Costa.

El modelo genético propuesto en el presente estudio es coincidente con los estudios de Wilson (1998) y Boric (2002), sugiriendo dos etapas de formación para El Soldado. La primera etapa, ocurrida entre los 127 y 110 Ma, involucra el enterramiento de la secuencia volcano-sedimentaria, y la formación de pirita framboidal y petróleo líquido a temperaturas menores a 120°C, con migración del petróleo hacia el miembro superior de la Fm. Lo Prado a través de fallas normales y estructuras preferenciales. La etapa principal de mineralización de cobre, generada aproximadamente a los 103 Ma, se caracterizó por la presencia de fluidos hidrotermales de temperaturas intermedias (≤350°C) que habrían circulado de manera descendente a través de la roca huésped, provocando una lixiviación de los metales (ej. Cu). Dichos fluidos interactuaron con la asociación mineral de la etapa de pre-mena, propiciando la precipitación de calcopirita, bornita y calcosina, que habrían heredado la signatura sedimentaria de la primera etapa de formación del depósito.

Para futuros estudios, se recomienda ampliar la base de datos presentada en este trabajo, por ejemplo, centrando los esfuerzos en el análisis sistemático de bitumen y de fases minerales de alteración. Asimismo, aún es necesario mayores estudios para comprender la fuente de los metales y del fluido hidrotermal, por lo cual es fundamental realizar análisis geoquímicos en las rocas hospedantes, para comprender a cabalidad el rol que pudo haber jugado la lixiviación y la materia orgánica en el proceso mineralizador. Dichos análisis, en conjunto con datos isotópicos in-situ de azufre, proporcionarán información adicional y de utilidad orientada a la identificación tanto de la naturaleza de los fluidos, como de los procesos fisicoquímicos de precipitación. Se sugiere además realizar estudios similares en otros depósitos estratoligados de Cu-(Ag) de la franja metalogénica la Cordillera de la Costa de Chile, centrando el estudio en la geoquímica de sulfuros de Cu-Fe (calcopirita y bornita), las cuales, a pesar de corresponder a los principales sulfuros de mena de este tipo de depósito, no han sido estudiados con detalle. Dichos datos podrían ser de utilidad al momento de generar herramientas exploratorias adecuadas basadas en la geoquímica de sulfuros.

Finalmente, se tiene que la caracterización de la concentración y distribución de elementos traza en los sulfuros de depósitos estratoligados de Cu-(Ag) es fundamental para identificar elementos críticos que son de gran relevancia para la actual transición energética y avance tecnológico global (ej. Mn, Co, Cu, Ga, Se, Ag, In, Au). Además, algunos de los elementos identificados en este estudio (ej. As, Tl) son potencialmente dañinos para el medio ambiente y la salud humana, por lo cual la identificación de estos y de su especiación en los minerales es esencial para prevenir posibles daños y pérdidas económicas.

BIBLIOGRAFÍA

Aberg, G., Aguirre, L., Levi, B., & Nystrom, J.O., 1984, Spreading-subsidence and generation of ensialic marginal basins: an example from the early Cretaceous of central Chile (B.P. Kokelaar & M.F. Howells, Eds.): Geological Society, London, Special Publications, v. 16, p. 185–193.

Affouri, H., Montacer, M., & Disnar, J.R., 2013, Organic geochemistry of the cenomanian-turonian bahloul formation petroleum source rock, central and northern Tunisia: Resource Geology, v. 63, p. 262–287.

Aguirre, L., Féraud, G., Morata, D., Vergara, M., & Robinson, D., 1999, Time interval between volcanism and burial metamorphism and rate of basin subsidence in a Cretaceous Andean extensional setting: Tectonophysics, v.313, p. 433–447.

Anglo American, 2022, Ore Reserves and Mineral Resources Report 2021, 54 p.

Boric, R., 2002, Geology, Mineral Zoning, and Lithochemistry of The El Soldado Manto Type Copper Deposit, Chile. MSc Thesis: Halifax, Canadá, Dalhousic University: 250 p.

Boric, R., Holmgren, C., Wilson, N., & Zentilli, M., 2002, The Geology Of The Soldado Manto Type Cu (Ag) Deposit, Central Chile: Hydrothermal Iron Oxide Copper-Gold & Related Deposits: A Global Perspective, v. 2, p. 163–184.

Boyce, D., Charrier, R., & Farías, M., 2020, The First Andean Compressive Tectonic Phase: Sedimentologic and Structural Analysis of Mid-Cretaceous Deposits in the Coastal Cordillera, Central Chile (32°50′S): Tectonics, v. 39, 24 p.

Charrier, R., Pinto, L., & Rodríguez, M.P., 2007, Tectonostratigraphic evolution of the Andean Orogen in Chile, in Moreno, T. and Gibbons, W. eds., The Geology of Chile: London, The Geological Society, p. 21–114.

Cisternas, M.E., & Hermosilla, J., 2006, The role of bitumen in strata-bound copper deposit formation in the Copiapo area, Northern Chile: Mineralium Deposita, v. 41, p. 339–355.

Coira, B., Davidson, John, Mpodozis, C., & Ramos, V., 1982, Tectonic and Magmatic Evolution of the Andes of Northern Argentina and Chile: Earth-Science Reviews, v. 18, p. 303–332.

Fuchs, S., Schumann, D., Williams-Jones, A.E., and Vali, H., 2015, The growth and concentration of uranium and titanium minerals in hydrocarbons of the Carbon Leader Reef, Witwatersrand Supergroup, South Africa: Chemical Geology, v. 393–394, p. 55–66.

Fuentes, F., Féraud, G., Aguirre, L., & Morata, D., 2005, $^{40}Ar/^{39}Ar$ dating of volcanism and subsequent very low-grade metamorphism in a subsiding basin: example of the Cretaceous lava series from central Chile: Chemical Geology, v. 214, p. 157–177.

Gaupp, R., Möller, P., Lüders, V., Di Primio, R., Littke, R., Urai, J.L., Nover, G., Zwach, C., Ondrak, R., Schöner, R., Krooss, B.M., Cramer, B., Plessen, B., & Machel, H.G., 2008, Fluid in

sedimentary basins: An overview, in Dynamics of Complex Intracontinental Basins: The Central European Basin System: Springer Berlin Heidelberg, p. 346–458.

George, L.L., Cook, N.J., & Ciobanu, C.L., 2016, Partitioning of trace elements in co-crystallized sphalerite-galena-chalcopyrite hydrothermal ores: Ore Geology Reviews, v. 77, p. 97–116.

Holmgren, C., 1987, Antecedentes para un modelo genético del yacimiento El Soldado, V Región de Valparaíso: Revista Geológica de Chile, p. 3–18.

Jara, J.J., Barra, F., Reich, M., Morata, D., Leisen, M., & Romero, R., 2021a, Geochronology and petrogenesis of intrusive rocks in the Coastal Cordillera of northern Chile: Insights from zircon U-Pb dating and trace element geochemistry: Gondwana Research, v. 93, p. 48–72.

Jara, J.J., Barra, F., Reich, M., Leisen, M., Romero, R., & Morata, D., 2021b, Episodic construction of the early Andean Cordillera unravelled by zircon petrochronology: Nature Communications, v. 12, 8 p.

Klohn, E., Holmgren, C., & Ruge, H., 1990, El Soldado, a Stratabound Copper Deposit Associated with Alkaline Volcanism in the Central Chilean Coastal Range, in Fontboté, G., Amstutz, G.C., Cardozo, M., Cedillo, E., and Frutos, J. eds., Stratabound ore deposits in the Andes: Special Publication of the Society for Geology Applied to Mineral Deposits, p. 435–448.

Kojima, S., Trista-Aguilera, D., & Hayashi, K.I., 2009, Genetic Aspects of the Manto-Type Copper Deposits Based on Geochemical Studies of North Chilean Deposits: Resource Geology, v. 59, p. 87–98.

Large, R., Bull, S., & Maslennikov, V., 2011, A carbonaceous sedimentary source-rock model for Carlin-type and orogenic gold deposits: Economic Geology, v. 106, p. 331–358.

Maksaev, V., & Zentilli, M., 2002, Chilean Strata-Bound Cu-(Ag) Deposit: Overview: Hydrothermal Iron Oxide Copper-Gold & Related Deposits: A Global Perspective, v. 2, p. 185–205.

Maksaev, V., Townley, B., Palacios, C., & Camus, F., 2007, Metallic Ore Deposits, in Moreno, T. and Gibbons, W. eds., The Geology of Chile: London, The Geological Society of London, p. 177–199.

Movahednia, M., Maghfouri, S., Fazli, N., Rastad, E., Ghaderi, M., & González, F.J., 2022, Metallogeny of Manto-type stratabound Cu-(Ag) mineralization in Iran: Relationship with NeoTethyan evolution and implications for future exploration: Ore Geology Reviews, v. 149, 28 p.

Mpodozis, C., & Allmendinger, R.W., 1993, Extensional tectonics, Cretaceous Andes, northern Chile (27°S): Geological Society of America Bulletin, v. 105, p. 1462–1477.

Mpodozis, C., & Kay, S., 1990, Provincias magmáticas ácidas y evolución tectónica de Gondwana: Andes chilenos (28-31°S).: Revista Geológica de Chile, v. 17, p. 153–180.

Mpodozis, C., & Ramos, V., 1989, The Andes of Chile and Argentina, in Ericksen, G.E., Cañas-Pinochet, M.T., and Reinemund, J.A. eds., Geology of the Andes and its relation to hydrocarbon

and mineral resources: Texas, Circumpacific Council for Energy and Mineral Resources. Earth Science Series, p. 59–90.

Nasi, C., & Thiele. R, 1982, Estratigrafía del Jurásico y Cretácico de la Cordillera de la Costa, al sur del Río Maipo, entre Melipilla y Laguna de Aculeo (Chile central): Revista Geológica de Chile, v. 16, p. 81–99.

Ojeda, A., Barra, F., Reich, M., Romero, R., and Tapia, M.J., 2024, Evolution and fertility of magmas associated with iron oxide-apatite (IOA) deposits, Coastal Cordillera, Northern Chile: A zircon petrochronology perspective: Gondwana Research, v. 131, p. 38–56.

Oliveros, V., Féraud, G., Aguirre, L., Ramírez, L., Fornari, M., Palacios, C., & Parada, M., 2008, Detailed $^{40}Ar/^{39}Ar$ dating of geologic events associated with the Mantos Blancos copper deposit, northern Chile: Mineralium Deposita, v. 43, p. 281–293.

Oliveros, V., Vásquez, P., Creixell, C., Lucassen, F., Ducea, M.N., Ciocca, I., González, J., Espinoza, M., Salazar, E., Coloma, F., & Kasemann, S.A., 2020, Lithospheric evolution of the Pre- and Early Andean convergent margin, Chile: Gondwana Research, v. 80, p. 202–227.

Parnell, J., Kucha, H., & Landais, P., 1993, Bitumens in Ore Deposits: Springer Berlin Heidelberg, 517 p.

Perona, J., Canals, À., & Cardellach, E., 2018, Zn-Pb mineralization associated with salt diapirs in the basque-cantabrian Basin, Northern Spain: Geology, geochemistry, and genetic model: Economic Geology, v. 113, no. 5, p. 1133–1159.

Ramos, V., & Aleman, A., 2000, Tectonic evolution of the Andes. In: Cordani, U.G. et al (editors).: Tectonic Evolution of South America, p. 635–685.

Rivano, S., 1993, Hoja Quillota y Portillo. Servicio Nacional de Geología y Minería.: Carta Geológica de Chile N°73, no. Carta Geológica de Chile N°73, p. 202p.

Rivano, S., 1996, Geología de las Hojas Quillota y Portillo 1:250.000. Servicio Nacional de Geología y Minería: Carta Geológica de Chile, no. 73; 202 p.

Ruiz, C., Aguirre, L., Corvalan, J., Klohn, C., & Klohn, E., 1965, Geología y yacimientos metalíferos de Chile: Instituto de Investigaciones Geológicas, Santiago, Chile., 302 p.

Ruiz, J., Freydier, C., McCandless, T., Chesley, J., & Munizaga, F., 1997, Re-os-isotope systematics of sulfides from base-metal porphyry and manto-type mineralization in chile: International Geology Review, v. 39, p. 317–324.

Saintilan, N.J., Spangenberg, J.E., Chiaradia, M., Chelle-Michou, C., Stephens, M.B., & Fontboté, L., 2019, Petroleum as source and carrier of metals in epigenetic sediment-hosted mineralization: Scientific Reports, v. 9, 7 p.

Sato, T., 1984, Manto type copper deposits in Chile: a review: Bulletin of the Geological Survey of Japan, v. 35, p. 565–582.

Servicio Nacional de Geología y Minería, 2023, Anuario de la minería de Chile 2022: Servicio Nacional de Geología y Minería. 240 p

Spirakis, C.S., & Heyll, A. V, 1993, Organic Matter (Bitumen and Other Forms) as the Key to Localisation of Mississippi Valley-Type Ores: Special Publication of the Society for Geology Applied to Mineral Deposits, v. 9, p. 381–398.

Tosdal, R.M., & Munizaga, F., 2003, Lead sources in Mesozoic and Cenozoic Andean ore deposits, north-central Chile (30-34°S): Mineralium Deposita, v. 38, p. 234–250.

Vergara, M., Levi, B., Nyström, J. o, & Cancino, A., 1995, Jurassic and Early Cretaceous island arc volcanism, extension, and subsidence in the Coast Range of central Chile: Geological Society of American Bulletin, v. 107, p. 1427–1440.

Wilson, N., 1998, The role of petroleum in the formation of The El Soldado copper deposit, Chile: Hydrotermal replacement of a biodegrades petroleum reservoirPh. D Thesis: Halifax, Canada, Dalhousie University: 418 p.

Wilson, N., & Zentilli, M., 1999, The Role of Organic Matter in the Genesis of the El Soldado Volcanic-Hosted Manto-Type Cu Deposit, Chile: Economic Geology, v. 94, p. 1115–1136.

Wilson, N., Zentilli, M., & Spiro, B., 2003a, A sulfur, carbon, oxygen, and strontium isotope study of the volcanic-hosted El Soldado Manto-Type copper deposit, Chile: The essential role of bacteria and petroleum: Economic Geology, v. 98, p. 163–174.

Wilson, N., Zentilli, M., Reynolds, P.H., & Boric, R., 2003b, Age of mineralization by basinal fluids at the El Soldado manto-type copper deposit, Chile: 40Ar/39Ar geochronology of K-feldspar: Chemical Geology, v. 197, p. 161–176.

Wilson, N.S.F., & Zentilli, M., 2006, Association of pyrobitumen with copper mineralization from the Uchumi and Talcuna districts, central Chile: International Journal of Coal Geology, v. 65, p. 158–169.

Zentilli, M., Boric, R., Munizaga, F., & Graves, M.C., 1994, Petroleum involvement in the genesis of some strata-bound copper deposits of Chile, in 7th Chilean Geological Congress, Concepción, Chile, II: p. 1542–1546.

Zentilli, M., Munizaga, F., Graves, M.C., Boric, R., Wilson, N.S.F., Mukhopadhyay, P.K., & Snowdon, L.R., 1997, Hydrocarbon Involvement in the Genesis of Ore Deposits: An Example in Cretaceous Stratabound (Manto-Type) Copper Deposits of Central Chile: International Geology Review, v. 39, 21 p.

ANEXOS

ANEXO A: Muestras analizadas

En el siguiente anexo se presenta un resumen de las secciones transparentes pulidas analizadas mediante diversas técnicas analíticas, así como también la litología de la roca huésped (Wilson, 1998), y la principal mineralización presente.

Sample	SEM	EPMA	LA-ICP-MS	µ-XRF	Orebody	Lithology (Wilson, 1998)	Mineralization
MP-688	X	X	X	-	Osorno	Pink rhyolite	Fr. py, ccp, bn
NW-2	X	X	X	X	Filo	Rhyolite	Py, ccp, bit
NW-121	X	X	X	-	Filo	Porous rhyolite/breccia	ccp, bn
MP-699	X	X	X	-	Osorno	Rhyolite	ccp, bn, hem
MP-893	X	X	X	-	Santa Clara	Rhyolite	ccp, bn
NW-24	X	X	X	X	Filo	Porphrytic andesite	Fr. py, py, ccp, bit
NW-140-6	-	X	X	X	Filo	Green andesite	ccp, bn, bit
MP-666	-	X	X	-	Osorno	Red rhyolite	Bn, cct
NW-140-3	-	X	X	X	Filo	Green breccia andesite	Bn, bit
NW-127-1	X	-	-	-	Santa Clara	Rhyolite autobreccia	Py, bn
NW-46-1	X	-	-	X	Filo	Green porphrytic andesite	Py, bn, cct, bit
NW-107	X	-	-	X	Filo	Brecciated rhyolite	Py, ccp, bn, bit
NW-29	X	-	-	X	Filo	Andesite	Fr. py, py, bit, sph
NW-137	-	-	-	X	Filo	Yellow/green andesite	Bit
NW-6	-	-	-	X	Filo	Breccia rhyolite	ccp, bn, bit
NW-137-v2	-	-	-	X	Filo	Yellow/green andesite	Py, bit
NW-33	-	-	-	X	Filo	Rhyolite	Py, ccp, bit
NW-27	-	-	-	X	Filo	Porphrytic andesite	ccp, bn, bit

ANEXO B: Anexo metodológico

B.1. Microscopía electrónica de barrido

Con el fin de identificar a detalle las texturas y asociaciones minerales presentes en las muestras del depósito, se realiza un análisis mediante un microscopio electrónico de barrido (SEM). Estos análisis fueron llevados a cabo en el Centro de Excelencia en Geotermia de los Andes (CEGA), Universidad de Chile, utilizando un equipo FEI Quanta 250, el cual se encuentra equipado con detectores de electrones secundarios (SE), de electrones retrodispersados (BSE), de dispersión de energía de rayos X (EDS) y con detectores de cátodoluminiscencia (CL).

Las condiciones analíticas utilizadas fueron un voltaje de aceleración de 20 kV, un haz de diámetro de 5 µm y una distancia de trabajo de 10.5 mm.

B.2. Microsonda electrónica (EPMA)

Para obtener la concentración de los elementos mayores y menores en el bitumen y las principales fases sulfuradas de El Soldado (i.e., pirita, calcopirita, bornita y calcosina), se utiliza un equipo JEOL JXA-85530-F Hyperprobe, en el laboratorio EPMA, en la Universidad de Rice, Houston, Texas. Los análisis se realizaron en dos sesiones distintas, la primera de ellas realizada durante el mes de agosto del año 2022, y la segunda realizada en el mes de diciembre del mismo año.

Las condiciones analíticas utilizadas en el caso de los sulfuros fueron las siguientes: un voltaje de aceleración de 15 kV, una corriente del haz de 150 nA, y un diámetro del haz de electrones de 500 nm para la pirita y calcopirita, 10 µm en el caso de la bornita, y 700 nm para el caso de la calcosina. Además, se realizan análisis puntuales en granos de bitumen, utilizando las siguientes condiciones: un voltaje de aceleración de 15 kV, una corriente del haz de 50 nA, y un diámetro del haz de electrones entre 400 nm a 2 µm. Durante la realización de los análisis, se presta cuidadosa atención a la presencia de fracturas, irregularidades y/o inclusiones, de manera de no alterar los resultados. Los límites de detección para cada una de las fases analizadas son las siguientes: Para el caso de pirita los valores varían entre 0.0093 y 0.017 wt.%, para la calcopirita entre 0.023 y 0.21 wt.%, entre 0.0024 y 0.32 wt.% para el caso de la bornita, y entre 0.007 y 0.110 wt.% para el caso de la calcosina. Finalmente, en el caso de los granos de bitumen, los límites de detección de los distintos elementos analizados varían entre 0.0014 y 0.125 wt.%. El detalle de las medianas de cada uno de los límites de detección se puede obtener en el Anexo C.

Además, se realizan mapas de rayos X por espectrometría de dispersión de longitud de onda (WDS) en granos de pirita y calcopirita, usando un voltaje de 15 kV y una corriente del haz de 50 nA.

En la siguiente tabla se detallan los cristales dispersivos de ondas, las líneas espectrales utilizadas, los segundos de análisis realizados en el peak y en el background, la posición del peak, y los materiales de calibración utilizado para cada uno de los análisis.

Elemento	Cristal	Línea espectral	Peak (s)	Background (s)	Peak Position	Material de calibración
Pirita						
S	PETJ	Kα	20	10	172,084	FeS_2
Mn	LIFL	Kα	40	30	146,225	$Mn^{2+}SiO_3$
Co	LIF	Kα	80	60	124,561	Co^0
Fe	LIF	Kα	20	10	134,775	$CuFeS_2$
Ni	LIFH	Kα	80	60	115,458	$(Ni, Fe)_9S_8$
Ag	PETH	Lα	80	60	133,121	Ag^0
Au	PETH	Mα	60	60	187,009	Au^0
Se	TAP	Lα	80	60	97,717	Bi_2Se_3
As	TAP	Lα	80	60	105,129	FeAsS
Cu	TAP	Lα	80	60	144,875	$CuFeS_2$
Te	PETL	Lα	80	60	105,334	Te^0
Sb	PETL	Lα	80	60	110,196	Sb_2S_3
Bi	PETL	Mα	80	60	163,882	Bi_2Se_3
Calcopirita y bornita						
S	PETJ	Kα	20	10	172,069	FeS_2
Mn	LIFL	Kα	40	30	146,225	$Mn^{2+}SiO_3$
Fe	LIF	Kα	20	10	134,767	$CuFeS_2$
Ag	PETH	Lα	80	60	133,121	Ag^0
Au	PETH	Mα	80	60	187,009	Au^0
Zn	LIFH	Kα	80	60	99,986	ZnS
Se	TAP	Lα	80	60	97,717	Bi_2Se_3
As	TAP	Lα	80	60	105,129	FeAsS
Cu	TAP	Lα	80	60	144,875	$CuFeS_2$
Te	PETL	Lα	80	60	105,334	Te^0
Sb	PETL	Lα	80	60	110,196	Sb_2S_3
Bi	PETL	Mα	80	60	163,882	Bi_2Se_3
Pb	PETL	Mα	80	60	169,257	PbS
Calcosina						
S	PETJ	Kα	20	10	172,084	FeS_2
Fe	LIF	Kα	40	30	134,767	$CuFeS_2$
Ag	PETH	Lα	40	30	133,121	Ag^0
Au	PETH	Mα	40	30	187,009	Au^0
Zn	LIFH	Kα	40	30	99,986	ZnS
Se	TAP	Lα	40	30	97,717	Bi_2Se_3
As	TAP	Lα	40	30	105,129	FeAsS
Cu	TAP	Lα	40	30	144,875	$CuFeS_2$
Te	PETL	Lα	40	30	105,334	Te^0
Sb	PETL	Lα	40	30	110,196	Sb_2S_3
Bi	PETL	Mα	40	30	163,882	Bi_2Se_3
Pb	PETL	Mα	40	30	169,257	PbS

Bitumen						
C	LDE2	Kα	10	5	127,982	C^0
Ag	PETJ	Lα	10	5	0	Ag^0
Sb	PETJ	Lα	10	5	110,185	Sb_2S_3
Ca	PETJ	Kα	20	10	107,637	$CaMg(CO_3)_2$
Zn	TAP	Lα	60	40	133,519	ZnS
Cu	TAP	Lα	60	40	144,875	$CuFeS_2$
As	TAP	Lα	60	40	105,129	FeAsS
Fe	LIF	Kα	60	40	134,759	$(Mg, Fe)_2SiO_4$
P	PETH	Kα	20	10	197,098	P_2O_5
Cr	LIFH	Kα	40	30	159,376	$FeCr_2O_4$
Co	LIFH	Kα	60	40	124,505	Co^0
O	LDE1	Kα	20	10	110,497	Fe_3O_4
S	PETL	Kα	20	10	172,072	FeS_2
Mo	PETL	Lβ	60	40	165,817	Mo^0
Mn	LIFL	Kα	10	5	146,257	$Mn^{2+}SiO_3$

B.3. Espectrometría de masas por plasma inductivamente acoplado con ablación láser (LA-ICP-MS)

Para la obtención de concentraciones de elementos traza en pirita, calcopirita y bornita se utiliza un análisis de espectrometría de masas por plasma inductivamente acoplado con ablación láser (LA-ICP-MS) utilizando un equipo de ArF excímero de 193 nm acoplado a un cuadrupolo ICP-MS (Thermo Fisher Scientific iCAP Q), disponible en el Laboratorio de Espectrometría de Masas del Departamento de Geología, Universidad de Chile. El protocolo utilizado para el análisis de sulfuros fue el detallado por Román et al. (2019).

Los análisis fueron divididos en rondas de 15-20 puntos, y previo y al final de cada una de las rondas se miden los estándares externos primarios (MASS-1; Wilson et al. 2002), y externos secundarios (GSE-1; Jochum et al. 2005), de forma de realizar un control de calidad. Además, como estándar interno, se utilizan las concentraciones de 57Fe obtenidas previamente mediante EPMA. El diámetro del haz fue generalmente de 40 µm, pero fue reducido a 25 µm para evitar ablacionar zonas con presencia de inclusiones, fracturas o rayas. En cuanto a los tiempos de cada análisis, se tiene que cada punto es ablacionado por aproximadamente 52.5 segundos, con un tiempo de 30 segundos de lectura en el background. Además, se utiliza una tasa de frecuencia de pulso de láser de 4 Hz, y una energía de 2.5 J/cm2, utilizando He puro como el gas portador. Para asegurar niveles aceptables de robustez del plasma, producción de óxido y producción de doble carga se ablaciona el material NIST SRM 610.

Los isótopos medidos para cada uno de los sulfuros son: 34S, 51V, 52Cr, 53Cr, 55Mn, 59Co, 60Ni, 63Cu, 65Cu, 66Zn, 69Ga, 72Ge, 73Ge, 75As, 77Se, 82Se, 95Mo, 97Mo, 107Ag, 109Ag, 111Cd, 115In, 118Sn, 120Sn, 121Sb, 123Sb, 125Te, 195Pt, 197Au, 202Hg, 205Tl, 206Pb, 207Pb, 208Pb, 209Bi. Finalmente, la reducción y procesamiento de los datos se realiza utilizando el

software Iolite (v. 3.6.3; Paton et al. 2011). El detalle de los límites de detección para cada uno de los elementos se puede obtener en el Anexo D.

B.4. Micro-fluorescencia de rayos X (µ-XRF)

Con el fin de identificar la distribución de metales y ligantes en la materia orgánica presente en el depósito, se realizan mapas elementales en granos de bitumen utilizando un espectrómetro de micro-fluorescencia de rayos X Bruker M4 Tornado Plus, en el Laboratorio de Nutrición Vegetal, Universidad de Talca, Chile. El instrumento se encuentra equipado con un tubo rayos X de rodio que opera a 50 kV y 600 µA. El tamaño del haz y la distancia entre los puntos analizados fue de 20 µm para obtener una buena resolución del resultado. Para el procesamiento de los datos e imágenes se utiliza el software ESPRIT.

B.5. Referencias anexo metodológico

Jochum, K.P., Willbold, M., Raczek, I., Stoll, B., & Herwig, K., 2005, Chemical characterisation of the USGS reference glasses GSA-1G, GSC-1G, GSD-1G, GSE-1G, BCR-2G, BHVO-2G and BIR-1G using EPMA, ID-TIMS, ID-ICP-MS and LA-ICP-MS: Geostandards and Geoanalytical Research, v. 29, p. 285–302.

Paton, C., Hellstrom, J., Paul, B., Woodhead, J., & Hergt, J., 2011, Iolite: Freeware for the visualisation and processing of mass spectrometric data: Journal of Analytical Atomic Spectrometry, v. 26, no. 12, p. 2508–2518.

Román, N., Reich, M., Leisen, M., Morata, D., Barra, F., & Deditius, A.P., 2019, Geochemical and micro-textural fingerprints of boiling in pyrite: Geochimica et Cosmochimica Acta, v. 246, p. 60–85.

Wilson, S.A., Ridley, W.I., & Koenig, A.E., 2002, Development of sulfide calibration standards for the laser ablation inductively-coupled plasma mass spectrometry technique: Journal of Analytical Atomic Spectrometry, v. 17, p. 406–409.

ANEXO C: Resultados EPMA

C.1. Pirita

Anexo equivalente a *Appendix B-Pyrite* indicado en el manuscrito del Capítulo 2. Las concentraciones se muestran en porcentaje en peso (wt.%). "bdl" indica los valores que se encuentran bajo el límite de detección, el cual se puede identificar debajo de cada uno de los elementos analizados.

	S 0.0026	**Mn** 0.0026	**Fe** 0.0090	**Co** 0.0032	**Ni** 0.0034	**Cu** 0.0093	**Zn** 0.0000	**As** 0.0038	**Se** 0.0028	**Ag** 0.0050	**Sb** 0.0017	**Te** 0.0017	**Au** 0.0038	**Pb** 0.0000	**Bi** 0.0038	**Total**
NW-24	51.56	-	44.70	bdl	0.05	0.05	-	0.16	bdl	bdl	0.00	bdl	0.01	-	bdl	96.54
NW-24	50.39	-	44.50	0.02	0.09	0.06	-	1.93	bdl	0.00	bdl	bdl	0.09	-	bdl	97.09
NW-24	52.01	-	45.16	bdl	bdl	0.02	-	0.01	bdl	0.00	bdl	0.00	0.08	-	bdl	97.29
NW-24	52.00	-	44.95	bdl	bdl	0.03	-	0.01	bdl	0.00	bdl	bdl	0.05	-	bdl	97.05
NW-24	51.62	-	44.73	bdl	bdl	0.03	-	0.36	bdl	0.00	bdl	bdl	0.07	-	bdl	96.82
NW-24	51.79	-	44.73	bdl	0.00	0.03	-	0.05	bdl	bdl	bdl	bdl	bdl	-	bdl	96.60
NW-24	51.69	-	44.75	bdl	0.01	0.04	-	0.06	bdl	bdl	bdl	bdl	0.10	-	bdl	96.65
NW-24	51.81	-	44.44	bdl	0.00	0.04	-	0.30	bdl	bdl	bdl	bdl	0.08	-	bdl	96.68
NW-2	53.37	bdl	46.37	0.07	bdl	0.21	bdl	bdl	0.01	0.01	bdl	bdl	bdl	bdl	bdl	100.05
NW-2	53.30	bdl	46.69	0.05	bdl	0.10	bdl	bdl	bdl	0.03	bdl	bdl	0.01	bdl	bdl	100.19
NW-2	53.24	0.00	46.32	0.05	bdl	0.13	bdl	bdl	bdl	0.03	bdl	bdl	0.10	bdl	bdl	99.88
NW-2	53.29	bdl	46.29	0.06	bdl	0.10	bdl	bdl	bdl	0.02	bdl	bdl	0.03	bdl	bdl	99.80
NW-2	53.28	bdl	46.56	0.07	bdl	0.14	bdl	bdl	0.01	bdl	bdl	bdl	0.09	bdl	bdl	100.15
NW-2	53.31	bdl	46.19	0.06	bdl	0.36	bdl	bdl	bdl	bdl	bdl	bdl	0.10	bdl	bdl	100.03
NW-2	53.50	bdl	46.65	0.06	bdl	0.07	bdl	bdl	0.00	bdl	bdl	bdl	0.05	bdl	bdl	100.33
NW-2	53.44	bdl	46.66	0.06	bdl	0.10	bdl	bdl	0.01	bdl	bdl	bdl	0.10	bdl	bdl	100.37
NW-2	53.03	0.00	46.34	0.05	bdl	0.19	bdl	bdl	bdl	bdl	bdl	bdl	0.12	bdl	bdl	99.73
NW-2	53.50	bdl	46.48	0.06	bdl	0.12	bdl	bdl	bdl	bdl	bdl	bdl	0.06	bdl	bdl	100.23
NW-2	53.08	0.07	46.33	0.07	bdl	0.02	bdl	0.05	bdl	0.01	bdl	bdl	0.01	bdl	bdl	99.66
NW-2	53.28	0.06	46.46	0.06	bdl	0.02	bdl	bdl	bdl	0.01	bdl	bdl	0.08	bdl	bdl	99.97

NW-2	52.88	bdl	46.20	0.05	bdl	bdl	bdl	bdl	bdl	0.01	bdl	bdl	bdl	bdl	bdl	99.15
NW-2	52.77	0.02	46.40	0.08	0.02	0.05	bdl	0.05	bdl	bdl	bdl	bdl	0.10	bdl	bdl	99.49
NW-2	53.16	0.06	46.32	0.08	bdl	0.05	bdl	0.08	bdl	0.03	bdl	bdl	0.01	bdl	bdl	99.79
NW-2	52.92	bdl	46.42	0.06	0.01	0.05	bdl	bdl	bdl	bdl	bdl	bdl	0.09	bdl	bdl	99.54
NW-2	52.95	bdl	46.47	0.06	0.01	0.06	bdl	0.10	bdl	bdl	bdl	bdl	0.08	bdl	bdl	99.73
NW-2	53.08	0.03	46.28	0.07	0.02	0.06	bdl	bdl	bdl	bdl	bdl	bdl	0.05	bdl	bdl	99.59
NW-2	52.77	bdl	46.25	0.06	0.03	0.04	bdl	0.71	bdl	bdl	bdl	bdl	bdl	bdl	bdl	99.85
NW-2	53.18	0.02	46.32	0.07	bdl	bdl	bdl	0.10	bdl	bdl	bdl	bdl	0.07	bdl	bdl	99.77
NW-2	53.06	0.08	46.42	0.07	bdl	0.03	bdl	0.10	bdl	bdl	bdl	bdl	0.08	bdl	bdl	99.83

	Estadística															
	S	**Mn**	**Fe**	**Co**	**Ni**	**Cu**	**Zn**	**As**	**Se**	**Ag**	**Sb**	**Te**	**Au**	**Pb**	**Bi**	**Total**
Mínimo	50.39	0.003	44.44	0.023	0.003	0.020	-	0.012	0.004	0.002	0.002	0.002	0.007	-	-	96.54
Máximo	53.50	0.075	46.69	0.083	0.094	0.363	-	1.930	0.010	0.033	0.002	0.002	0.120	-	-	100.37
Mediana	53.06	0.029	46.32	0.061	0.016	0.053	-	0.101	0.007	0.013	0.002	0.002	0.076	-	-	99.73
Promedio	52.73	0.038	45.94	0.062	0.024	0.082	-	0.272	0.007	0.015	0.002	0.002	0.067	-	-	99.03
Sobre l.d.	29	9	29	22	10	27	-	15	4	12	1	1	25	-	-	29

C.2. Calcopirita

Anexo equivalente a *Appendix B-Chalcopyrite* indicado en el manuscrito del Capítulo 2. Las concentraciones se muestran en porcentaje en peso (wt.%). "bdl" indica los valores que se encuentran bajo el límite de detección, el cual se puede identificar debajo de cada uno de los elementos analizados.

	S 0.0027	**Mn** 0.0028	**Fe** 0.0090	**Cu** 0.0210	**Zn** 0.0058	**As** 0.0035	**Se** 0.0027	**Ag** 0.0023	**Sb** 0.0034	**Te** 0.0027	**Au** 0.0045	**Pb** 0.0070	**Bi** 0.0053	**Total**
MP-688	34.87	bdl	29.90	34.07	bdl	bdl	bdl	0.01	bdl	bdl	0.05	bdl	bdl	98.91
MP-688	34.72	bdl	29.43	36.02	bdl	0.00	bdl	0.01	bdl	bdl	0.07	bdl	0.01	100.26
MP-699	35.12	bdl	30.18	34.03	0.06	bdl	bdl	0.03	bdl	bdl	0.06	bdl	bdl	99.49
MP-699	35.32	bdl	31.52	34.51	0.01	bdl	bdl	0.03	bdl	bdl	0.01	bdl	bdl	101.40
MP-699	35.32	bdl	30.39	34.51	0.05	bdl	bdl	0.04	0.00	bdl	bdl	bdl	bdl	100.31
MP-699	35.45	bdl	30.47	34.55	bdl	bdl	bdl	0.03	bdl	bdl	0.05	bdl	bdl	100.55
MP-699	35.49	bdl	30.50	34.43	0.07	bdl	0.01	0.02	bdl	bdl	0.03	bdl	bdl	100.55
MP-699	35.58	bdl	30.68	34.12	0.07	bdl	bdl	0.01	bdl	bdl	bdl	bdl	0.01	100.47
MP-699	35.34	bdl	30.62	34.54	0.06	bdl	bdl	0.01	bdl	bdl	0.08	bdl	bdl	100.65
MP-699	35.50	bdl	30.67	34.66	bdl	bdl	bdl	0.01	bdl	bdl	bdl	bdl	0.01	100.86
MP-699	35.17	bdl	30.71	34.19	bdl	0.01	bdl	0.00	bdl	bdl	bdl	bdl	bdl	100.08
MP-699	35.59	bdl	30.74	34.24	bdl	bdl	0.00	0.01	bdl	bdl	bdl	bdl	0.01	100.60
MP-699	35.65	bdl	30.71	34.38	0.03	0.00	bdl	0.01	bdl	0.00	bdl	bdl	0.01	100.79
MP-699	35.49	bdl	30.37	34.47	0.05	bdl	bdl	bdl	bdl	0.00	0.01	bdl	bdl	100.40
MP-699	34.95	bdl	30.45	34.34	bdl	bdl	bdl	0.03	bdl	bdl	0.06	0.29	0.01	100.12
MP-699	35.11	bdl	30.54	34.36	bdl	0.01	0.01	0.02	bdl	0.00	0.07	bdl	0.01	100.12
MP-699	35.02	bdl	30.58	34.39	0.01	bdl	bdl	0.02	bdl	bdl	0.02	0.28	0.01	100.34
MP-699	35.00	bdl	30.49	34.34	0.06	bdl	bdl	0.02	bdl	bdl	0.03	bdl	0.02	99.95
MP-699	34.99	bdl	30.11	34.51	0.05	0.01	bdl	0.03	bdl	bdl	0.10	0.29	bdl	100.09
MP-699	34.99	bdl	30.63	34.36	bdl	bdl	bdl	0.01	bdl	bdl	0.03	bdl	0.02	100.04
MP-699	34.98	bdl	30.46	34.08	0.01	bdl	0.01	0.02	bdl	bdl	0.09	0.28	bdl	99.93
MP-699	34.89	bdl	30.56	34.27	0.05	bdl	bdl	0.02	bdl	bdl	bdl	0.24	bdl	100.04
MP-699	34.95	bdl	30.25	34.31	0.01	bdl	0.01	0.01	bdl	bdl	bdl	0.30	0.02	99.86
MP-699	34.77	bdl	30.66	34.06	0.02	bdl	bdl	0.02	bdl	bdl	0.07	0.31	0.01	99.92

MP-699	34.95	bdl	30.77	33.88	0.05	bdl	0.00	0.02	bdl	0.00	0.01	0.31	bdl	99.99
MP-699	34.80	bdl	30.77	33.90	bdl	bdl	bdl	0.02	bdl	bdl	bdl	0.26	bdl	99.75
MP-699	35.05	bdl	30.92	34.00	0.03	bdl	bdl	0.01	bdl	bdl	0.03	bdl	bdl	100.05
MP-699	35.00	bdl	30.62	33.85	bdl	bdl	0.01	0.03	bdl	bdl	bdl	0.22	bdl	99.72
MP-699	35.00	bdl	30.75	33.95	0.02	bdl	0.00	0.01	bdl	bdl	bdl	0.27	bdl	100.01
MP-699	35.06	bdl	30.81	34.18	0.06	bdl	bdl	0.01	bdl	0.01	bdl	bdl	bdl	100.13
MP-699	35.10	bdl	30.72	34.13	0.05	bdl	bdl	0.02	bdl	bdl	0.06	bdl	bdl	100.08
MP-699	34.81	bdl	30.50	34.15	bdl	0.01	bdl	0.02	bdl	bdl	bdl	0.22	bdl	99.72
MP-699	34.87	bdl	30.46	33.95	bdl	bdl	bdl	0.02	0.00	bdl	bdl	0.25	bdl	99.55
MP-699	34.90	bdl	30.72	33.94	0.05	bdl	bdl	0.01	bdl	bdl	0.06	0.29	bdl	99.96
MP-699	35.24	bdl	30.33	33.84	0.03	bdl	bdl	0.01	0.01	bdl	0.01	0.31	0.01	99.79
MP-699	35.13	bdl	30.47	34.17	0.06	0.01	0.00	0.02	bdl	bdl	bdl	0.31	bdl	100.16
MP-699	35.08	bdl	30.68	34.21	bdl	bdl	bdl	0.01	0.00	bdl	bdl	0.24	bdl	100.23
MP-699	35.17	bdl	30.55	34.29	0.05	bdl	bdl	0.02	bdl	bdl	0.09	bdl	bdl	100.18
MP-699	35.08	bdl	30.72	34.20	0.06	bdl	bdl	0.01	bdl	0.01	0.08	bdl	0.01	100.17
MP-699	34.97	bdl	30.70	33.89	0.01	bdl	bdl	0.01	bdl	bdl	0.01	0.28	0.01	99.88
MP-699	35.16	bdl	30.83	33.98	0.02	0.01	bdl	0.01	bdl	bdl	0.03	0.29	bdl	100.32
MP-699	35.11	bdl	30.60	34.29	0.01	bdl	bdl	0.01	bdl	bdl	bdl	0.31	bdl	100.33
MP-699	35.10	bdl	31.05	34.11	bdl	0.01	bdl	0.02	bdl	bdl	0.04	0.28	0.01	100.61
MP-699	34.96	bdl	30.93	34.11	0.05	bdl	bdl	0.01	bdl	bdl	0.06	0.29	bdl	100.41
MP-893	34.72	bdl	29.52	33.91	0.05	bdl	0.01	0.02	bdl	bdl	0.07	bdl	bdl	98.29
MP-893	34.81	bdl	29.43	33.77	0.02	bdl	0.00	0.02	bdl	bdl	0.06	bdl	0.01	98.13
MP-893	34.92	bdl	29.46	33.96	0.09	bdl	bdl	0.02	bdl	bdl	0.03	bdl	bdl	98.49
MP-893	34.78	bdl	29.38	34.05	0.10	bdl	bdl	0.01	bdl	bdl	0.09	bdl	0.02	98.42
MP-893	34.99	bdl	29.61	33.84	0.07	bdl	bdl	bdl	bdl	bdl	0.01	bdl	0.02	98.54
MP-893	34.82	bdl	29.70	34.07	0.02	bdl	bdl	bdl	bdl	bdl	0.08	bdl	bdl	98.69
MP-893	34.89	bdl	29.73	34.40	0.05	bdl	0.01	0.01	bdl	bdl	0.05	bdl	bdl	99.14
MP-893	34.85	bdl	29.85	34.05	0.07	bdl	bdl	0.01	bdl	bdl	bdl	bdl	0.02	98.85
MP-893	34.83	bdl	29.80	34.19	0.03	bdl	bdl	0.00	bdl	bdl	0.06	bdl	bdl	98.92
MP-893	34.69	bdl	29.59	34.07	0.02	bdl	bdl	bdl	bdl	bdl	0.09	bdl	bdl	98.47
MP-893	34.90	bdl	29.60	33.96	0.06	bdl	0.00	bdl	bdl	bdl	0.07	bdl	bdl	98.60

MP-893	34.96	bdl	29.57	33.77	0.06	bdl	0.01	bdl	bdl	bdl	0.08	bdl	bdl	98.45
MP-893	34.82	bdl	29.50	33.99	0.05	bdl	bdl	bdl	bdl	bdl	bdl	bdl	bdl	98.37
MP-893	34.93	bdl	29.47	34.06	0.03	bdl	bdl	0.00	bdl	bdl	0.12	bdl	0.03	98.64
MP-893	35.02	bdl	29.66	34.16	0.06	bdl	0.00	0.01	bdl	bdl	bdl	bdl	bdl	98.92
MP-893	34.95	bdl	29.76	33.91	0.05	bdl	0.00	0.01	bdl	bdl	0.00	bdl	0.01	98.71
MP-893	34.94	0.00	29.79	33.98	0.05	bdl	bdl	0.01	bdl	bdl	bdl	bdl	0.01	98.79
NW-121	35.29	bdl	30.28	34.37	0.01	bdl	bdl	0.02	bdl	bdl	bdl	bdl	0.02	99.99
NW-121	35.19	bdl	30.51	34.12	0.04	bdl	bdl	0.00	bdl	bdl	0.01	bdl	bdl	99.87
NW-121	35.24	bdl	30.70	33.95	0.05	bdl	0.00	0.03	bdl	bdl	0.03	bdl	bdl	100.00
NW-121	35.15	bdl	30.60	34.35	0.05	bdl	bdl	bdl	bdl	bdl	0.09	bdl	0.01	100.25
NW-121	35.20	bdl	30.17	35.90	0.03	bdl	0.00	bdl	0.01	bdl	0.01	bdl	bdl	101.33
NW-121	35.10	bdl	30.38	36.18	0.04	bdl	0.01	0.02	bdl	bdl	bdl	bdl	bdl	101.72
NW-121	35.38	bdl	30.25	35.66	0.14	bdl	bdl	bdl	bdl	bdl	bdl	bdl	bdl	101.43
NW-121	35.27	bdl	30.51	35.79	0.21	bdl	0.01	bdl	bdl	bdl	bdl	bdl	bdl	101.79
NW-121	35.08	bdl	30.33	33.43	0.04	bdl	bdl	bdl	bdl	bdl	0.03	bdl	bdl	98.91
NW-121	34.62	bdl	30.09	33.80	0.06	bdl	bdl	0.10	bdl	bdl	bdl	bdl	bdl	98.67
NW-121	35.19	bdl	30.82	33.88	0.11	bdl	bdl	bdl	bdl	bdl	bdl	bdl	0.01	100.01
NW-121	35.14	bdl	30.74	33.71	0.05	bdl	bdl	0.01	bdl	bdl	0.00	bdl	0.02	99.68
NW-121	35.29	bdl	30.99	33.49	0.04	bdl	0.00	0.01	bdl	bdl	0.06	bdl	0.01	99.90
NW-121	35.11	bdl	30.75	33.57	0.02	bdl	bdl	0.01	bdl	bdl	0.09	bdl	0.02	99.58
NW-2	35.52	bdl	30.97	33.80	0.04	bdl	bdl	bdl	bdl	bdl	bdl	bdl	0.01	100.34
NW-2	35.65	bdl	30.96	33.89	0.07	bdl	bdl	bdl	bdl	bdl	bdl	bdl	bdl	100.58
NW-2	35.53	bdl	30.90	33.76	0.03	bdl	0.00	bdl	bdl	bdl	0.09	bdl	bdl	100.32
NW-2	35.43	bdl	30.80	33.78	0.06	bdl	0.00	bdl	bdl	bdl	0.10	bdl	bdl	100.17
NW-2	35.46	bdl	31.06	34.07	0.06	bdl	0.01	bdl	bdl	bdl	0.06	bdl	bdl	100.72

	Estadística													
	S	**Mn**	**Fe**	**Cu**	**Zn**	**As**	**Se**	**Ag**	**Sb**	**Te**	**Au**	**Pb**	**Bi**	**Total**
Mínimo	34.62	0.003	29.38	33.43	0.008	0.005	0.002	0.003	0.004	0.003	0.005	0.218	0.006	98.13
Máximo	35.65	0.003	31.52	36.18	0.207	0.010	0.013	0.099	0.007	0.005	0.118	0.314	0.026	101.79
Mediana	35.07	0.003	30.51	34.10	0.048	0.007	0.005	0.014	0.005	0.004	0.058	0.284	0.013	100.01
Promedio	35.09	0.003	30.38	34.21	0.049	0.007	0.005	0.017	0.005	0.004	0.052	0.277	0.013	99.85
Sobre l.d.	80	1	80	80	65	9	24	62	5	6	51	22	30	80

C.3. Bornita

Anexo equivalente a *Appendix B-Bornite* indicado en el manuscrito del Capítulo 2. Las concentraciones se muestran en porcentaje en peso (wt.%). "bdl" indica los valores que se encuentran bajo el límite de detección, el cual se puede identificar debajo de cada uno de los elementos analizados.

	S 0.0027	**Mn** 0.0029	**Fe** 0.0093	**Cu** 0.0322	**Zn** 0.0052	**As** 0.0036	**Se** 0.0024	**Ag** 0.0025	**Sb** 0.0044	**Te** 0.0030	**Au** 0.0046	**Pb** 0.0066	**Bi** 0.0054	**Total**
MP-688	26.48	-	11.56	62.93	bdl	bdl	bdl	0.00	bdl	bdl	bdl	bdl	bdl	100.97
MP-688	26.39	-	11.57	62.70	bdl	bdl	bdl	0.01	0.00	bdl	bdl	bdl	bdl	100.67
MP-688	26.34	-	11.59	63.11	bdl	0.00	bdl	0.01	bdl	bdl	bdl	bdl	bdl	101.05
MP-688	29.30	-	15.49	56.17	bdl	0.37	bdl	0.03	bdl	bdl	0.01	0.01	bdl	101.38
MP-688	26.35	-	11.64	62.44	bdl	bdl	bdl	0.01	bdl	bdl	0.00	bdl	bdl	100.44
MP-688	26.63	-	11.88	61.96	bdl	bdl	bdl	0.01	bdl	bdl	0.01	bdl	bdl	100.49
MP-688	26.51	-	11.68	62.24	bdl	bdl	bdl	0.01	bdl	bdl	0.00	bdl	bdl	100.44
MP-688	26.48	-	11.69	62.21	bdl	0.01	bdl	0.01	bdl	bdl	bdl	bdl	0.00	100.40
MP-688	26.71	-	11.82	61.78	bdl	bdl	bdl	0.02	0.00	bdl	0.01	bdl	bdl	100.35
MP-688	26.53	-	11.67	62.30	bdl	0.00	bdl	0.01	bdl	bdl	bdl	bdl	0.01	100.52
MP-688	26.49	-	11.67	62.33	bdl	bdl	bdl	0.01	bdl	bdl	bdl	bdl	bdl	100.50
MP-699	28.05	-	12.00	59.37	0.06	bdl	bdl	0.14	bdl	bdl	bdl	bdl	0.01	99.63
MP-699	27.92	-	12.01	59.76	0.01	bdl	bdl	0.13	bdl	bdl	bdl	0.01	0.01	99.85
MP-699	27.93	-	12.04	60.33	0.11	bdl	bdl	0.10	bdl	bdl	0.01	0.01	bdl	100.53
MP-699	27.63	-	11.98	58.94	0.07	0.00	0.01	0.10	bdl	bdl	bdl	bdl	bdl	98.74
MP-699	28.17	-	12.03	59.69	0.03	bdl	bdl	0.14	bdl	bdl	bdl	bdl	0.01	100.07
MP-699	27.83	-	12.22	59.77	0.04	bdl	bdl	0.15	bdl	bdl	0.03	bdl	bdl	100.04
MP-699	27.78	-	12.33	58.79	0.08	bdl	bdl	0.17	bdl	bdl	0.01	bdl	bdl	99.17
MP-699	26.87	-	11.95	60.32	0.10	0.00	bdl	0.04	bdl	bdl	0.01	bdl	bdl	99.30
MP-699	27.47	-	12.08	60.91	bdl	bdl	0.00	0.07	bdl	bdl	0.04	bdl	bdl	100.58
MP-699	26.77	-	12.49	60.82	0.06	0.01	bdl	0.07	0.00	bdl	0.03	bdl	bdl	100.25
MP-699	26.66	-	12.72	60.47	bdl	bdl	0.01	0.08	0.01	bdl	0.02	bdl	0.01	99.97
MP-699	27.08	-	11.94	60.90	0.09	bdl	bdl	0.05	bdl	bdl	0.01	bdl	bdl	100.06
MP-699	27.08	-	11.78	61.17	bdl	bdl	bdl	0.05	0.00	bdl	bdl	bdl	bdl	100.08

MP-699	27.39	-	11.72	60.36	bdl	0.00	bdl	0.05	bdl	bdl	bdl	bdl	0.01	99.54
MP-699	27.80	-	11.99	60.25	bdl	bdl	bdl	0.06	bdl	bdl	bdl	bdl	bdl	100.11
MP-699	27.08	-	11.76	61.27	0.02	0.01	bdl	0.03	bdl	bdl	bdl	bdl	bdl	100.18
MP-699	27.47	-	11.76	61.29	0.07	bdl	bdl	0.04	bdl	bdl	bdl	bdl	bdl	100.63
MP-699	27.05	-	11.68	60.45	0.06	bdl	bdl	0.05	bdl	bdl	bdl	bdl	bdl	99.29
MP-699	27.22	-	11.85	60.79	bdl	bdl	bdl	0.06	0.01	0.01	0.03	bdl	bdl	99.97
MP-699	26.95	-	11.75	61.56	0.02	bdl	bdl	0.05	bdl	bdl	bdl	bdl	0.01	100.35
MP-699	27.52	-	11.69	61.00	bdl	0.00	0.01	0.06	bdl	bdl	bdl	bdl	0.01	100.29
MP-699	26.93	-	11.60	61.41	bdl	bdl	bdl	0.05	bdl	bdl	bdl	bdl	bdl	99.99
MP-699	27.32	-	11.70	60.02	bdl	bdl	bdl	0.06	bdl	bdl	0.03	0.18	0.01	99.32
MP-699	27.20	-	11.77	60.04	0.08	bdl	bdl	0.05	bdl	bdl	bdl	0.23	0.01	99.39
MP-699	27.05	-	11.69	59.93	0.02	bdl	bdl	0.06	bdl	bdl	bdl	bdl	bdl	98.75
MP-699	27.08	-	11.72	60.44	0.10	0.02	bdl	0.06	bdl	bdl	bdl	0.22	bdl	99.63
MP-699	26.83	-	11.54	60.29	bdl	bdl	bdl	0.05	bdl	bdl	0.01	0.21	bdl	98.93
MP-699	27.23	-	11.68	60.16	0.09	bdl	bdl	0.04	bdl	bdl	bdl	0.20	bdl	99.40
MP-699	27.21	-	11.79	60.13	bdl	bdl	bdl	0.04	bdl	bdl	0.04	0.17	bdl	99.39
MP-699	27.03	-	11.74	60.60	0.06	0.00	bdl	0.05	bdl	bdl	bdl	0.19	bdl	99.67
MP-699	27.21	-	11.86	59.29	0.04	bdl	bdl	0.04	bdl	bdl	0.03	0.19	0.01	98.67
MP-699	27.26	-	11.96	59.99	0.09	0.00	bdl	0.05	bdl	bdl	bdl	0.21	bdl	99.56
MP-699	27.19	-	11.80	60.14	0.01	bdl	bdl	0.03	bdl	0.00	0.02	0.18	bdl	99.38
MP-699	26.85	-	11.90	60.45	0.03	bdl	bdl	0.04	bdl	bdl	0.02	0.18	0.01	99.49
MP-699	27.18	-	11.72	60.30	0.08	bdl	bdl	0.03	bdl	bdl	bdl	bdl	0.01	99.33
MP-699	27.63	-	11.66	59.29	bdl	0.01	bdl	0.02	bdl	bdl	0.03	0.21	bdl	98.84
MP-893	26.95	0.01	11.17	60.19	0.19	bdl	bdl	0.02	bdl	bdl	bdl	bdl	0.01	98.55
MP-893	27.01	bdl	10.99	60.65	0.07	bdl	bdl	0.02	bdl	bdl	0.01	bdl	bdl	98.75
MP-893	26.86	bdl	10.98	61.31	0.09	bdl	bdl	0.04	bdl	bdl	0.01	bdl	0.02	99.31
MP-893	26.85	bdl	10.62	61.13	0.12	bdl	0.00	0.02	bdl	bdl	bdl	bdl	0.01	98.75
MP-893	26.87	bdl	10.72	61.20	0.10	bdl	bdl	0.04	bdl	bdl	0.01	bdl	bdl	98.94
MP-893	26.96	bdl	11.81	61.35	0.13	bdl	bdl	0.03	bdl	bdl	bdl	bdl	bdl	100.28
MP-893	26.99	bdl	11.26	62.01	0.08	bdl	bdl	0.02	bdl	bdl	bdl	bdl	0.02	100.39
MP-893	26.73	bdl	10.18	62.52	0.08	bdl	bdl	0.06	bdl	bdl	0.01	bdl	bdl	99.58

MP-893	26.26	bdl	10.38	63.67	0.14	bdl	0.01	0.03	bdl	bdl	bdl	bdl	bdl	100.49
MP-893	27.09	bdl	10.65	62.02	0.13	bdl	0.00	0.03	bdl	bdl	0.02	bdl	0.01	99.96
MP-893	27.60	bdl	11.77	59.69	0.08	bdl	bdl	0.02	bdl	bdl	bdl	bdl	bdl	99.17
MP-893	27.11	0.01	12.25	59.10	0.08	bdl	bdl	0.03	bdl	bdl	0.01	bdl	bdl	98.59
NW-121	26.54	bdl	9.88	64.32	0.05	bdl	bdl	0.06	bdl	bdl	bdl	bdl	0.02	100.87
NW-121	26.71	bdl	10.18	64.31	0.16	bdl	bdl	0.09	bdl	bdl	bdl	bdl	bdl	101.45
NW140-3	26.70	0.02	10.10	64.02	0.15	bdl	bdl	0.01	bdl	bdl	bdl	bdl	bdl	101.01
NW140-3	26.75	0.04	9.72	63.77	0.04	bdl	bdl	0.01	bdl	bdl	bdl	bdl	bdl	100.34
NW140-3	27.11	0.02	10.69	62.14	0.09	bdl	bdl	0.02	bdl	bdl	bdl	bdl	bdl	100.06
NW140-3	26.55	bdl	9.82	64.54	0.07	bdl	bdl	0.01	bdl	bdl	bdl	bdl	0.01	101.00
NW140-3	26.65	0.08	9.89	63.60	0.08	bdl	bdl	0.01	bdl	bdl	bdl	bdl	bdl	100.32
NW140-3	26.94	bdl	9.93	63.56	0.05	bdl	bdl	0.01	bdl	bdl	bdl	bdl	0.02	100.51
NW140-3	27.07	0.10	10.02	63.20	0.08	bdl	0.01	bdl	bdl	bdl	bdl	bdl	bdl	100.48
NW-121	26.37	bdl	9.52	65.87	0.07	bdl	bdl	0.10	bdl	bdl	bdl	bdl	bdl	101.93
NW-121	26.05	bdl	9.26	63.97	0.06	bdl	bdl	0.09	bdl	bdl	bdl	bdl	bdl	99.44
NW-121	26.10	bdl	8.78	66.47	0.06	bdl	bdl	0.11	bdl	bdl	bdl	bdl	0.01	101.53
NW-121	26.46	bdl	10.01	64.52	0.13	bdl	bdl	0.04	bdl	bdl	0.02	bdl	bdl	101.18
NW-121	26.43	bdl	11.69	62.01	0.05	bdl	0.01	0.04	bdl	bdl	bdl	bdl	bdl	100.23
NW-121	26.71	bdl	11.76	60.92	0.15	bdl	bdl	0.03	bdl	bdl	bdl	bdl	bdl	99.57
NW140-6	25.93	bdl	8.84	63.80	0.10	bdl	bdl	0.02	bdl	bdl	bdl	bdl	bdl	98.68
NW140-6	25.99	bdl	9.00	65.35	0.08	bdl	bdl	0.01	bdl	bdl	0.02	bdl	bdl	100.46
NW140-6	26.18	bdl	9.30	64.56	0.09	bdl	bdl	0.01	bdl	bdl	0.03	bdl	0.01	100.18
NW140-6	25.95	bdl	9.08	64.49	0.08	bdl	bdl	0.01	bdl	bdl	bdl	bdl	0.01	99.62
NW140-6	26.15	bdl	9.28	64.38	0.08	bdl	0.00	0.01	bdl	bdl	bdl	bdl	bdl	99.90
NW140-6	26.01	0.00	9.40	64.37	0.17	bdl	bdl	0.01	bdl	bdl	bdl	bdl	bdl	99.97
NW140-6	25.98	bdl	9.43	63.88	0.09	bdl	bdl	0.01	bdl	bdl	0.03	bdl	bdl	99.42
NW140-6	26.16	0.01	9.62	62.93	0.02	bdl	bdl	0.02	bdl	bdl	0.01	bdl	bdl	98.77
NW140-6	26.01	0.01	9.70	63.19	0.07	bdl	bdl	0.01	bdl	bdl	0.02	bdl	bdl	99.01
NW140-6	26.52	bdl	10.05	62.45	0.08	bdl	0.00	0.02	bdl	bdl	bdl	bdl	0.01	99.13
NW140-6	26.35	bdl	9.25	62.81	0.05	bdl	bdl	0.01	bdl	bdl	bdl	bdl	bdl	98.48
NW140-6	26.59	0.01	11.04	61.28	0.08	bdl	0.00	0.01	bdl	bdl	bdl	bdl	bdl	99.01

NW140-6	26.16	bdl	9.36	63.04	0.04	bdl	bdl	0.01	bdl	bdl	bdl	bdl	bdl	98.60
NW140-6	26.13	bdl	9.47	63.68	0.08	0.01	bdl	0.01	bdl	bdl	0.01	bdl	bdl	99.38
NW140-6	26.07	bdl	9.66	63.70	0.15	bdl	bdl	0.01	bdl	bdl	bdl	bdl	0.01	99.60
NW140-6	26.08	0.02	10.01	62.30	0.14	bdl	bdl	0.02	bdl	bdl	bdl	bdl	bdl	98.58
NW140-6	25.77	0.03	10.50	62.35	0.08	bdl	bdl	0.02	bdl	bdl	bdl	bdl	bdl	98.75
NW140-6	26.10	0.01	9.77	63.62	0.07	bdl	bdl	0.02	bdl	bdl	bdl	bdl	bdl	99.59
NW140-6	26.27	bdl	10.16	61.95	0.06	bdl	0.00	0.01	bdl	bdl	bdl	bdl	bdl	98.46
NW140-6	25.83	0.00	10.80	62.16	0.16	bdl	bdl	0.01	bdl	bdl	bdl	bdl	bdl	98.96
NW140-6	26.25	bdl	9.29	63.54	0.06	bdl	bdl	0.02	bdl	bdl	0.02	bdl	bdl	99.17
NW140-6	25.92	bdl	10.56	62.35	0.09	bdl	bdl	0.02	bdl	bdl	0.01	bdl	0.01	98.96
NW140-6	26.03	bdl	11.49	60.65	0.06	bdl	bdl	0.01	bdl	bdl	bdl	bdl	bdl	98.24
NW140-6	25.98	bdl	11.40	61.42	0.06	bdl	bdl	0.02	bdl	bdl	0.02	bdl	0.01	98.90
NW140-6	26.17	bdl	10.32	62.01	0.07	bdl	bdl	0.01	bdl	bdl	bdl	bdl	bdl	98.58
NW140-6	25.73	bdl	9.09	64.06	0.14	bdl	bdl	0.02	bdl	bdl	bdl	bdl	bdl	99.04
NW140-6	25.69	bdl	9.38	63.36	0.07	bdl	bdl	0.01	bdl	bdl	bdl	bdl	0.01	98.53
NW140-6	26.22	0.01	10.41	63.01	0.15	bdl	bdl	0.01	bdl	bdl	bdl	bdl	bdl	99.82
NW140-6	26.41	bdl	10.46	62.74	0.04	bdl	bdl	0.01	bdl	bdl	0.01	bdl	bdl	99.67
NW140-6	25.94	0.01	9.33	64.16	0.08	bdl	0.01	0.01	bdl	bdl	bdl	bdl	bdl	99.54
NW140-6	25.79	0.00	8.90	65.19	0.07	bdl	bdl	0.03	bdl	bdl	bdl	bdl	bdl	99.98
NW140-6	25.97	bdl	8.97	65.38	0.15	bdl	bdl	0.02	bdl	bdl	bdl	bdl	bdl	100.49
NW140-6	25.85	bdl	9.11	65.13	0.07	bdl	bdl	0.02	bdl	bdl	0.02	bdl	bdl	100.20
NW140-6	26.04	bdl	9.22	64.84	0.14	bdl	bdl	0.03	bdl	bdl	bdl	bdl	bdl	100.28
NW140-6	25.77	0.00	9.40	65.11	0.06	bdl	bdl	0.02	bdl	bdl	bdl	bdl	bdl	100.36
NW140-6	25.93	bdl	9.22	65.49	0.07	bdl	bdl	0.01	bdl	bdl	0.01	bdl	bdl	100.73
NW140-6	25.84	bdl	9.05	65.52	0.13	bdl	bdl	0.01	bdl	bdl	0.01	bdl	bdl	100.57
NW140-6	25.79	bdl	9.42	65.19	0.08	bdl	bdl	0.02	bdl	bdl	0.01	bdl	bdl	100.51
NW140-6	25.73	bdl	8.82	65.66	0.08	bdl	bdl	0.02	bdl	bdl	bdl	bdl	bdl	100.31
NW140-6	25.76	bdl	8.61	65.32	0.08	bdl	bdl	0.03	bdl	bdl	bdl	bdl	bdl	99.80
MP-666	25.09	bdl	8.32	67.12	0.12	bdl	bdl	0.05	bdl	bdl	bdl	bdl	bdl	100.70
MP-666	25.29	bdl	8.44	67.10	0.18	bdl	bdl	0.05	bdl	bdl	bdl	bdl	bdl	101.06
MP-666	25.26	bdl	8.57	66.80	0.08	bdl	bdl	0.02	bdl	bdl	bdl	bdl	bdl	100.73

MP-666	25.22	bdl	8.63	66.83	0.07	bdl	bdl	0.04	bdl	bdl	bdl	bdl	0.02	100.82
MP-666	25.09	bdl	7.98	67.76	0.05	bdl	bdl	0.06	bdl	bdl	0.02	bdl	bdl	100.96
MP-666	25.19	bdl	8.94	66.88	0.18	bdl	bdl	0.05	bdl	bdl	bdl	bdl	0.02	101.25
MP-666	25.40	bdl	9.03	65.88	0.07	bdl	bdl	0.04	bdl	bdl	bdl	bdl	bdl	100.42
MP-666	25.57	bdl	8.90	66.20	0.08	bdl	bdl	0.05	bdl	bdl	bdl	bdl	bdl	100.80
MP-666	25.29	bdl	8.36	66.94	0.15	bdl	bdl	0.04	bdl	bdl	bdl	bdl	bdl	100.78
MP-666	25.02	bdl	8.15	67.45	0.07	bdl	bdl	0.04	bdl	bdl	bdl	bdl	bdl	100.74
MP-666	24.97	bdl	7.97	68.31	0.04	bdl	bdl	0.05	bdl	bdl	bdl	bdl	bdl	101.34
MP-666	25.03	bdl	8.26	67.58	0.08	bdl	bdl	0.03	bdl	bdl	bdl	bdl	bdl	100.98
MP-666	25.77	bdl	9.83	64.83	0.09	bdl	0.00	0.03	bdl	bdl	bdl	bdl	0.01	100.56
MP-666	25.82	bdl	9.96	65.06	0.09	bdl	bdl	0.01	bdl	bdl	bdl	bdl	0.01	100.96
MP-666	25.65	bdl	9.93	64.93	0.08	bdl	bdl	0.01	bdl	bdl	0.01	bdl	bdl	100.61
MP-666	25.81	bdl	10.09	63.87	0.15	bdl	bdl	0.02	bdl	bdl	0.01	bdl	0.01	99.96
MP-666	25.86	bdl	10.58	63.91	0.09	bdl	bdl	0.03	bdl	bdl	0.03	bdl	bdl	100.51
MP-666	25.87	bdl	9.85	64.45	0.08	bdl	0.01	0.03	bdl	bdl	0.02	bdl	bdl	100.30
MP-666	25.55	bdl	8.70	67.06	0.09	bdl	bdl	0.01	bdl	bdl	bdl	bdl	bdl	101.40
MP-666	25.77	bdl	9.63	65.40	0.06	bdl	0.01	0.03	bdl	bdl	bdl	bdl	bdl	100.90
MP-666	25.58	bdl	9.08	66.35	0.06	bdl	bdl	0.02	bdl	bdl	bdl	bdl	bdl	101.09
MP-666	25.59	bdl	9.63	65.38	0.11	bdl	bdl	0.03	bdl	bdl	bdl	bdl	0.01	100.75
MP-666	25.86	bdl	10.55	64.15	0.17	bdl	0.00	0.02	bdl	bdl	0.01	bdl	0.02	100.78
MP-666	26.01	bdl	9.95	64.39	0.10	bdl	bdl	0.01	bdl	bdl	0.01	bdl	0.01	100.48
MP-666	25.73	bdl	10.28	63.62	0.08	bdl	bdl	0.02	bdl	bdl	bdl	bdl	bdl	99.73
MP-666	25.95	bdl	10.07	63.74	0.05	bdl	0.00	0.03	bdl	bdl	bdl	bdl	0.01	99.86
MP-666	25.91	bdl	9.13	64.73	0.06	bdl	bdl	0.00	bdl	bdl	bdl	bdl	bdl	99.84
MP-666	26.38	bdl	10.64	62.39	0.16	bdl	0.01	0.01	bdl	bdl	0.04	bdl	bdl	99.62
MP-666	25.79	bdl	10.49	63.18	0.06	bdl	bdl	0.01	bdl	bdl	bdl	bdl	bdl	99.52
MP-666	26.02	bdl	8.84	65.07	0.05	bdl	bdl	0.00	bdl	bdl	bdl	bdl	bdl	99.99
MP-666	26.28	bdl	10.17	62.49	0.05	bdl	bdl	0.01	bdl	bdl	bdl	bdl	0.01	99.01
MP-666	25.83	bdl	8.96	65.41	0.07	bdl	0.00	0.01	bdl	bdl	bdl	bdl	bdl	100.28
MP-666	25.67	bdl	11.22	63.84	0.13	bdl	bdl	0.03	bdl	bdl	bdl	bdl	bdl	100.90
MP-666	25.78	0.01	10.63	63.66	0.16	bdl	bdl	0.01	bdl	bdl	bdl	bdl	0.01	100.26

MP-666	25.78	0.02	10.49	63.42	0.11	bdl	0.01	0.02	bdl	bdl	bdl	bdl	bdl	99.85

	Estadística													
	S	**Mn**	**Fe**	**Cu**	**Zn**	**As**	**Se**	**Ag**	**Sb**	**Te**	**Au**	**Pb**	**Bi**	**Total**
Mínimo	24.97	0.004	7.97	56.17	0.009	0.004	0.002	0.002	0.003	0.004	0.003	0.009	0.005	98.24
Máximo	29.30	0.095	15.49	68.31	0.191	0.374	0.010	0.166	0.007	0.005	0.040	0.234	0.024	101.93
Mediana	26.35	0.011	10.41	62.93	0.079	0.005	0.005	0.024	0.004	0.005	0.015	0.189	0.009	100.04
Promedio	26.42	0.021	10.47	62.92	0.086	0.031	0.005	0.034	0.004	0.005	0.017	0.160	0.011	99.96
Sobre l.d.	149	21	149	149	126	15	22	148	6	2	50	15	41	149

C.4. Calcosina

Anexo equivalente a *Appendix B-Chalcocite* indicado en el manuscrito del Capítulo 2. Las concentraciones se muestran en porcentaje en peso (wt.%). “bdl” indica los valores que se encuentran bajo el límite de detección, el cual se puede identificar debajo de cada uno de los elementos analizados.

	S 0.0070	**Fe** 0.0386	**Co** 0.0377	**Ni** 0.0316	**Cu** 0.0255	**As** 0.0240	**Se** 0.0240	**Ag** 0.0155	**Sb** 0.0240	**Pb** 0.1092	**Total**
MP-666	20.09	0.70	0.05	bdl	79.23	bdl	bdl	0.08	0.08	bdl	100.22
MP-666	20.41	0.71	bdl	0.06	79.52	bdl	bdl	0.11	bdl	bdl	100.84
MP-666	20.58	0.78	bdl	bdl	79.52	bdl	0.05	0.07	bdl	bdl	101.06
MP-666	19.83	0.64	bdl	bdl	79.94	bdl	bdl	0.05	bdl	bdl	100.50
MP-666	20.47	0.59	bdl	bdl	80.33	bdl	bdl	0.09	bdl	bdl	101.52
MP-666	20.45	0.46	0.05	bdl	79.98	bdl	bdl	0.10	bdl	bdl	101.07
MP-666	20.43	0.45	bdl	bdl	79.85	0.03	bdl	0.06	bdl	bdl	100.84
MP-666	20.50	0.76	bdl	bdl	79.43	bdl	bdl	0.09	bdl	bdl	100.85
MP-666	20.18	0.69	bdl	bdl	79.65	bdl	bdl	0.09	bdl	bdl	100.62
MP-666	20.45	0.45	bdl	bdl	78.67	bdl	bdl	0.08	bdl	bdl	99.75
MP-666	20.65	0.41	bdl	bdl	79.53	bdl	bdl	0.08	bdl	bdl	100.71
MP-666	20.58	0.73	bdl	bdl	79.42	bdl	bdl	0.08	0.08	bdl	100.92
MP-666	20.55	0.45	bdl	bdl	78.85	0.03	bdl	0.02	0.05	bdl	99.98
MP-666	20.97	0.41	bdl	bdl	79.41	bdl	bdl	0.11	bdl	bdl	100.89
MP-666	22.29	2.58	0.06	bdl	74.52	bdl	bdl	0.09	bdl	0.33	99.86
MP-666	22.43	2.87	bdl	bdl	75.18	bdl	bdl	0.06	bdl	bdl	100.56
MP-666	20.89	0.72	bdl	bdl	78.91	bdl	0.04	0.11	bdl	bdl	100.67
MP-666	21.19	0.57	bdl	bdl	79.28	bdl	bdl	0.09	bdl	bdl	101.15
MP-666	21.03	0.95	bdl	bdl	78.90	bdl	bdl	0.13	bdl	0.28	101.32
MP-666	20.68	1.14	bdl	bdl	79.27	0.03	bdl	0.06	bdl	bdl	101.22
MP-666	20.70	1.34	bdl	bdl	78.72	bdl	bdl	0.08	0.05	bdl	100.90
MP-666	20.68	1.15	bdl	bdl	79.82	bdl	bdl	0.08	0.05	bdl	101.81
MP-666	22.59	4.41	bdl	bdl	74.43	bdl	bdl	0.06	0.04	bdl	101.55

	Estadística										
	S	**Fe**	**Co**	**Ni**	**Cu**	**As**	**Se**	**Ag**	**Sb**	**Pb**	**Total**
Mínimo	19.83	0.406	0.048	0.063	74.43	0.031	0.043	0.018	0.036	0.284	99.75
Máximo	22.59	4.406	0.063	0.063	80.33	0.033	0.047	0.126	0.082	0.332	101.81
Mediana	20.58	0.705	0.052	0.063	79.41	0.031	0.045	0.081	0.049	0.308	100.85
Promedio	20.81	1.041	0.054	0.063	78.80	0.032	0.045	0.080	0.057	0.308	100.82
Sobre l.d.	23	23	3	1	23	3	2	23	6	2	23

C.5. Bitumen

Anexo equivalente a *Appendix B-Bitumen* indicado en el manuscrito del Capítulo 2. Las concentraciones se muestran en porcentaje en peso (wt.%). "bdl" indica los valores que se encuentran bajo el límite de detección, el cual se puede identificar debajo de cada uno de los elementos analizados.

	C 0.1254	**O** 0.0114	**P** 0.0020	**S** 0.0014	**Ca** 0.0026	**Cr** 0.0021	**Mn** 0.0046	**Fe** 0.0040	**Co** 0.0022	**Cu** 0.0102	**Zn** 0.0040	**As** 0.0038	**Mo** 0.0040	**Ag** 0.0143	**Sb** 0.0101	**Total**
NW140-6	93.80	2.74	bdl	0.79	0.02	bdl	0.02	0.19	bdl	0.04	0.00	bdl	bdl	0.04	bdl	97.65
NW140-6	93.27	3.31	bdl	0.78	0.03	bdl	0.03	0.34	bdl	0.01	bdl	bdl	bdl	0.06	bdl	97.84
NW140-6	95.03	2.48	0.00	0.76	0.01	bdl	bdl	0.14	bdl	bdl	bdl	bdl	bdl	bdl	bdl	98.44
NW140-6	95.22	2.35	bdl	0.77	0.01	bdl	0.00	0.14	bdl	0.03	bdl	bdl	bdl	bdl	0.02	98.54
NW140-6	95.22	2.37	bdl	0.77	0.01	bdl	bdl	0.15	bdl	0.02	bdl	bdl	bdl	0.03	bdl	98.58
NW140-6	95.19	2.35	0.00	0.75	0.01	bdl	0.01	0.20	bdl	0.04	bdl	bdl	bdl	bdl	0.01	98.58
NW140-6	94.34	3.16	bdl	0.72	0.05	bdl	bdl	0.08	bdl	0.01	bdl	bdl	bdl	bdl	bdl	98.37
NW140-6	94.41	3.22	bdl	0.73	0.05	0.00	bdl	0.11	bdl	bdl	bdl	bdl	bdl	0.01	bdl	98.54
NW140-6	93.15	4.21	bdl	0.80	0.06	bdl	0.01	0.06	bdl	0.02	bdl	bdl	0.01	0.02	bdl	98.33
NW140-6	92.94	4.28	bdl	0.77	0.06	bdl	bdl	0.08	bdl	0.04	bdl	bdl	bdl	bdl	bdl	98.17
NW140-6	95.51	2.74	0.00	0.72	0.04	bdl	0.01	0.10	bdl	0.02	bdl	bdl	0.01	0.02	bdl	99.17
NW140-6	95.37	2.63	0.00	0.73	0.04	0.01	0.01	0.11	bdl	0.03	bdl	bdl	bdl	0.02	bdl	98.95
NW140-6	94.82	3.13	bdl	0.69	0.05	0.01	0.01	0.11	bdl	0.02	bdl	bdl	bdl	0.03	0.01	98.88
NW140-6	91.05	5.21	bdl	0.79	0.02	bdl	bdl	0.06	0.01	0.03	bdl	bdl	bdl	0.03	bdl	97.20
NW140-6	91.13	4.98	bdl	0.79	0.03	bdl	bdl	0.05	bdl	0.04	bdl	bdl	bdl	bdl	bdl	97.03
NW140-6	94.91	2.75	bdl	0.79	0.04	bdl	0.01	0.20	0.00	bdl	bdl	bdl	bdl	0.03	bdl	98.73
NW140-6	94.62	2.84	bdl	0.84	0.11	0.00	0.01	0.19	bdl	bdl	bdl	bdl	bdl	0.04	bdl	98.65
NW140-6	94.27	3.08	bdl	0.85	0.09	bdl	0.01	0.16	0.00	0.01	bdl	bdl	bdl	0.03	0.01	98.52
NW140-6	94.02	2.98	bdl	0.82	0.05	bdl	0.02	0.17	0.00	0.02	bdl	bdl	bdl	0.01	bdl	98.10
NW140-6	92.69	4.07	bdl	0.77	0.01	bdl	0.01	0.17	bdl	bdl	bdl	bdl	bdl	bdl	bdl	97.72
NW140-6	93.80	3.14	0.00	0.81	0.08	bdl	0.00	0.11	bdl	0.02	bdl	bdl	bdl	0.02	0.03	98.01

	Estadística															
	C	**O**	**P**	**S**	**Ca**	**Cr**	**Mn**	**Fe**	**Co**	**Cu**	**Zn**	**As**	**Mo**	**Ag**	**Sb**	**Total**
Mínimo	91.05	2.35	0.002	0.694	0.009	0.003	0.005	0.052	0.003	0.012	0.005	-	0.006	0.013	0.011	97.03
Máximo	95.51	5.21	0.003	0.850	0.107	0.006	0.030	0.339	0.006	0.038	0.005	-	0.009	0.065	0.031	99.17
Mediana	94.34	3.08	0.002	0.772	0.042	0.005	0.008	0.137	0.004	0.023	0.005	-	0.007	0.026	0.012	98.44
Promedio	94.04	3.24	0.002	0.774	0.041	0.005	0.010	0.139	0.004	0.025	0.005	-	0.007	0.027	0.017	98.28
Sobre l.d.	21	21	5	21	21	4	14	21	4	16	1	-	2	14	5	21

ANEXO D: Resultados LA-ICP-MS

D.1. Pirita

Anexo equivalente a *Appendix C-Pyrite* indicado en el manuscrito del Capítulo 2. Las concentraciones se muestran en porcentaje en peso (ppm). “bdl” indica los valores que se encuentran bajo el límite de detección, el cual se puede identificar debajo de cada uno de los elementos analizados.

	V 4.2	**Cr** 1.8	**Mn** 5.2	**Co** 4.9	**Ni** 9.1	**Cu** 5.7	**Zn** 13.5	**Ga** 1.8	**Ge** 4.6	**As** 9.0	**Se** 13.3	**Mo** 2.8	**Ag** 1.3	**Cd** 3.4	**In** 0.1	**Sn** 0.6	**Sb** 1.8	**Te** 5.4	**Pt** 0.0	**Au** 0.1	**Hg** 0.7	**Tl** 0.3	**Pb** 0.2	**Bi** 0.1
NW-24	bdl	9.3	24.3	227.0	1000.0	317.0	bdl	bdl	6.5	7900.0	20.0	15.3	7.0	bdl	bdl	bdl	10.7	bdl	bdl	bdl	bdl	678.0	47.0	bdl
NW-24	bdl	19.0	20.0	bdl	bdl	bdl	bdl	bdl	15.1	3260.0	65.0	10.0	bdl	bdl	bdl	bdl	bdl	bdl	bdl	bdl	bdl	76.5	1.3	bdl
NW-2	bdl	bdl	bdl	bdl	bdl	2340.0	193.0	bdl	bdl	bdl	bdl	bdl	7.2	bdl	7.6	24.4	bdl	bdl	bdl	bdl	bdl	bdl	61.0	bdl
NW-2	bdl	bdl	9.6	bdl	bdl	800.0	83.0	bdl	bdl	24.0	bdl	bdl	4.7	4.4	6.3	14.9	11.3	bdl	bdl	bdl	bdl	bdl	107.0	bdl
NW-2	bdl	bdl	bdl	bdl	bdl	368.0	121.0	bdl	bdl	51.0	bdl	bdl	bdl	6.9	7.4	20.7	bdl	bdl	bdl	0.0	bdl	bdl	190.0	bdl
NW-2	9.0	7.1	11.8	bdl	bdl	301.0	138.0	bdl	bdl	bdl	bdl	bdl	bdl	bdl	7.9	22.8	bdl	bdl	bdl	bdl	bdl	bdl	8.3	bdl
NW-2	bdl	15.6	bdl	11.0	bdl	760.0	80.0	bdl	bdl	24.0	bdl	bdl	3.5	bdl	7.6	16.1	9.9	bdl	bdl	bdl	bdl	bdl	760.0	0.5
NW-2	bdl	bdl	183.0	58.7	231.0	109.9	bdl	1.5	bdl	2410.0	bdl	13.2	5.6	bdl	bdl	bdl	15.1	bdl	bdl	0.0	bdl	47.6	47.6	0.6
NW-2	bdl	3.1	360.0	78.7	205.0	107.6	bdl	bdl	bdl	1291.0	bdl	18.0	6.6	bdl	bdl	bdl	14.2	bdl	bdl	0.1	0.3	30.5	67.6	0.7
NW-2	bdl	bdl	9.1	138.0	188.0	62.1	bdl	bdl	bdl	5420.0	bdl	2.5	5.0	bdl	bdl	bdl	19.9	bdl	bdl	0.0	bdl	42.6	73.6	0.5
NW-2	bdl	1.7	218.0	82.6	251.0	110.8	bdl	bdl	4.8	2150.0	42.0	7.8	5.4	1.1	0.1	bdl	17.3	bdl	bdl	bdl	bdl	51.8	61.5	0.7
NW-2	bdl	bdl	610.0	165.0	116.0	87.1	bdl	bdl	bdl	914.0	56.0	26.4	4.7	bdl	bdl	bdl	18.5	6.6	bdl	0.1	bdl	32.3	62.6	0.7
NW-2	bdl	bdl	23.0	103.0	342.0	157.0	bdl	bdl	5.8	156.0	bdl	4.5	4.5	bdl	bdl	bdl	5.9	bdl	bdl	bdl	0.7	187.0	71.2	bdl
NW-2	bdl	bdl	40.0	133.0	500.0	2950.0	bdl	bdl	6.1	291.0	bdl	59.0	7.1	bdl	bdl	bdl	bdl	bdl	bdl	bdl	1.0	12.7	55.4	0.3
NW-2	bdl	bdl	1740.0	130.0	148.0	163.0	22.0	bdl	3.0	188.0	bdl	10.3	3.2	bdl	bdl	bdl	6.3	bdl	bdl	0.0	0.6	14.2	47.1	0.3
NW-2	bdl	bdl	1460.0	285.0	440.0	1360.0	12.8	0.9	2.2	488.0	bdl	38.7	5.9	bdl	bdl	bdl	21.0	bdl	bdl	bdl	bdl	39.3	67.8	0.4
NW-24	bdl	1.3	894.0	bdl	bdl	63.5	12.2	bdl	bdl	1680.0	bdl	35.0	0.8	bdl	bdl	bdl	bdl	10.2	bdl	bdl	bdl	bdl	8.8	bdl

NW-24	bdl	bdl	2800.0	bdl	bdl	127.1	27.5	bdl	4.3	4940.0	bdl	61.9	1.3	bdl	bdl	bdl	bdl	8.9	bdl	bdl	bdl	bdl	2.6	bdl
NW-24	bdl	bdl	3080.0	bdl	6.8	202.0	47.3	bdl	3.1	3480.0	12.0	54.7	5.7	bdl	bdl	bdl	bdl	bdl	bdl	bdl	0.6	bdl	9.4	bdl
NW-24	bdl	bdl	43.9	bdl	bdl	244.0	17.8	bdl	4.0	1246.0	11.0	14.4	3.7	bdl	bdl	bdl	bdl	bdl	bdl	bdl	1.5	bdl	19.1	bdl
NW-24	bdl	2.6	32.9	45.0	bdl	454.0	bdl	bdl	bdl	1660.0	bdl	19.3	7.3	bdl	bdl	bdl	bdl	bdl	bdl	0.0	bdl	bdl	139.0	bdl
NW-24	bdl	bdl	3100.0	36.9	bdl	660.0	44.0	bdl	bdl	4100.0	bdl	50.5	8.9	bdl	bdl	bdl	bdl	bdl	bdl	0.0	1.7	bdl	162.0	bdl

	Estadística																							
	V	**Cr**	**Mn**	**Co**	**Ni**	**Cu**	**Zn**	**Ga**	**Ge**	**As**	**Se**	**Mo**	**Ag**	**Cd**	**In**	**Sn**	**Sb**	**Te**	**Pt**	**Au**	**Hg**	**Tl**	**Pb**	**Bi**
Mínimo	9	1.3	9.1	11.0	6.8	62.1	12.2	0.9	2.2	24.0	11.0	2.5	0.8	1.1	0.1	14.9	5.9	6.6	-	0.0	0.3	12.7	1.3	0.3
Máximo	9	19.0	3100.0	285.0	1000.0	2950.0	193.0	1.5	15.1	7900.0	65.0	61.9	8.9	6.9	7.9	24.4	21.0	10.2	-	0.1	1.7	678.0	760.0	0.7
Mediana	9	5.1	183.0	103.0	231.0	244.0	45.7	1.2	4.6	1475.5	31.0	18.0	5.4	4.4	7.5	20.7	14.2	8.9	-	0.0	0.7	42.6	61.3	0.5
Promedio	9	7.5	771.6	114.9	311.6	559.2	66.6	1.2	5.5	2083.7	34.3	26.0	5.2	4.1	6.1	19.8	13.6	8.6	-	0.0	0.9	110.2	94.1	0.5
Sobre l.d.	1	8	19	13	11	21	12	2	10	20	6	17	19	3	6	5	11	3	-	8	7	11	22	9

D.2. Calcopirita

Anexo equivalente a *Appendix C-Chalcopyrite* indicado en el manuscrito del Capítulo 2. Las concentraciones se muestran en porcentaje en peso (ppm). “bdl” indica los valores que se encuentran bajo el límite de detección, el cual se puede identificar debajo de cada uno de los elementos analizados.

	V	**Cr**	**Mn**	**Co**	**Ni**	**Zn**	**Ga**	**Ge**	**As**	**Se**	**Mo**	**Ag**	**Cd**	**In**	**Sn**	**Sb**	**Te**	**Pt**	**Au**	**Hg**	**Tl**	**Pb**	**Bi**
	25.7	15.2	37.3	24.7	61.9	110.6	14.8	27.2	58.8	100.8	17.9	9.3	26.4	0.6	3.8	8.5	29.1	0.0	0.0	7.1	1.8	1.1	0.8
NW-2	bdl	bdl	bdl	bdl	bdl	270.0	bdl	bdl	bdl	bdl	bdl	bdl	bdl	8.0	22.5	bdl	4.1	bdl	bdl	bdl	bdl	bdl	bdl
NW-2	bdl	bdl	bdl	bdl	bdl	bdl	bdl	bdl	bdl	bdl	bdl	bdl	bdl	7.3	18.1	bdl	bdl	bdl	bdl	bdl	0.4	bdl	bdl
NW-2	bdl	bdl	bdl	bdl	bdl	248.0	bdl	bdl	bdl	bdl	bdl	4.5	bdl	7.7	23.7	bdl	bdl	bdl	bdl	bdl	bdl	3.5	bdl
NW-2	bdl	bdl	28.0	bdl	bdl	100.0	bdl	bdl	bdl	bdl	bdl	bdl	bdl	6.9	16.7	bdl	bdl	bdl	bdl	bdl	bdl	8.2	bdl
NW-2	bdl	bdl	26.0	bdl	bdl	107.0	bdl	14.6	bdl	bdl	bdl	bdl	bdl	6.5	12.8	bdl	bdl	bdl	0.0	bdl	bdl	4.6	bdl
MP-893	bdl	125.0	bdl	bdl	bdl	bdl	bdl	bdl	bdl	bdl	bdl	bdl	bdl	9.8	bdl	bdl	bdl	bdl	bdl	bdl	bdl	259.0	bdl
MP-893	bdl	220.0	bdl	bdl	bdl	bdl	bdl	70.0	bdl	bdl	bdl	23.0	bdl	7.5	bdl	bdl	bdl	bdl	bdl	bdl	bdl	490.0	bdl
MP-893	56.0	76.0	bdl	bdl	bdl	bdl	bdl	bdl	bdl	bdl	bdl	23.0	bdl	9.0	9.3	bdl	bdl	bdl	bdl	bdl	bdl	75.0	bdl
MP-893	50.0	58.0	bdl	bdl	bdl	bdl	bdl	bdl	bdl	bdl	bdl	17.0	bdl	8.1	15.4	26.0	bdl	bdl	bdl	bdl	bdl	bdl	bdl
MP-893	62.0	bdl	bdl	64.0	bdl	bdl	bdl	bdl	130.0	14000.0	bdl	16.0	bdl	bdl	23.6	bdl	bdl	bdl	bdl	bdl	bdl	bdl	bdl
MP-893	bdl	66.0	bdl	bdl	bdl	bdl	bdl	bdl	bdl	5100.0	bdl	20.0	bdl	bdl	15.3	bdl	bdl	bdl	0.8	9.3	bdl	bdl	bdl
MP-893	bdl	bdl	bdl	100.0	bdl	bdl	bdl	bdl	bdl	500.0	5.0	22.0	bdl	bdl	14.3	bdl	bdl	bdl	bdl	bdl	bdl	bdl	bdl
MP-893	80.0	bdl	bdl	45.0	bdl	bdl	bdl	bdl	bdl	2200.0	bdl	bdl	bdl	bdl	9.6	bdl	bdl	bdl	bdl	bdl	bdl	12.7	bdl
MP-893	28.0	bdl	bdl	bdl	59.0	bdl	bdl	bdl	bdl	1700.0	bdl	bdl	3.5	6.9	13.3	bdl	bdl	bdl	bdl	bdl	bdl	bdl	bdl
MP-893	25.0	bdl	bdl	bdl	bdl	bdl	bdl	bdl	bdl	100.0	bdl	bdl	bdl	7.9	16.4	bdl	bdl	bdl	bdl	bdl	bdl	12.9	bdl
MP-893	bdl	bdl	bdl	bdl	bdl	bdl	bdl	bdl	72.0	1100.0	2.7	bdl	7.0	6.4	16.6	11.3	bdl	bdl	bdl	bdl	bdl	4.8	bdl
MP-893	bdl	bdl	bdl	bdl	bdl	bdl	bdl	bdl	bdl	bdl	bdl	bdl	bdl	5.7	12.9	18.6	bdl	bdl	bdl	bdl	bdl	94.0	bdl
MP-893	bdl	bdl	bdl	bdl	bdl	bdl	bdl	bdl	bdl	bdl	bdl	bdl	bdl	5.5	18.8	bdl	bdl	bdl	bdl	bdl	bdl	7.2	0.2
MP-893	bdl	45.0	57.0	bdl	bdl	bdl	bdl	bdl	bdl	bdl	bdl	bdl	bdl	5.7	13.8	bdl	bdl	bdl	0.1	bdl	bdl	4.2	bdl
MP-893	bdl	bdl	36.0	bdl	bdl	bdl	9.6	bdl	bdl	bdl	bdl	bdl	bdl	4.2	14.6	bdl	bdl	bdl	bdl	bdl	bdl	4.4	bdl
MP-893	bdl	90.0	bdl	140.0	bdl	bdl	bdl	bdl	bdl	1100.0	bdl	bdl	bdl	6.5	bdl	bdl	bdl	bdl	bdl	bdl	bdl	8.9	bdl
MP-893	bdl	bdl	127.0	bdl	bdl	bdl	bdl	bdl	bdl	1100.0	18.0	bdl	bdl	8.8	16.5	bdl	bdl	bdl	bdl	bdl	bdl	24.9	bdl

MP-893	bdl	bdl	bdl	bdl	bdl	bdl	bdl	bdl	bdl	bdl	bdl	bdl	bdl	7.5	15.6	bdl	bdl	bdl	0.3	bdl	bdl	7.1	bdl
MP-893	bdl	bdl	bdl	bdl	bdl	bdl	bdl	bdl	bdl	bdl	bdl	bdl	bdl	5.4	9.4	bdl	bdl	bdl	bdl	bdl	bdl	57.0	bdl
MP-893	bdl	29.0	bdl	bdl	bdl	bdl	bdl	bdl	bdl	bdl	bdl	bdl	bdl	6.8	8.5	bdl	bdl	bdl	bdl	bdl	bdl	8.0	bdl
MP-893	bdl	35.0	190.0	bdl	bdl	bdl	bdl	bdl	bdl	340.0	bdl	bdl	bdl	4.7	9.3	bdl	23.0	bdl	bdl	bdl	bdl	166.0	bdl
NW-121	25.0	bdl	bdl	bdl	bdl	bdl	bdl	bdl	bdl	bdl	bdl	bdl	bdl	6.6	bdl	bdl	bdl	0.3	bdl	bdl	bdl	0.1	bdl
NW-121	bdl	bdl	bdl	bdl	bdl	bdl	bdl	bdl	bdl	bdl	bdl	bdl	bdl	7.3	bdl	bdl	bdl	bdl	bdl	bdl	bdl	bdl	bdl
NW-121	bdl	bdl	bdl	bdl	bdl	bdl	bdl	bdl	bdl	800.0	bdl	bdl	bdl	6.7	bdl	bdl	1.7	bdl	bdl	bdl	bdl	bdl	bdl
NW-121	bdl	bdl	bdl	bdl	bdl	bdl	bdl	bdl	bdl	500.0	bdl	6.2	bdl	7.0	bdl	bdl	bdl	bdl	0.0	bdl	bdl	1.1	bdl
NW-121	bdl	bdl	bdl	bdl	bdl	bdl	bdl	bdl	bdl	260.0	bdl	bdl	bdl	7.1	bdl	bdl	bdl	bdl	0.1	bdl	bdl	0.8	bdl
NW-121	26.0	bdl	bdl	bdl	bdl	bdl	bdl	bdl	bdl	bdl	bdl	bdl	bdl	8.3	bdl	bdl	bdl	bdl	0.2	bdl	bdl	15.3	bdl
NW-121	20.0	18.0	bdl	bdl	33.0	bdl	bdl	bdl	bdl	bdl	bdl	bdl	bdl	8.7	bdl	bdl	bdl	bdl	bdl	bdl	0.1	5.6	bdl
NW-121	bdl	bdl	bdl	bdl	bdl	bdl	bdl	bdl	bdl	bdl	bdl	bdl	bdl	7.9	bdl	bdl	bdl	bdl	bdl	bdl	0.1	bdl	bdl
MP-699	bdl	bdl	307.0	bdl	bdl	bdl	bdl	bdl	bdl	bdl	bdl	12.0	bdl	2.7	bdl	bdl	bdl	bdl	bdl	bdl	bdl	49.9	1.4
MP-699	bdl	bdl	2540.0	bdl	bdl	bdl	bdl	29.0	bdl	bdl	bdl	22.1	bdl	2.1	bdl	bdl	bdl	bdl	0.1	bdl	bdl	113.0	6.4
MP-699	bdl	16.0	1210.0	26.0	bdl	bdl	bdl	bdl	bdl	bdl	bdl	17.2	bdl	2.9	bdl	bdl	bdl	bdl	0.2	7.9	bdl	156.0	4.5
MP-699	bdl	bdl	132.0	14.0	bdl	bdl	bdl	bdl	bdl	89.0	2.0	15.7	bdl	3.0	bdl	10.3	bdl	bdl	bdl	bdl	bdl	143.0	6.5
MP-699	bdl	bdl	1220.0	bdl	bdl	bdl	bdl	bdl	bdl	bdl	bdl	bdl	bdl	3.2	bdl	bdl	4.1	bdl	bdl	bdl	bdl	96.0	3.2
MP-699	bdl	36.0	bdl	bdl	bdl	bdl	bdl	bdl	bdl	bdl	bdl	bdl	15.0	3.6	bdl	bdl	3.3	bdl	bdl	bdl	bdl	9.9	bdl
MP-699	bdl	bdl	2030.0	19.0	bdl	bdl	bdl	bdl	bdl	bdl	bdl	8.2	1.0	3.2	bdl	11.3	bdl	bb	bdl	bdl	bdl	133.0	3.7

	Estadística																						
	V	**Cr**	**Mn**	**Co**	**Ni**	**Zn**	**Ga**	**Ge**	**As**	**Se**	**Mo**	**Ag**	**Cd**	**In**	**Sn**	**Sb**	**Te**	**Pt**	**Au**	**Hg**	**Tl**	**Pb**	**Bi**
Mínimo	20.0	16.0	26.0	14.0	33.0	100.0	9.6	14.6	72.0	89.0	2.0	4.5	1.0	2.1	8.5	10.3	1.7	0.3	0.0	7.9	0.1	0.1	0.2
Máximo	80.0	220.0	2540.0	140.0	59.0	270.0	9.6	70.0	130.0	14000.0	18.0	23.0	15.0	9.8	23.7	26.0	23.0	0.3	0.8	9.3	0.4	490.0	6.5
Mediana	28.0	51.5	161.0	45.0	46.0	177.5	9.6	29.0	101.0	950.0	3.9	17.0	5.3	6.8	15.3	11.3	4.1	0.3	0.1	8.6	0.1	12.7	3.7
Promedio	41.3	67.8	658.6	58.3	46.0	181.3	9.6	37.9	101.0	2063.5	6.9	15.9	6.6	6.3	15.1	15.5	7.2	0.3	0.2	8.6	0.2	63.7	3.7
Sobre l.d.	9	12	12	7	2	4	1	3	2	14	4	13	4	37	23	5	5	1	9	2	3	31	7

D.3. Bornita

Anexo equivalente a *Appendix C-Bornite* indicado en el manuscrito del Capítulo 2. Las concentraciones se muestran en porcentaje en peso (ppm). “bdl” indica los valores que se encuentran bajo el límite de detección, el cual se puede identificar debajo de cada uno de los elementos analizados.

	V 17.2	**Cr** 9.4	**Mn** 30.2	**Co** 16.5	**Ni** 37.5	**Zn** 79.5	**Ga** 9.9	**Ge** 18.3	**As** 41.9	**Se** 68.0	**Mo** 11.4	**Ag** 6.6	**Cd** 21.2	**In** 0.5	**Sn** 3.2	**Sb** 5.8	**Te** 9.1	**Pt** 0.0	**Au** 0.2	**Hg** 6.6	**Tl** 1.2	**Pb** 1.3	**Bi** 0.5
MP-893	28.0	21.0	276.0	bdl	bdl	bdl	bdl	bdl	bdl	bdl	bdl	138	bdl	bdl	bdl	bdl	bdl	bdl	0.0	bdl	bdl	29.2	13.6
MP-893	34.0	bdl	bdl	bdl	bdl	48.0	bdl	bdl	bdl	bdl	bdl	115.0	bdl	bdl	bdl	bdl	bdl	bdl	bdl	bdl	bdl	24.8	10.3
MP-893	bdl	bdl	bdl	bdl	bdl	bdl	bdl	bdl	bdl	bdl	bdl	92.0	bdl	bdl	bdl	bdl	bdl	bdl	bdl	bdl	bdl	11.7	8.6
MP-893	24.0	bdl	bdl	bdl	bdl	bdl	bdl	bdl	bdl	bdl	bdl	159.0	bdl	bdl	bdl	bdl	bdl	bdl	bdl	bdl	bdl	10.7	15.7
MP-893	39.0	15.0	bdl	bdl	bdl	bdl	bdl	bdl	80.0	bdl	7.8	106.0	bdl	bdl	bdl	bdl	bdl	bdl	0.2	bdl	bdl	14.9	14.4
MP-893	bdl	bdl	bdl	bdl	bdl	bdl	bdl	bdl	bdl	bdl	bdl	132.0	bdl	bdl	bdl	bdl	bdl	bdl	bdl	bdl	bdl	121.0	18.7
MP-893	bdl	14.0	bdl	bdl	bdl	bdl	bdl	bdl	bdl	100.0	bdl	190.0	bdl	bdl	bdl	bdl	bdl	bdl	bdl	bdl	bdl	50.0	16.5
MP-893	bdl	101.0	bdl	bdl	140.0	bdl	bdl	bdl	bdl	bdl	5.0	386.0	12.0	bdl	bdl	bdl	bdl	bdl	bdl	bdl	6.5	bdl	28.7
MP-893	bdl	29.0	bdl	bdl	69.0	bdl	bdl	bdl	bdl	6800.0	bdl	377.0	bdl	bdl	bdl	bdl	bdl	bdl	bdl	bdl	bdl	bdl	25.4
MP-893	bdl	55.0	bdl	bdl	bdl	bdl	bdl	bdl	bdl	bdl	bdl	264.0	bdl	bdl	bdl	bdl	bdl	bdl	bdl	bdl	bdl	bdl	22.9
MP-893	30.0	63.0	bdl	bdl	bdl	bdl	bdl	bdl	bdl	90000	bdl	253.0	bdl	bdl	bdl	bdl	6.0	bdl	0.0	bdl	bdl	bdl	19.5
MP-893	bdl	27.0	bdl	bdl	bdl	bdl	bdl	bdl	bdl	bdl	bdl	318.0	bdl	bdl	bdl	bdl	bdl	bdl	bdl	bdl	bdl	55.0	25.1
MP-893	bdl	bdl	bdl	bdl	bdl	bdl	bdl	bdl	37.0	750.0	bdl	260.0	3.7	bdl	bdl	bdl	bdl	bdl	bdl	bdl	bdl	3.4	14.1
MP-893	bdl	bdl	bdl	94.0	bdl	bdl	43.0	bdl	bdl	bdl	bdl	242.0	bdl	bdl	bdl	bdl	bdl	bdl	bdl	bdl	bdl	75.0	20.9
MP-893	bdl	47.0	199.0	bdl	bdl	bdl	bdl	bdl	bdl	bdl	bdl	460.0	bdl	bdl	bdl	bdl	bdl	bdl	bdl	bdl	bdl	187.0	13.1
MP-893	45.0	bdl	49.0	bdl	bdl	bdl	bdl	bdl	bdl	bdl	bdl	115.0	bdl	bdl	10.0	bdl	bdl	bdl	bdl	bdl	3.8	322.0	19.5
NW140-6	bdl	bdl	42.0	6.8	bdl	bdl	bdl	bdl	bdl	bdl	7.1	47.9	bdl	0.2	bdl	bdl	bdl	bdl	bdl	bdl	2.0	65.0	6.0
NW140-6	bdl	bdl	bdl	bdl	bdl	bdl	bdl	bdl	bdl	bdl	bdl	66.0	bdl	bdl	bdl	bdl	bdl	bdl	bdl	bdl	2.0	86.0	4.9
NW140-6	bdl	bdl	41.8	bdl	bdl	bdl	bdl	bdl	bdl	bdl	bdl	54.0	bdl	0.4	bdl	bdl	bdl	bdl	bdl	bdl	7.9	238.0	5.5
NW140-6	bdl	bdl	49.9	bdl	bdl	bdl	bdl	bdl	bdl	bdl	1.2	57.6	bdl	0.8	bdl	bdl	bdl	bdl	bdl	bdl	12.7	291.0	5.5

NW140-6	bdl	bdl	bdl	bdl	bdl	bdl	bdl	bdl	bdl	50.0	21.5	58.0	bdl	bdl	bdl	bdl	1.6	bdl	bdl	bdl	2.4	71.2	5.4
NW140-6	bdl	bdl	bdl	bdl	bdl	bdl	bdl	bdl	bdl	bdl	bdl	50.4	bdl	bdl	bdl	bdl	4.4	bdl	bdl	bdl	1.3	46.9	5.7
NW140-6	bdl	bdl	50.3	bdl	bdl	bdl	bdl	bdl	bdl	124.0	bdl	34.9	bdl	bdl	bdl	bdl	bdl	bdl	bdl	bdl	1.5	71.5	5.3
NW140-6	bdl	bdl	74.0	bdl	bdl	bdl	bdl	bdl	bdl	155.0	bdl	25.0	bdl	bdl	bdl	bdl	bdl	bdl	bdl	bdl	8.9	197.0	4.9
NW140-6	bdl	bdl	99.0	bdl	bdl	bdl	bdl	bdl	bdl	bdl	11.7	25.7	bdl	0.4	bdl	bdl	bdl	bdl	bdl	bdl	5.1	149.0	4.5
NW140-6	bdl	bdl	16.3	7.4	bdl	bdl	bdl	bdl	bdl	bdl	bdl	35.8	bdl	bdl	bdl	bdl	bdl	bdl	bdl	bdl	1.2	29.3	5.2
NW140-6	bdl	9.6	29.8	bdl	bdl	bdl	bdl	bdl	bdl	78.0	bdl	26.3	bdl	0.3	bdl	bdl	bdl	bdl	bdl	bdl	7.3	214.0	6.7
NW140-6	bdl	bdl	44.0	bdl	bdl	bdl	bdl	bdl	bdl	bdl	bdl	37.3	bdl	bdl	bdl	bdl	7.9	bdl	bdl	bdl	bdl	21.2	7.2
NW140-6	bdl	6.3	29.1	bdl	bdl	bdl	bdl	bdl	bdl	bdl	39.4	34.3	bdl	0.3	bdl	bdl	bdl	bdl	0.0	bdl	7.1	249.0	7.2
NW140-6	bdl	7.2	14.9	bdl	bdl	bdl	bdl	bdl	bdl	bdl	bdl	34.3	bdl	0.3	bdl	bdl	2.8	bdl	bdl	bdl	3.2	120.5	4.9
NW140-6	bdl	bdl	18.7	bdl	bdl	bdl	bdl	bdl	bdl	bdl	28.7	52.5	bdl	0.4	bdl	bdl	bdl	bdl	0.1	bdl	4.0	217.0	7.4
NW140-6	bdl	bdl	bdl	bdl	bdl	bdl	bdl	bdl	bdl	bdl	bdl	29.9	bdl	bdl	bdl	bdl	bdl	bdl	bdl	bdl	3.8	92.3	4.9
NW140-6	bdl	bdl	bdl	bdl	bdl	bdl	bdl	bdl	bdl	bdl	bdl	37.5	bdl	bdl	bdl	bdl	1.3	bdl	bdl	bdl	bdl	1.9	7.7
NW140-6	bdl	bdl	bdl	bdl	bdl	bdl	bdl	bdl	bdl	bdl	bdl	36.1	bdl	bdl	bdl	bdl	1.5	bdl	bdl	bdl	bdl	bdl	6.6
NW140-6	bdl	bdl	bdl	bdl	bdl	bdl	bdl	bdl	bdl	bdl	bdl	53.0	15.0	bdl	bdl	bdl	1.2	bdl	bdl	bdl	0.3	1.7	7.0
NW140-6	bdl	bdl	bdl	bdl	bdl	bdl	bdl	bdl	bdl	bdl	bdl	45.1	bdl	bdl	bdl	bdl	4.3	bdl	bdl	bdl	bdl	2.1	6.8
NW140-6	bdl	9.0	bdl	bdl	bdl	bdl	bdl	bdl	bdl	bdl	bdl	46.9	bdl	bdl	bdl	bdl	bdl	bdl	bdl	bdl	bdl	14.0	6.7
NW140-3	bdl	bdl	bdl	bdl	bdl	bdl	bdl	bdl	bdl	bdl	bdl	154.0	bdl	0.5	bdl	bdl	bdl	bdl	bdl	bdl	1.8	26.1	450.0
NW140-3	44.0	22.0	bdl	bdl	bdl	bdl	bdl	bdl	bdl	bdl	bdl	157.0	bdl	bdl	bdl	6.1	bdl	1.9	bdl	bdl	bdl	50.0	413.0
NW140-3	bdl	bdl	1130.0	bdl	bdl	bdl	bdl	bdl	bdl	bdl	bdl	115.0	bdl	0.9	bdl	bdl	bdl	bdl	bdl	bdl	13.3	117.0	377.0
NW140-3	bdl	bdl	623.0	bdl	bdl	bdl	bdl	bdl	bdl	bdl	1.1	82.0	bdl	1.3	bdl	bdl	bdl	bdl	bdl	bdl	13.4	189.0	398.0

NW140-3	61.0	23.0	930.0	28.0	bdl	bdl	bdl	bdl	bdl	bdl	bdl	65.0	bdl	1.6	bdl	bdl	bdl	bdl	bdl	bdl	3.9	89.0	370.0
NW140-3	bdl	bdl	579.0	bdl	32.0	bdl	bdl	bdl	bdl	bdl	bdl	73.0	bdl	0.8	bdl	bdl	bdl	bdl	bdl	bdl	9.8	136.0	308.0
NW140-3	26.0	bdl	528.0	bdl	bdl	bdl	bdl	bdl	bdl	bdl	79.0	62.0	6.0	0.7	bdl	bdl	bdl	bdl	bdl	bdl	11.9	91.0	243.0
NW140-3	bdl	bdl	680.0	bdl	bdl	bdl	bdl	bdl	bdl	bdl	bdl	63.0	bdl	0.6	bdl	bdl	2.3	bdl	bdl	bdl	3.5	96.0	255.0
NW140-3	bdl	bdl	337.0	bdl	bdl	bdl	bdl	bdl	bdl	bdl	bdl	101.0	bdl	1.6	bdl	bdl	bdl	bdl	bdl	bdl	13.4	199.0	339.0
NW140-3	33.0	bdl	504.0	bdl	70.0	bdl	bdl	bdl	22.0	120.0	bdl	91.0	bdl	1.3	bdl	bdl	bdl	bdl	bdl	bdl	11.1	126.0	273.0
NW140-3	bdl	bdl	246.0	14.0	bdl	bdl	bdl	bdl	bdl	50.0	7.4	81.0	bdl	1.3	bdl	bdl	bdl	bdl	bdl	bdl	9.6	97.0	270.0
NW140-3	bdl	bdl	503.0	19.0	bdl	bdl	bdl	bdl	bdl	bdl	bdl	93.0	14.0	0.9	bdl	bdl	bdl	bdl	bdl	bdl	11.1	111.0	309.0
NW140-3	bdl	20.0	178.0	bdl	bdl	bdl	bdl	bdl	bdl	450.0	bdl	155.0	bdl	0.9	bdl	bdl	bdl	bdl	bdl	bdl	11.3	124.0	412.0
NW140-3	bdl	30.0	810.0	bdl	bdl	bdl	bdl	bdl	bdl	150.0	bdl	119.0	bdl	0.7	bdl	bdl	bdl	bdl	bdl	bdl	8.0	151.0	501.0
NW140-3	bdl	50.0	980.0	36.0	bdl	bdl	bdl	bdl	140.0	bdl	bdl	112.0	bdl	bdl	bdl	bdl	bdl	bdl	bdl	bdl	7.1	93.0	530.0
NW140-3	50.0	bdl	239.0	50.0	bdl	bdl	bdl	bdl	bdl	bdl	bdl	109.0	bdl	0.6	bdl	bdl	12.0	bdl	bdl	bdl	7.6	120.0	336.0
NW140-3	67.0	bdl	bdl	bdl	bdl	bdl	bdl	bdl	bdl	bdl	bdl	150.0	bdl	bdl	bdl	bdl	bdl	bdl	0.4	bdl	bdl	40.0	508.0
NW140-3	bdl	15.0	bdl	bdl	bdl	bdl	bdl	18.0	bdl	bdl	33.0	142.0	bdl	0.8	bdl	bdl	bdl	bdl	bdl	bdl	5.0	35.8	464.0
MP-666	bdl	9.0	bdl	23.0	bdl	bdl	8.0	bdl	bdl	150.0	200.0	142.0	bdl	0.7	bdl	bdl	23.0	bdl	bdl	9.0	bdl	148.0	8.1
MP-666	bdl	bdl	bdl	71.0	158.0	bdl	bdl	bdl	bdl	bdl	388.0	332.0	55.0	bdl	bdl	bdl	bdl	bdl	bdl	bdl	3.4	225.0	8.8
MP-666	bdl	39.0	bdl	bdl	bdl	bdl	bdl	76.0	bdl	bdl	bdl	249.0	bdl	bdl	bdl	bdl	bdl	7.0	bdl	bdl	bdl	101.0	6.1
MP-666	110.0	76.0	bdl	bdl	bdl	bdl	bdl	bdl	bdl	1000.0	bdl	211.0	bdl	bdl	bdl	bdl	bdl	bdl	bdl	bdl	bdl	84.0	11.0
MP-666	bdl	bdl	bdl	bdl	bdl	bdl	bdl	bdl	bdl	bdl	bdl	75.0	bdl	bdl	bdl	bdl	bdl	bdl	bdl	bdl	bdl	5.0	5.0
MP-666	bdl	bdl	121.0	bdl	bdl	bdl	bdl	bdl	bdl	bdl	bdl	83.0	bdl	bdl	bdl	bdl	bdl	bdl	bdl	bdl	bdl	17.5	4.7
MP-666	bdl	bdl	bdl	bdl	bdl	bdl	bdl	bdl	bdl	bdl	bdl	155.0	bdl	bdl	bdl	bdl	bdl	bdl	bdl	bdl	bdl	169.0	5.6
MP-666	bdl	bdl	bdl	123.0	bdl	bdl	bdl	bdl	bdl	bdl	bdl	142.0	bdl	bdl	bdl	bdl	bdl	bdl	bdl	bdl	bdl	9.8	5.9
MP-666	bdl	79.0	bdl	bdl	bdl	bdl	bdl	bdl	bdl	bdl	bdl	96.0	bdl	bdl	bdl	bdl	bdl	bdl	bdl	bdl	0.8	9.1	5.8
MP-666	bdl	55.0	bdl	49.0	bdl	bdl	bdl	bdl	100.0	bdl	bdl	93.0	bdl	bdl	bdl	17.0	24.0	bdl	0.3	bdl	bdl	bdl	3.6
MP-666	bdl	bdl	bdl	bdl	bdl	bdl	17.0	bdl	bdl	bdl	bdl	bdl	bdl	0.6	bdl	bdl	bdl	bdl	bdl	bdl	bdl	bdl	2.8

MP-666	bdl	bdl	bdl	bdl	bdl	bdl	bdl	bdl	bdl	bdl	bdl	bdl	bdl	bdl	bdl	bdl	19.0	bdl	0.1	8.3	1.4	19.4	2.7
NW-121	bdl	11.1	bdl	13.2	38.0	bdl	bdl	bdl	bdl	bdl	bdl	170.0	bdl	bdl	bdl	bdl	bdl	bdl	bdl	bdl	bdl	1.8	30.6
NW-121	bdl	bdl	bdl	bdl	bdl	bdl	bdl	bdl	bdl	2800.0	bdl	92.0	bdl	bdl	bdl	bdl	bdl	bdl	bdl	bdl	bdl	3.8	26.1
NW-121	bdl	bdl	bdl	bdl	bdl	bdl	bdl	bdl	bdl	3200.0	bdl	172.0	bdl	bdl	bdl	bdl	bdl	bdl	bdl	bdl	bdl	25.9	33.1
NW-121	bdl	bdl	bdl	bdl	bdl	bdl	bdl	bdl	bdl	bdl	bdl	173.0	bdl	bdl	bdl	bdl	bdl	bdl	bdl	bdl	bdl	0.3	8.6
NW-121	bdl	bdl	bdl	bdl	bdl	bdl	bdl	bdl	bdl	360.0	bdl	285.0	bdl	bdl	bdl	bdl	bdl	bdl	bdl	bdl	bdl	0.4	11.7
NW-121	bdl	bdl	bdl	bdl	bdl	bdl	bdl	bdl	bdl	380.0	bdl	169.0	bdl	bdl	bdl	bdl	bdl	bdl	bdl	3.0	bdl	bdl	10.8
NW-121	bdl	bdl	bdl	bdl	bdl	bdl	bdl	bdl	bdl	bdl	bdl	182.0	bdl	bdl	bdl	bdl	bdl	bdl	bdl	bdl	bdl	12.7	20.7
NW-121	bdl	bdl	bdl	bdl	bdl	bdl	bdl	bdl	bdl	bdl	bdl	150.0	bdl	bdl	bdl	bdl	bdl	bdl	bdl	bdl	bdl	13.8	18.4
NW-121	12.6	bdl	bdl	bdl	bdl	bdl	bdl	bdl	bdl	90.0	bdl	190.0	13.9	bdl	bdl	bdl	bdl	bdl	bdl	bdl	bdl	bdl	17.6
NW-121	bdl	bdl	bdl	bdl	bdl	bdl	bdl	bdl	bdl	bdl	2.8	226.0	6.7	bdl	bdl	bdl	bdl	bdl	bdl	bdl	0.1	0.7	22.0
NW-121	bdl	bdl	bdl	bdl	bdl	bdl	bdl	bdl	bdl	bdl	bdl	310.0	5.3	bdl	bdl	bdl	2.6	bdl	bdl	bdl	bdl	1.5	22.7
MP-688	bdl	bdl	bdl	bdl	190.0	bdl	bdl	bdl	bdl	bdl	bdl	144.0	bdl	bdl	bdl	bdl	2100.0	bdl	bdl	bdl	bdl	bdl	bdl
MP-688	bdl	bdl	bdl	bdl	bdl	bdl	bdl	bdl	bdl	bdl	bdl	74.0	41.0	bdl	bdl	bdl	1010.0	bdl	bdl	bdl	bdl	bdl	bdl
MP-688	bdl	bdl	bdl	bdl	170.0	bdl	bdl	bdl	bdl	bdl	bdl	163.0	bdl	bdl	bdl	bdl	960.0	bdl	bdl	bdl	bdl	15.5	2.0
MP-688	bdl	25.0	bdl	bdl	bdl	bdl	bdl	bdl	92.0	110.0	bdl	132.0	bdl	bdl	bdl	bdl	bdl	bdl	bdl	bdl	bdl	1.9	bdl
MP-688	bdl	bdl	bdl	bdl	bdl	bdl	bdl	bdl	bdl	80.0	bdl	99.0	bdl	bdl	bdl	9.4	bdl	bdl	0.9	bdl	bdl	19.1	bdl
MP-688	24.0	bdl	bdl	bdl	bdl	bdl	bdl	bdl	bdl	100.0	14.8	100.0	bdl	bdl	bdl	bdl	21.0	bdl	bdl	5.7	bdl	3.8	bdl
MP-688	52.0	bdl	bdl	bdl	bdl	bdl	bdl	bdl	bdl	360.0	19.0	93.0	bdl	bdl	bdl	bdl	106.0	bdl	bdl	bdl	bdl	3.8	bdl
MP-699	bdl	bdl	1040.0	46.0	35.0	bdl	bdl	bdl	bdl	bdl	bdl	379.0	bdl	0.6	bdl	bdl	bdl	bdl	bdl	bdl	bdl	209.0	147.0
MP-699	bdl	10.0	711.0	48.0	bdl	bdl	bdl	bdl	bdl	bdl	bdl	341.0	bdl	bdl	bdl	bdl	bdl	bdl	bdl	bdl	5.0	284.0	169.0
MP-699	15.0	bdl	1220.0	bdl	bdl	bdl	bdl	bdl	71.0	bdl	bdl	249.0	bdl	bdl	bdl	bdl	bdl	bdl	bdl	bdl	3.0	207.0	113.0
MP-699	bdl	bdl	921.0	bdl	bdl	bdl	bdl	bdl	bdl	76.0	bdl	301.0	bdl	bdl	bdl	bdl	bdl	bdl	bdl	bdl	2.0	175.0	119.0
MP-699	bdl	8.0	1065.0	bdl	26.0	bdl	bdl	bdl	bdl	bdl	bdl	219.0	1.5	bdl	bdl	bdl	bdl	bdl	bdl	bdl	2.5	137.0	114.0
MP-699	bdl	8.5	1610.0	bdl	14.0	bdl	bdl	bdl	bdl	bdl	bdl	201.0	bdl	bdl	bdl	bdl	bdl	bdl	bdl	bdl	1.7	137.0	113.0
MP-699	bdl	bdl	681.0	bdl	bdl	bdl	bdl	bdl	25.0	bdl	bdl	209.0	bdl	bdl	bdl	bdl	2.7	bdl	bdl	bdl	bdl	93.0	105.0
MP-699	bdl	bdl	734.0	bdl	bdl	bdl	bdl	bdl	45.0	bdl	bdl	165.0	bdl	bdl	bdl	bdl	5.2	bdl	bdl	1.7	1.7	99.0	114.0
MP-699	bdl	bdl	1212.0	bdl	39.0	bdl	bdl	bdl	bdl	bdl	bdl	247.0	bdl	0.4	bdl	bdl	6.0	bdl	bdl	bdl	1.8	162.0	113.0
MP-699	28.0	17.0	1310.0	18.0	bdl	bdl	bdl	bdl	bdl	bdl	bdl	183.0	bdl	bdl	bdl	bdl	bdl	bdl	bdl	bdl	bdl	142.0	116.0

	Estadística																						
	V	**Cr**	**Mn**	**Co**	**Ni**	**Zn**	**Ga**	**Ge**	**As**	**Se**	**Mo**	**Ag**	**Cd**	**In**	**Sn**	**Sb**	**Te**	**Pt**	**Au**	**Hg**	**Tl**	**Pb**	**Bi**
Mínimo	12.6	6.3	14.9	6.8	14.0	48.0	8.0	18.0	22.0	50.0	1.1	25.0	1.5	0.2	10.0	6.1	1.2	1.9	0.0	1.7	0.1	0.3	2.0
Máximo	110.0	101.0	1610.0	123.0	190.0	48.0	43.0	76.0	140.0	90000.0	388.0	460.0	55.0	1.6	10.0	17.0	2100.0	7.0	0.9	9.0	13.4	322.0	530.0
Mediana	33.5	21.5	420.0	32.0	54.0	48.0	17.0	47.0	71.0	150.0	14.8	119.0	12.0	0.7	10.0	9.4	6.0	4.5	0.1	5.7	3.9	79.5	16.5
Promedio	40.1	30.1	498.1	40.4	81.8	48.0	22.7	47.0	68.0	4480.5	51.0	144.3	15.8	0.7	10.0	10.8	188.0	4.5	0.2	5.5	5.5	89.4	97.6
Sobre l.d.	18	30	40	16	12	1	3	2	9	24	17	93	11	27	1	3	23	2	9	5	45	84	89